UNIVERSITY OF CALGARY

Seismic attenuation measurements from multicomponent vertical seismic profile data

by

Michelle Carolina Montano Spagnolo

A THESIS
SUBMITTED TO THE FACULTY OF GRADUATE STUDIES
IN PARTIAL FULFILLMENT OF THE REQUIREMENTS FOR THE
DEGREE OF MASTER OF SCIENCE

GRADUATE PROGRAM IN GEOLOGY AND GEOPHYSICS

CALGARY, ALBERTA
FEBRUARY, 2017

Abstract

Vertical seismic profile (VSP) data provide a means to estimate the seismic wavelet at different receiver depths. The downgoing wavefield has always been the key to measure attenuation (Q) and enables us to correct for the effects of seismic attenuation on seismic data. We demonstrate that we can also use the upgoing wavefield to estimate Q, using reflections and mode-converted waves. In this work, Q is estimated from synthetic VSP downgoing and upgoing wavefields by using the spectral matching method. We also estimated Q, using the spectral matching method, from VSP data collected in a 500 m deep well in a heavy oil field and a 2000 m deep well in a shale gas play in Western Canada. For the first case, we obtained values of Q_P of approximately 50 and Q_S of 20 for the strata intersected by the well. For the second case, we obtained values of Q_P of approximately 50 and Q_S of 30. In the case of Q_S estimations, our results indicate that using the upgoing converted wavefield provides good estimations when downgoing S-wave are not available in the data.

Acknowledgements

I would like to thank my supervisor Dr. Don Lawton for his guidance and constant support, not only in my research but also in the extracurricular activities that I participated in the University of Calgary. Dr. Lawton encouraged me to work hard and find solutions to the problems I encounter. His broad knowledge inspires me every day to continue learning. I am very grateful to have him as my supervisor. I also would like to thank my co-supervisor Dr. Gary Margrave for his help, support and patience. Dr. Margrave was very welcoming and willing to answering all my questions. His course lecture notes of Seismic Signal Processing were very helpful for me and many other students. Also, I would like to extend my gratitude to Dr. Daniel Trad and Dr. Larry Bentley who kindly accepted to be part of my examiner committee on a short notice.

Special thanks to the sponsors of Consortium for Research in Elastic Wave Exploration Seismology (CREWES) for continued support. This work was funded by CREWES industrial sponsors and the Natural Science and Engineering Research Council of Canada (NSERC) through the grant CRDPJ 461179-13. I am grateful to the Canadian Society of Exploration Geophysicists (CSEG) for awarding me the 2014/2015 CSEG scholarship sponsored by Canadian Natural Resources (CNRL). Also, I was supported by 2016 Grant Spratt Graduate Scholarship in Geology. Special thanks to two anonymous companies for access to the field VSP data, GEDCO/Schlumberger for providing the VISTA software and NORSAR for the NORSAR-2D software.

Thanks to Adriana Gordon, Gabriela Gonzalez, Tianci Cui, Rafael Azuaje, and Faranak Mahmoudian for their friendship and support. My office mates, Bona Wu and Jessica Dongas for those great talks. Laura Baird for her help and support. My dear friend Babatunde who I miss every day, thanks for your help and kindness. CREWES fellow students and staff who helped me during this MSc program. I am thankful to Dr. Kris Innanen and Dr. Larry Lines for their guidance and kindly answering all my questions. Special thanks to Roy Lindseth for editing this thesis whose corrections are fantastic and for being such a great person.

I would like to thanks my parents, Diana Spagnolo and Miguel Montano for their support, patience and unconditional love.

Finally, I would like to thanks, Raul Cova who is my friend and family for his help, patience, friendship, guidance, and support. I would not get that far without his help. He inspires me to work hard, help other people, and enjoy life. It is an honour for me to be his wife.

Dedication

A mis padres y esposo. Sin ellos no estaria aqui.

Contents

List of Tables

List of Figures

List of Symbols, Abbreviations and Nomenclature

Symbol	Definition
VSP	Vertical Seismic Profile
2D	Two-dimensional
3D	Three-dimensional
ρ	Density
Hz	Hertz
m	Meters
Q	Quality factor
Q_P	P-wave attenuation
Q_S	S-wave attenuation
Q_I	Intrinsic attenuation
Q_A	Apparent attenuation
QVO	Q versus offset
V_P	P-wave velocity
V_S	S-wave velocity
P-wave	Compressional wave
S-wave	Shear wave
CMP	Common mid-point
CCP	Common conversion point
NMO	Normal moveout
SV	Vertically polarized shear energy
SH	Horizontally polarized shear energy
Z	Vertically oriented geophone
H1	Horizontally oriented geophone
H2	Horizontally oriented geophone
Hmax	Polarized H1 and H2 data oriented tangent to plane defined by source and well bore
Hmin	Polarized H1 and H2 data oriented perpendicular

	to plane defined by source and well bore
Hmax’	Polarized Z and Hmax data oriented in a direction towards source
Z’	Polarized Z an Hmax oriented perpendicular to the Hmax’ data
Hmax”	Polarized Z and Hmax data oriented along upgoing wave arrivals
Z”	Polarized Z and Hmax data oriented perpendicular to Hmax”
S/N	Signal/Noise

Chapter 1

INTRODUCTION

1.1 Introduction

A general definition of seismic attenuation is the decay in amplitude during wave propagation that cannot be explained by geometric spreading over the distance travelled. The quality factor Q, is a parameter inversely proportional to seismic attenuation. Liner (2012) summarized the common attenuation processes as in Figure 1.1. Typically, these are separated into two kinds of attenuation, intrinsic attenuation, and apparent-attenuation (Spencer et al., 1982; Richards and Menke, 1983; Liner, 2012), which are described below:

Intrinsic attenuation: is the conversion of wave energy into heat. This can be measured on a material sample in the laboratory and represents a rock property. This type of attenuation is approximately constant and usually small in the frequency band of surface seismic (Liner, 2012).

Apparent attenuation: is due to the presence of a layered media in which various processes occur such as reflection, transmission, multiples, and mode conversion. These processes conserve the energy. Another kind of apparent attenuation is due to random scattering which occurs mainly in the near-surface rocks (Liner, 2012).

The downgoing wavefield recorded in a zero-offset vertical seismic profile (VSP) data set provides a means to estimate seismic attenuation (Q) through a rock sequence (Figure 1.2a). This gives us access to the wavelet at different receiver depths, which makes Q estimation a relatively straight-forward process. However, we may encounter the following problems in determining Q, when using the downgoing wavefield from a zero-offset VSP. Firstly, some receivers may be very close to the source. Shallow data recorded by these receivers may be clipped or swamped with noise. Also, the wavefield has travelled for only a short period of time and significant attenuation may not be observed when the data is processed (Montano et al., 2015). Therefore, estimates of Q in very near-surface strata can be problematic.

Secondly, downgoing shear waves are not always easy to identify in a zero-offset VSP with a vibrator or dynamite energy source. The direct shear wave must travel through the near-surface, losing significant energy and bandwidth. If we desire to obtain reliable Q_S estimation through the rock strata over the full depth of the well, this energy loss is a problem.

One way to solve these issues is to use the upgoing wavefield from a zero-offset VSP (Figure 1.2b). For this case, a virtual source (green dot) is assumed far from the receivers in the near-surface (Figure 1.2c). This enables more reliable Q estimations in the near-surface. For Q_S measurements, we propose an alternative method to estimate Q_S by exploiting converted-wave (P-S) reflections from a walkaway VSP (Figure 1.3a). In this case, the downward propagating seismic wavefield travels as a P-wave and reflects as an S-wave. As a result, the S-wave generated at the conversion point has the same bandwidth as the P-wave incident upon the reflector (Figure 1.3b, green dots). This enables reliable Q_S estimations over the full depth range of the VSP data.

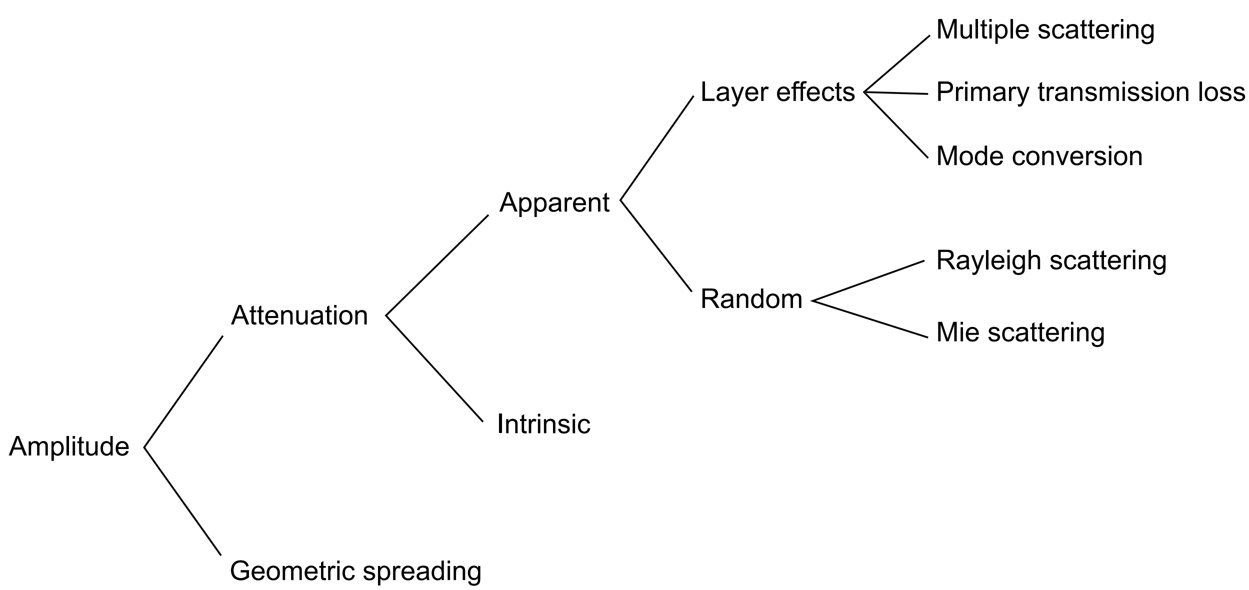

Figure 1.1: Amplitude phenomena related to subsurface properties. From Liner (2012).

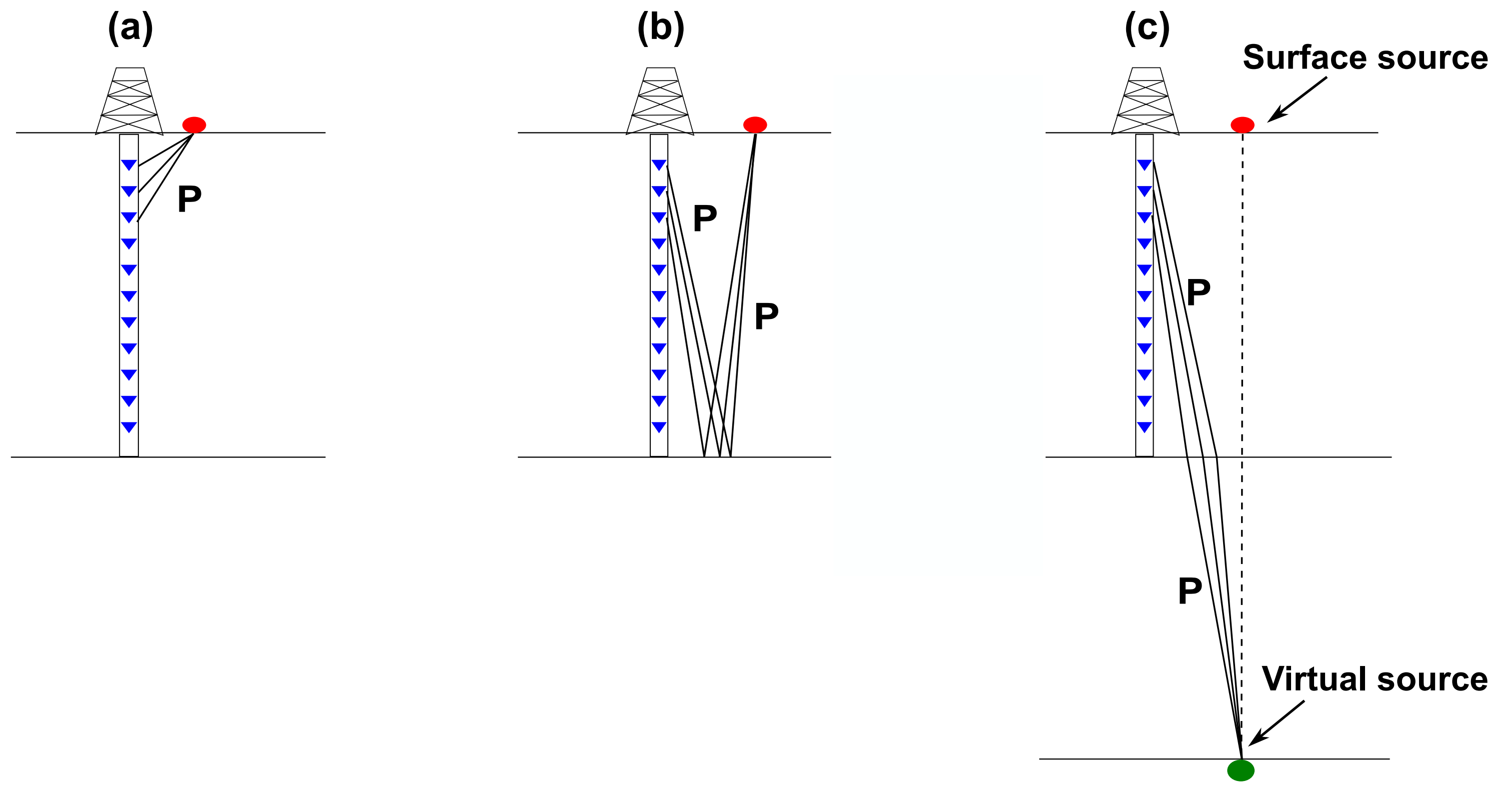

Figure 1.2: Vertical seismic profile P-waves, (a) Downgoing wavefield, (b) Upgoing wavefield and (c) Upgoing wavefield from a virtual source in depth (green dot).

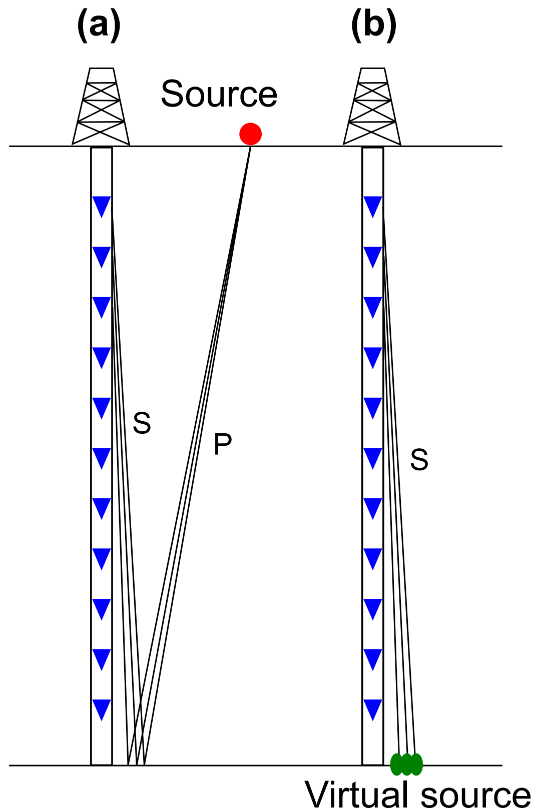

Figure 1.3: Mode-converted waves having (a) a surface source and (b) a virtual source in depth.

1.2 Thesis objectives

The main goal of this thesis is to use data from a multicomponent VSP in a heavy oil reservoir to measure seismic attenuation and to identify fluid saturation within the strata intersected by the well. This was achieved by defining specific tasks which are the following:

- Processing the multicomponent VSP data set without altering the amplitudes; picking travel times of first breaks and upgoing events; rotating the components and separating the wavefields.

- Measuring P-wave attenuation from downgoing and upgoing wavefields in the zero-offset VSP data.

- Measuring S-wave attenuation from the downgoing wavefield in zero-offset VSP data, and from converted-waves recorded in walkaway VSP data.
- Comparing seismic attenuation versus velocity along the strata intersected in the well to identify fluid saturation.

1.3 Data

Case Study 1

A walkaway VSP located in Western Canada was used for this part of the thesis. Fourteen source points were acquired; first, using 0.125 kg of dynamite at 9 m depth for energy source, and then with an EnviroVibe source using a linear sweep of 10-300 Hz over 20 s (Figure 1.4). The acquisition parameters are shown in Table 1.1.

Table 1.1: Acquisition parameters for case study 1.

	Parameters
Number of shots	14
Number of receivers	222
Type of receivers	VectorSeis
Receivers depth	63.72 - 506.63 m
Receiver spacing	$\sim$ 2 m
Record length	3 s
Sampling	0.001 s
Date	December 2011

Case Study 2

We also studied a 3D VSP located in Western Canada. For this case, 1047 source points were acquired with a Mertz 18 vibrator using a linear sweep of 6-120 Hz over 12 s (Figure 1.5). The acquisition parameters for this study, are shown in Table 1.2.

Table 1.2: Acquisition parameters for case study 2.

	Parameters
Number of shots	1047
Number of receivers	135
Type of receivers	GeoRes 57
Receivers depth	11.1 - 2026.46 m
Receiver spacing	$\sim$ 15 m
Record length	6 s
Sampling	0.002 s
Date	February 2012

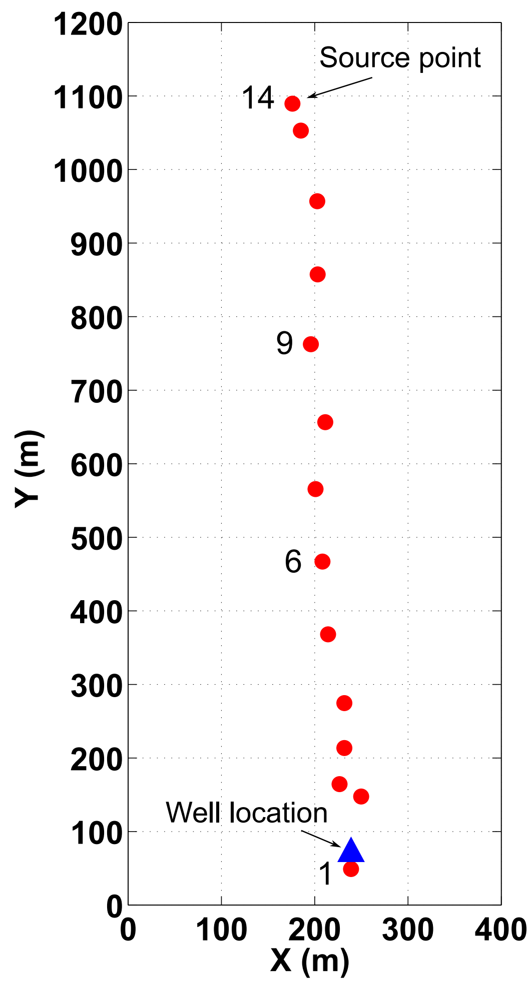

Figure 1.4: Case study 1: borehole location (blue triangle) and source points (red dots).

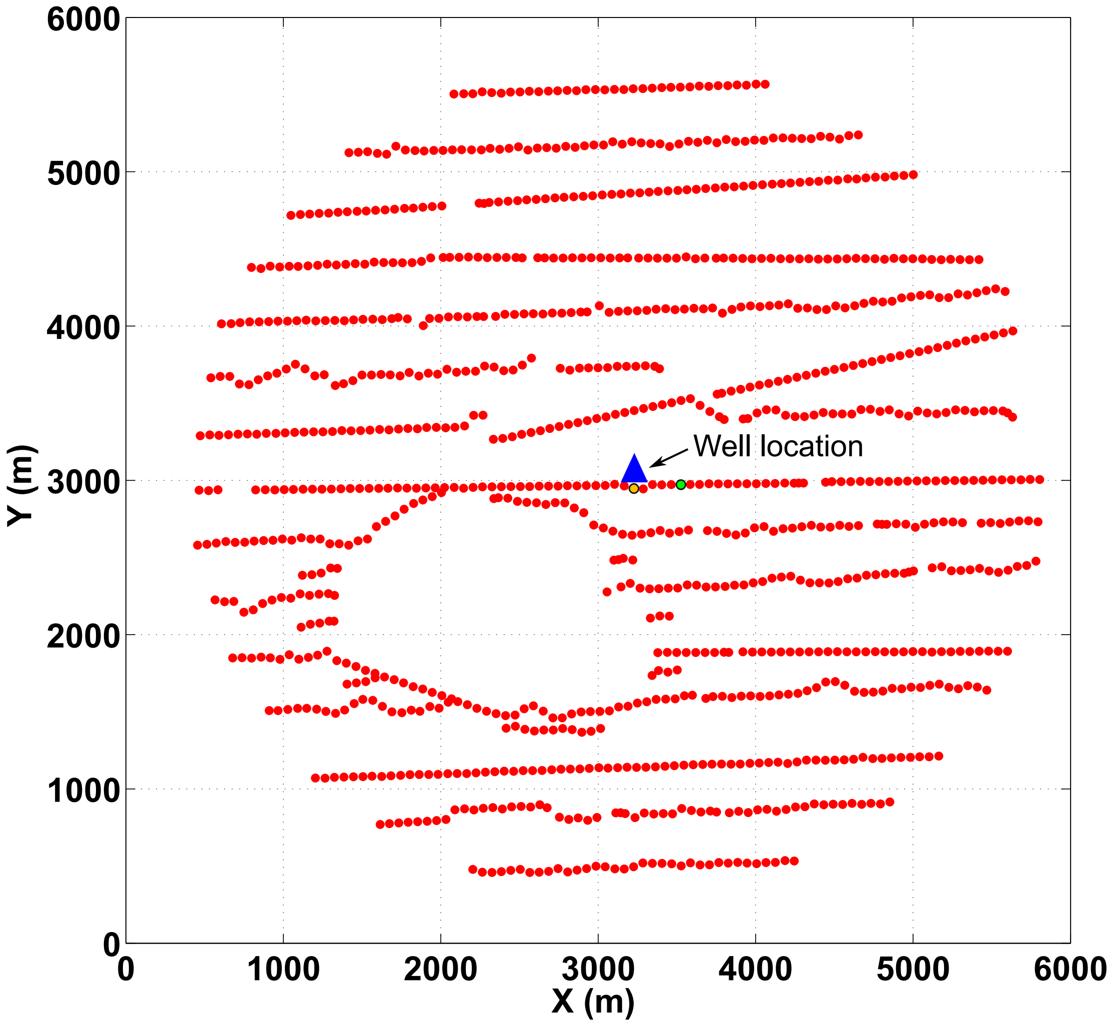

Figure 1.5: Case study 2: borehole location (blue triangle) and source points (red dots). Yellow dot indicates source point 1 at 72 m from the well. Green dot indicates source point at 300m from the well used for future work.

1.4 Software

MATLAB® was used to compute synthetic zero-offset VSP data. NORSAR2D® was used to compute synthetic walkaway VSP data. For the case study 1 and 2, we processed the field VSP data set using VISTA and MATLAB software. LaTeX was used for the thesis assembly and INKSCAPE to edit figures.

Following is a detailed list of software used in this thesis:

- VISTA2D/3D®; Schlumberger seismic processing software.
- MATLAB® 2013; student version. High-level language for scientific and engineering computing.
- NORSAR2D®; a ray modelling package to create synthetic seismic data using ray-tracing algorithms.
- LaTeX; an open source text editor.
- INKSCAPE; an open source figure editor.

1.5 Original Contributions

The main contribution of this thesis is an alternative method to estimate seismic attenuation (Q) from reflections and mode-converted waves recorded in VSP surveys. As we mentioned previously, the direct downgoing wavefield recorded in VSP surveys provides a means to estimate Q through strata intersected by the borehole. However, we encountered problems estimating Q through the near-surface strata when using the downgoing wavefield. For this reason, we explored an alternative method using reflected and mode-converted waves. Here is a list of the specific contributions:

- Rotation to isolate mode-converted upgoing S-waves events using a time-invariant polarization.
- An alternative method to estimate Q_P in the near-surface using the upgoing wavefield or reflections (P-P) recorded in a zero-offset VSP survey.

- An alternative method to estimate Q_S from mode-converted waves (P-S) recorded in an offset VSP survey.

- An existing function named ***VSP_separation*** to separate the wavefield in a VSP, was upgraded and split into ***VSP_separation_down*** to extract the downgoing wavefield, and ***VSP_separation_up*** to extract the reflected and mode-converted upgoing wavefield.

Chapter 2

THEORETICAL BACKGROUND

2.1 Vertical seismic profile

For a vertical seismic profile (VSP) survey the geophones are placed at various depths in a well to measure a seismic signal generated at the surface of the earth (Hardage, 1985). The location of the geophones enabled us to record both downgoing and upgoing seismic events (Figure 2.1a and 2.1b respectively). Whereas, in surface seismic acquisition, only upgoing events or reflections are recorded. Also, each receiver records P-waves or S-waves (Figure 2.1c). P-waves vibrate in the direction of propagation whereas S-wave vibrate perpendicular to the direction of propagation, either in the plane of source and receiver (SV-waves) or out of the plane (SH-waves) (Hinds et al., 1996).

2.1.1 Types of VSP surveys

VSP surveys are classified by the geometry which depends on source offset, borehole trajectory, and receiver array (Figure 2.2).

Checkshot and zero-offset VSPs, the most common type, are surveys that have the energy source placed close to the wellhead (Martinez and Jones, 2010).

Offset, walkaway and walkaround VSPs surveys all have the source offset from the well (Martinez and Jones, 2010).

3D VSP's are acquired to illuminate 3D structures; the survey geometry can follow either parallel lines or concentric circles around the borehole (Martinez and Jones, 2010).

Crosswell VSP is less common and consists of two boreholes; one to deploy the seismic source and the other, the receiver array (Martinez and Jones, 2010).

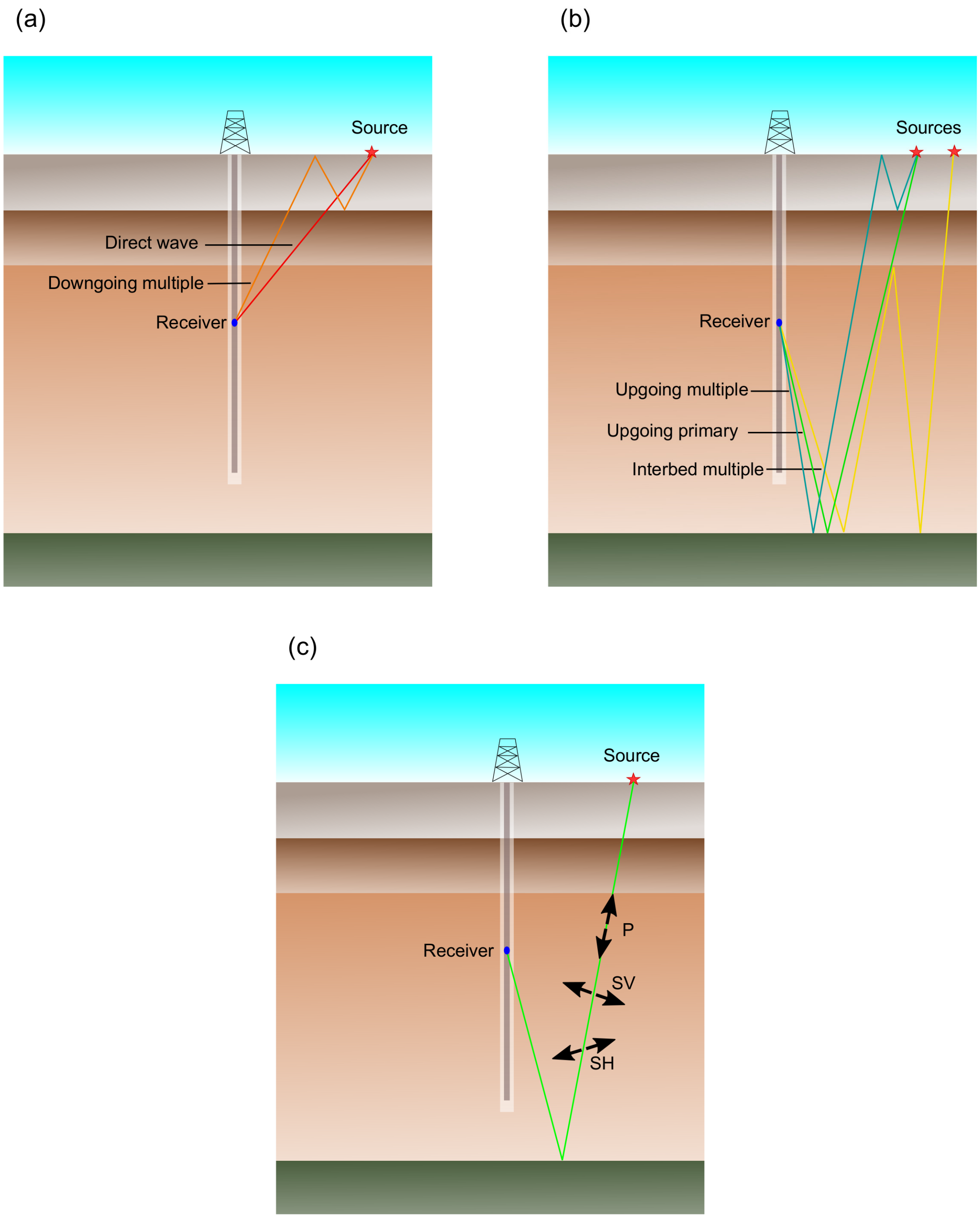

Figure 2.1: Vertical Seismic Profile. (a) Downgoing wavefields, (b) Upgoing wavefields, and, (c) Modes. Adapted from Hinds et al. (1996) and Martinez and Jones (2010).

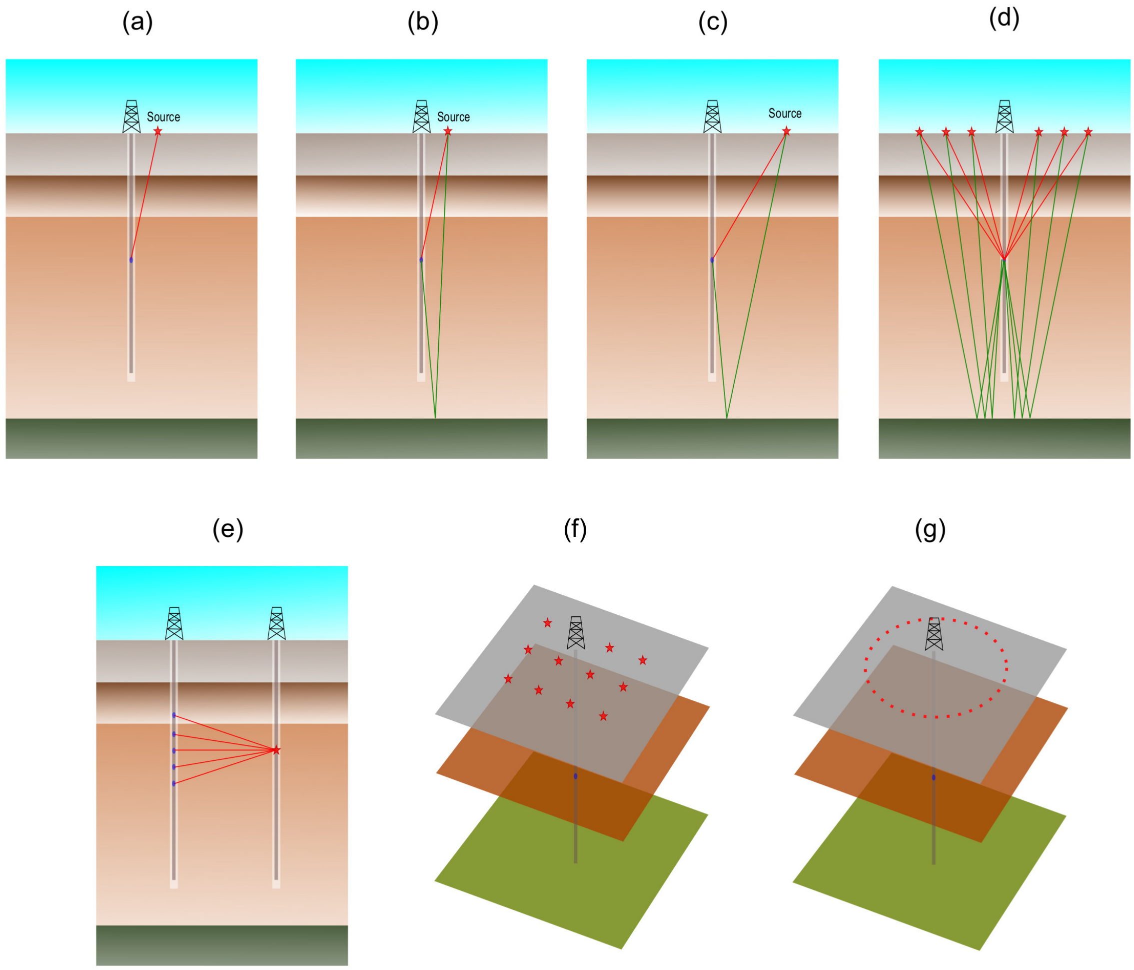

Figure 2.2: VSP survey types. (a) Checkshot, (b) Zero-offset, (c) Offset, (d) Walkaway, (e) Crosswell, (f) 3D, and, (g) Walkaround. Adapted from Martinez and Jones (2010).

2.1.2 VSP data processing

The direct downgoing wavefield of first arrivals, usually have higher amplitudes than upgoing events, which may make it difficult to interpret upgoing primary reflections. A typical processing flow, oriented to enhance the upgoing events, involves stacking, deconvolution, and bandpass filtering, among other routines (Wu, 2016). In this study, we try to avoid such processes in order to preserve the amplitude of the wavelet and obtain reliable Q estimates. However, we still need to do preliminary processing, which includes some of the following steps:

Rotation

In a VSP survey the total wavefield is recorded on three components, namely, the vertical component z, and horizontal components H1 and H2 (Figure 2.3a). The first rotation, we have to orient the horizontal components to a fixed reference because these are randomly rotated from depth to depth. Direct arrivals assumed to be P-waves are used as the reference frame into which to rotate the horizontal components because the projection into the same receiver plane does not variate with depth (DiSiena et al., 1984). The polarization angle θ can be calculated using hodograms, a graphical representation of particle displacement (Figure 2.4). This typically shows an elongated ellipse pointing in the direction of the source-receiver azimuth of direct arrivals. The data are usually oriented on a particular axis, for example Hmax, the vertical plane between the source and receiver, to maximize the energy for a given time window around the first breaks (Appendix A).

For the second rotation, the horizontal component Hmax obtained previously, and the vertical component z, are rotated in the plane of the well and source (Figure 2.3b) to obtain z' and Hmax' using hodogram analysis (Figure 2.5). Hmax' data shows mainly downgoing P-wave and mode-converted upgoing S-wave energy. The z' data contains predominately downgoing S-wave and upgoing P-wave energy, and also some remnants of the converted S-wave (Hinds et al., 1996). Figures 2.6 and 2.7 respectively show the recorded wavefield before and after rotations.

(a)

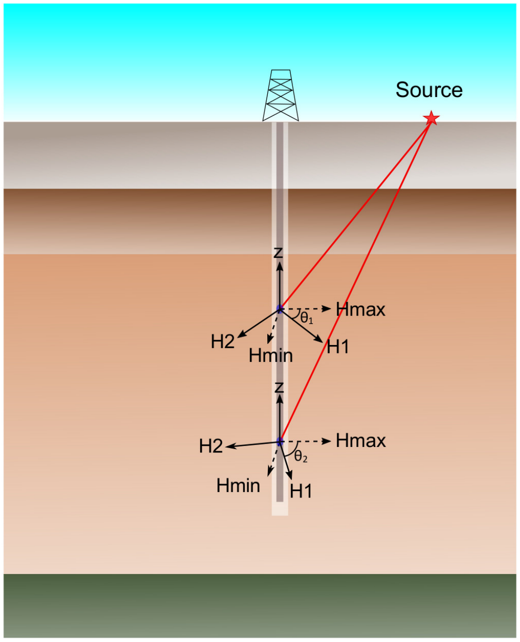

(b)

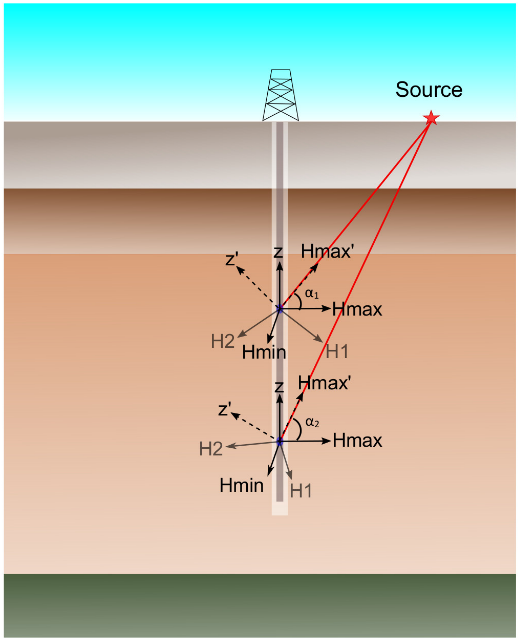

Figure 2.3: Geophone orientation at different depths; (a) First rotation using the horizontal components H1 and H2. (b) Second rotation using the vertical component z and the horizontal component Hmax. Adapted from Hinds et al. (1996).

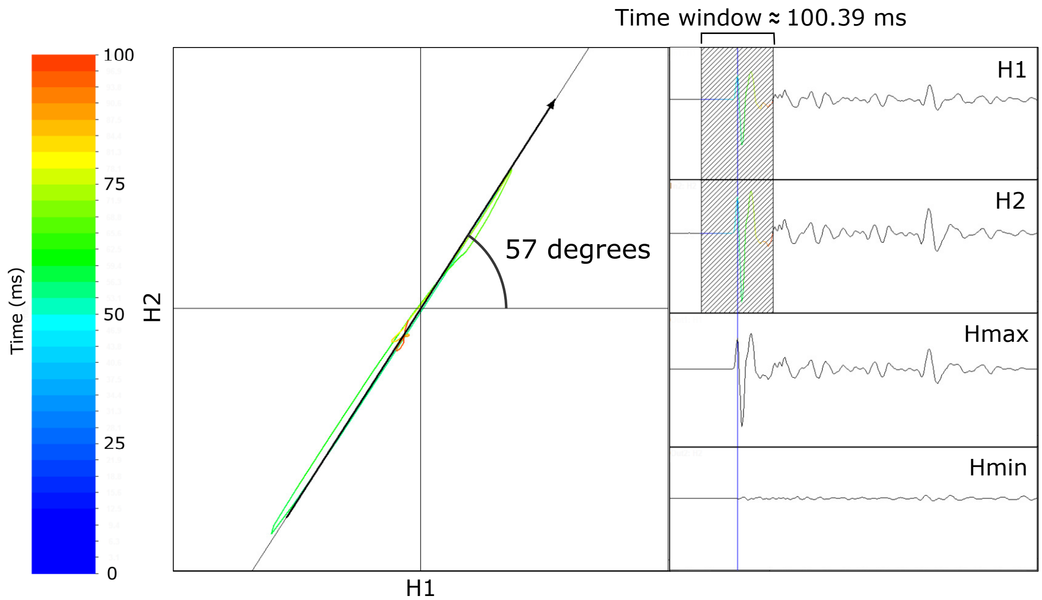

Figure 2.4: Example of hodogram analysis using horizontal components H1 and H2. Source point 10. Source offset ≈ 703.26 m. Receiver depth ≈ 322.25 m. Time window between 318.00 ms and 418.39 ms.

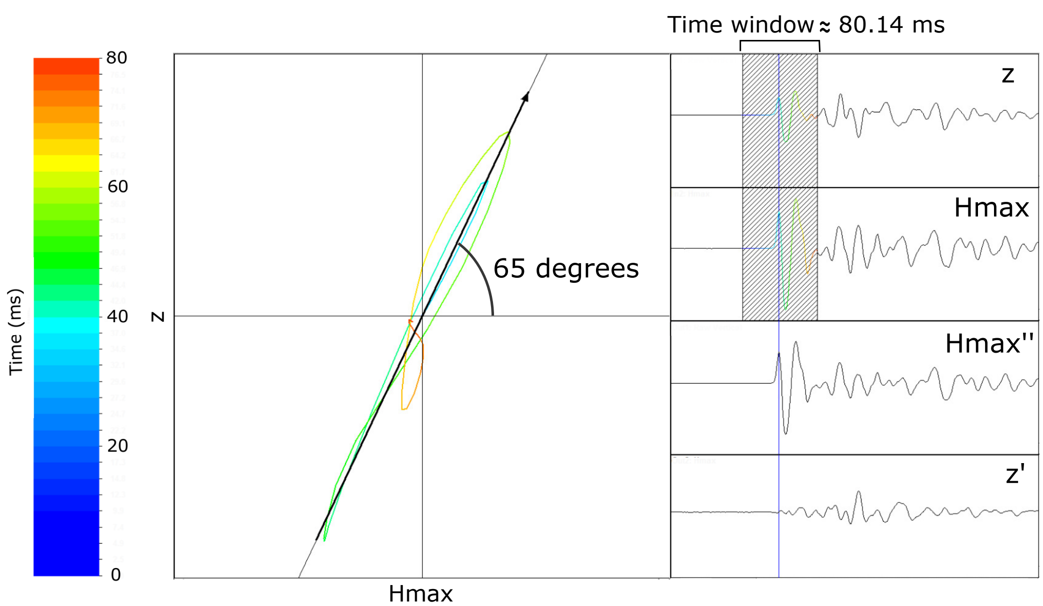

Figure 2.5: Example of hodogram analysis using vertical component z and horizontal component Hmax. Source point 10. Source offset ≈ 703.26 m. Receiver depth ≈ 414.44 m. Time window between 330.36 ms and 410.50 ms.

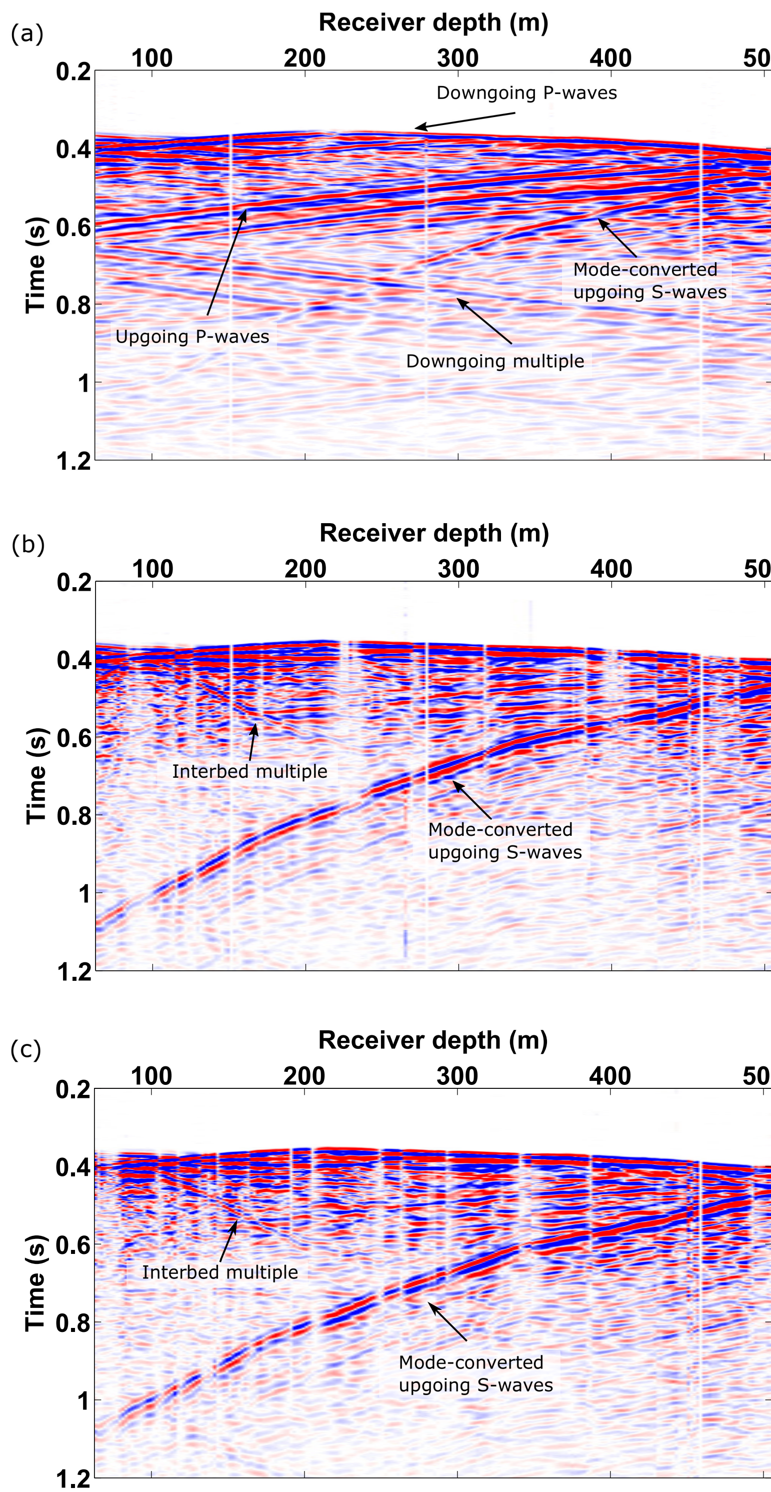

Figure 2.6: Source gather 10. (a) Vertical component z, and horizontal components, (b) H1, and (c) H2. These are true relative amplitude.

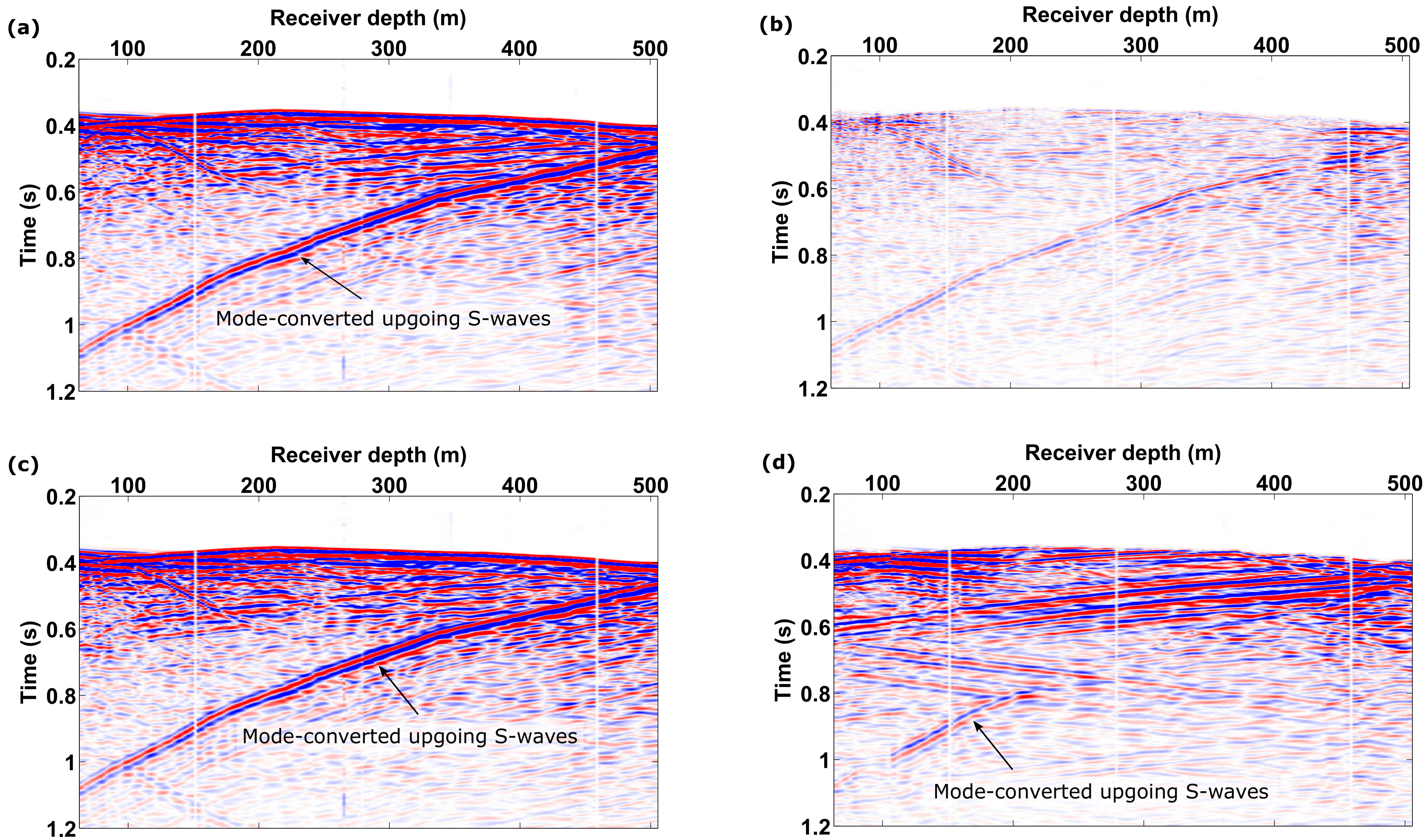

Figure 2.7: Source gather 10. Rotation to isolate downgoing event. (a) Hmax, (b) Hmin, (c) Hmax', and, (d) z'. These are true relative amplitude.

Rotation to isolate mode-converted upgoing S events.

The mode-converted upgoing S-wave is recorded with the three components: vertical component z and horizontal components H1 and H2 (Figure 2.6). In the first rotation, most of the converted wave energy is transferred to Hmax (Figures 2.6a and 2.6b). After the second rotation, some energy still remains in the vertical component z' (Figures 2.6c and 2.6d) because the polarization is based on the first arrival. For this case, we propose the second rotation to be based on the upgoing event. Then, Hmax is rotated toward the reflector or incidence point to obtain Hmax" and z" (Figure 2.8). In the hodogram analysis, we wish to rotate the time window centered on the upgoing event that which is the event coming from the deepest reflector just below the borehole (Figure 2.9). Now, the mode-converted upgoing S-wave recorded in the vertical component z has been transferred to z" (Figure 2.10). In this case, z" and Hmax" have a different meaning to the same terms referred in Hinds et al. (1996).

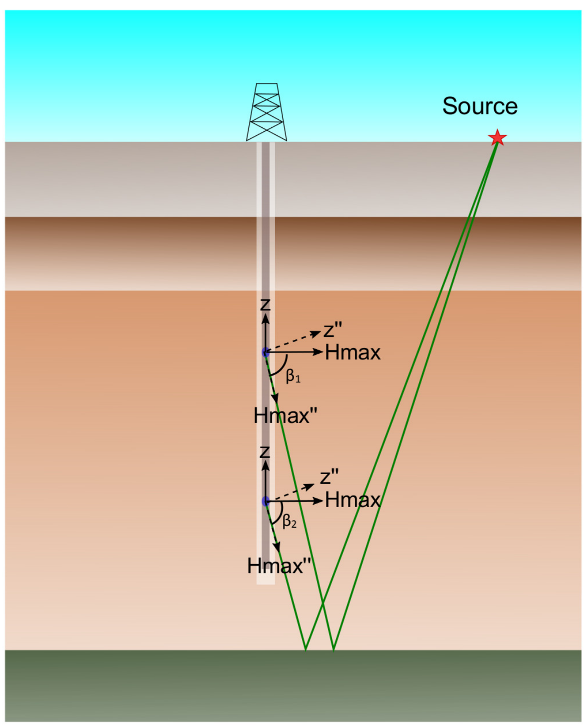

Figure 2.8: Geophone orientation at different depths. Upgoing wavefield.

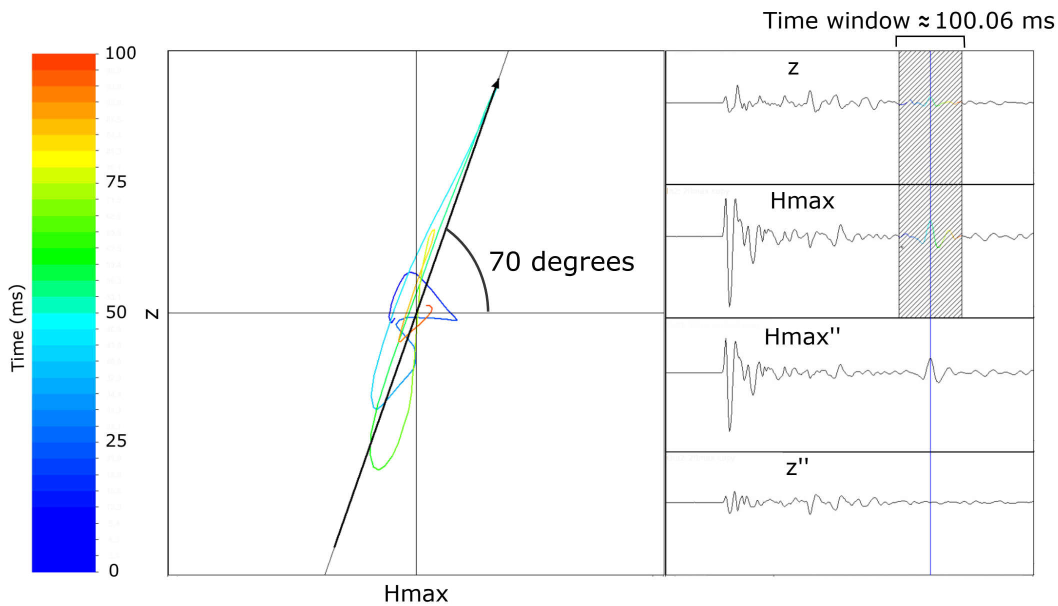

Figure 2.9: Example of hodogram analysis using vertical component z and horizontal component Hmax. Source point 10. Source offset ≈ 703.26 m. Receiver depth ≈ 282.17 m. Time window between 638.60 ms and 738.66 ms.

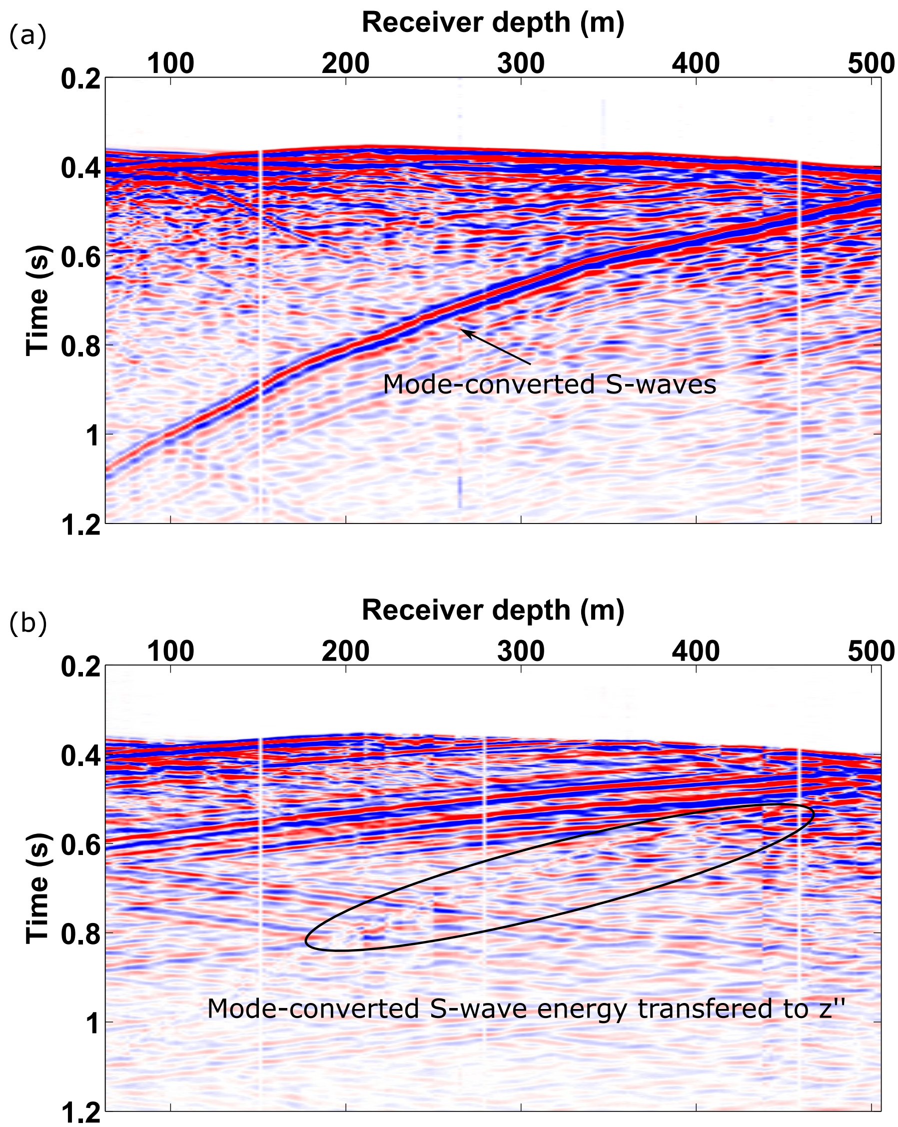

Figure 2.10: Source gather 10; Rotation to isolate mode-converted upgoing S-wave. (a) z”, and (b) Hmax”.

Static Time shift

VSP events can be positioned at the same time recorded by surface geophones by applying a static time shift (Hardage, 1985). First, we have to define the first breaks t_{fb}. For the upgoing events we delay each trace by the same amount of the first break time (add + t_{fb}). For all downgoing events we must advance each trace by an amount equal to the first break time (add - t_{fb}). Figure 2.11 shows the total wavefield before and after applying static shift times to their mean time, (add - $t_{fb} + mean(t_{fb})$), in order to flatten the downgoing events.

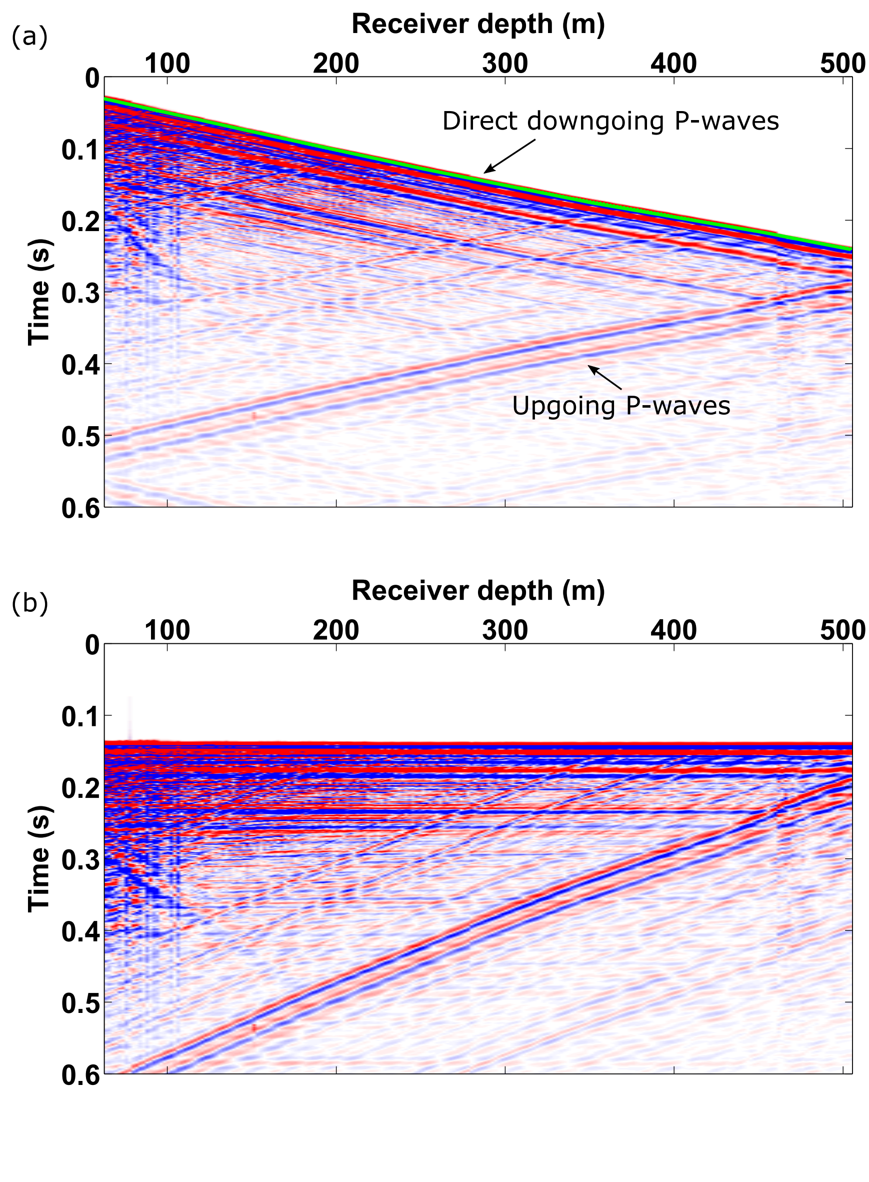

Figure 2.11: Source gather 1; (a) Total wavefield before and (b) after static shifts. Green line indicates first breaks.

Wavefield separation

A median filter is used to separate the wavefield (Hinds et al., 1996). First, a static shift is applied to each trace in order to flatten the first break events to their mean time (Figure 2.11b). Then, a spatial median filter is computed over a time window to isolate the downgoing events. The extracted downgoing wavefield is subtracted from the total wavefield to obtain the upgoing wavefield (Figure 2.12).

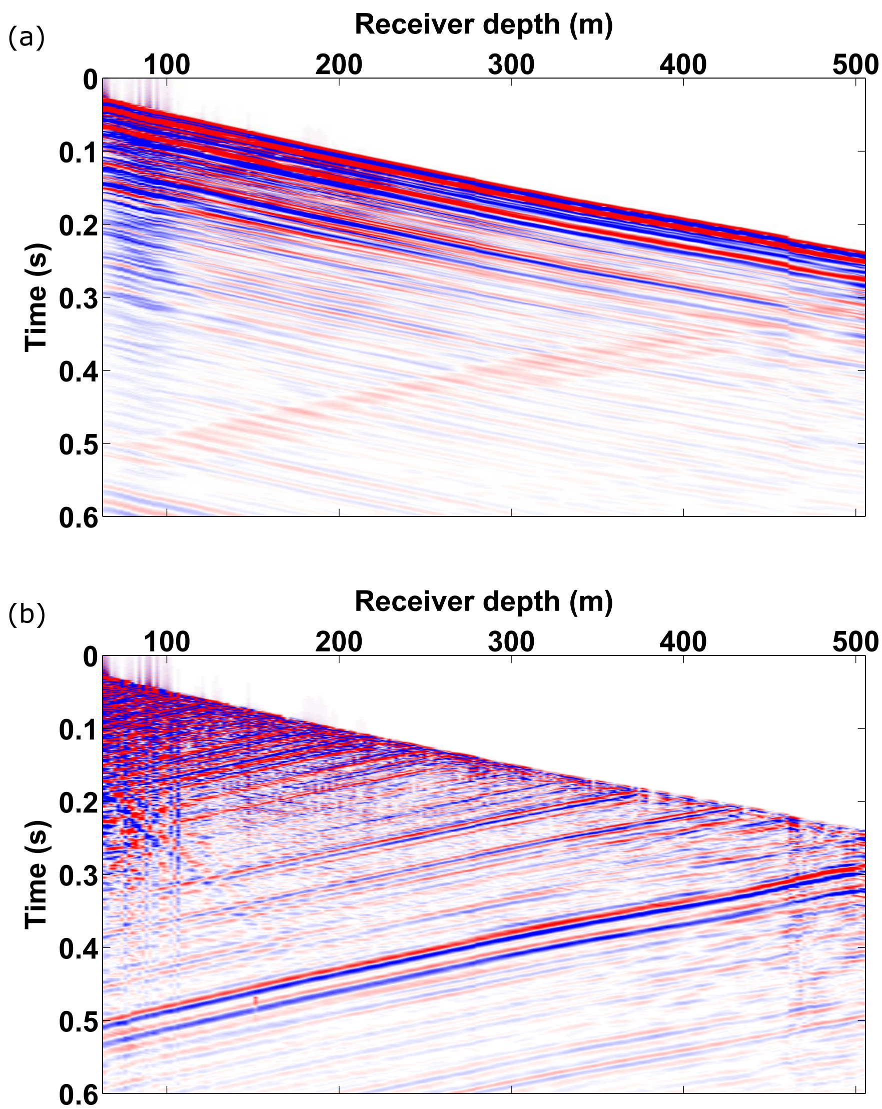

Figure 2.12: Shot gather 1; after wavefield separation using a median filter with 11 traces. (a) Downgoing wavefield, and (b) Upgoing wavefield.

2.2 Attenuation

The concept of quality factor Q is given by Equation 2.1. This shows that a rock in which the wavefield lose much energy will be a rock with low quality factor Q. Whereas, a rock where the wavefield do not lose much energy, will be a rock with high quality factor Q.

$$Q = \frac{energy}{energy\, loss} \quad per frequency\ cycle \tag{2.1}$$

The total attenuation Q can be estimated using Equation 2.2 proposed by Richards and Menke (1983),

$$\frac{1}{Q} = \frac{1}{Q_I} + \frac{1}{Q_A} \tag{2.2}$$

where: Q_I is intrinsic attenuation and Q_A is the apparent attenuation resulting from multiple scattering in a layered media.

2.2.1 Theoretical models of attenuation

Firstly, we have to consider the wave equation without attenuation for a source point at the Origin:

$$\left[\bigtriangledown^2 - \frac{1}{V^2}\frac{\partial^2}{\partial t^2}\right] G(t,x,y,z) = -4\pi\delta(t,x,y,z) \tag{2.3}$$

where V is wave speed, δ is the Dirac delta function, and G is the Green's function.

The solution of this equation is given by Equation 2.4 (Morse and Feshbach, 1953):

$$G(t,x,y,z) = \frac{\delta(t - R/V)}{R} \tag{2.4}$$

Equation 2.4 shows the wavefield to be a spherical wavefront that propagates at speed V and decays in amplitude as $1/R$ where R is the distanced travelled.

Now, if we want to consider attenuation, there are three common theoretical models: damping, complex moduli (Constant-Q) and time-dependent moduli (Viscous) (Liner, 2012). These three models are explained below:

Damping

An extra term is added to the wave equation (Equation 2.3) to obtain the damped wave equation,

$$\left[\bigtriangledown^2 - a^2\frac{\partial}{\partial t} - \frac{1}{V^2}\frac{\partial^2}{\partial t^2}\right] G(t,x,y,z) = -4\pi\delta(t,x,y,z) \tag{2.5}$$

where a^2 is the absorption parameter. The solution is given by the 3D Green's function (Morse and Feshbach, 1953):

$$G(t, x, y, z) = e^{-\alpha R} \left\{ \frac{\delta(t - R/V)}{R} + IH(t - R/V) \right\}, \tag{2.6}$$

where

$$I = \frac{a^2 e^{-\alpha R}}{2\sqrt{R^2 - V^2 t^2}} J_1 \left(\frac{1}{2} a^2 V \sqrt{R^2 - V^2 t^2} \right) \tag{2.7}$$

and where J_1 is the Bessel function of order 1, H is the Heaviside step function and the attenuation coefficient is:

$$\alpha = \frac{a^2 V}{2} \tag{2.8}$$

Equation 2.6 shows some characteristics of this kind of attenuation. The first term represents geometrical spreading (1/R) and exponential decay ($e^{-\alpha R}$); the attenuation coefficient and velocity are frequency independent.

Constant-Q

First, we start with the frequency domain Green's function,

$$G(\omega, x, y, z) = \frac{e^{i\omega R/Vo}}{R} \tag{2.9}$$

Then, we consider the complex velocity V as a function of Q:

$$\frac{1}{V} \rightarrow \frac{1}{V_0} \left(1 + \frac{i\ sgn(\omega)}{2Q} \right) \tag{2.10}$$

where sgn is the sign function. If we substitute this complex velocity into the Green's function, we obtain Equation 2.11.

$$G(\omega, x, y, z) = \frac{e^{-\alpha R} e^{i\omega R/Vo}}{R} \tag{2.11}$$

where $\omega = 2\pi f$ and the attenuation coefficient is

$$\alpha = \frac{\omega\ sgn(\omega)}{2VQ} = \frac{\pi f}{VQ} \tag{2.12}$$

The real and imaginary moduli must be related by of pair of integral equations called Kramers-Kronig relations to retain causality. These relationships lead to the equation 2.13 (Kjartansson, 1979):

$$\frac{V}{V_0} = \left(\frac{f}{f_0} \right)^{\gamma} \tag{2.13}$$

where the real velocity V is a function of frequency and attenuation (Q), V_0 is a reference velocity measured at frequency f_0 and

$$\gamma \equiv \frac{1}{\pi} \tan^{-1} \left(\frac{1}{Q} \right) \tag{2.14}$$

Kjartansson (1979) and Aki and Richards (1980) refers to equation 2.10 in the approximate form as:

$$\frac{V}{V_0} \approx \left[1 + \frac{1}{\pi Q} \, log \left(\frac{f}{f_0} \right) \right] \tag{2.15}$$

The seismic amplitude of a propagating wave at distance x is

$$A_X = A_0 e^{-\alpha x} = A_0 e^{-\dfrac{\pi f x}{VQ}} \tag{2.16}$$

Viscous attenuation

This theory is based on a version of Hooke's law that includes stress-rate and strain-rate term proposed by Liu et al. (1976):

$$\sigma + \tau_1 \dot{\sigma} = M_L (\varepsilon + \tau_2 \dot{\varepsilon}) \tag{2.17}$$

where σ and ε are stress and strain, $\dot{\sigma}$ and $\dot{\varepsilon}$ are stress and strain rates, M_L is the low frequency limit of a deformation modulus, and τ_1 and τ_2 are lower and upper relaxation times.

The upper-frequency limit is given by Equation 2.18,

$$M_U = \frac{\tau_2}{\tau_1} M_L \tag{2.18}$$

The values of τ_1 and τ_2 can be calculated from the low and high frequency observations of velocity plus one observation in the transition zone (Liner, 2012).

For this case, P-wave velocity is frequency-dependent as a consequences of Equation 2.17,

$$V = \frac{V_L \sqrt{2\Omega}}{B} \tag{2.19}$$

where V_L is the velocity at low frequency and the attenuation factor is given by Equation 2.20,

$$\alpha = \frac{\omega}{V_L}\sqrt{\frac{\Omega}{2}} \tag{2.20}$$

where, $\omega = 2\pi f$ as mentioned previously, and,

$$\Omega = A\left[\left(1 + \frac{B^2}{A^2}\right)^{1/2} - 1\right] \tag{2.21}$$

$$A = 1 - \frac{\omega^2\tau_2^2}{1+\omega^2\tau_2^2}\left(1 - \frac{\tau_1}{\tau_2}\right) \tag{2.22}$$

$$B = \omega(\tau_2 - \tau_1)/(1 + \omega^2\tau_2^2) \tag{2.23}$$

Then, Equation 2.24 is obtained by substituting Equations 2.21, 2.22 and 2.23 into equation 2.20. The relation between Q and attenuation factor is given by Equation 2.12. Equation 2.24 shows that Q is a function of frequency and relaxation parameters in this model, which means that it is no longer constant (Liner, 2012),

$$Q = \frac{1 + \omega^2\tau_1\tau_2}{\omega(\tau_2 - \tau_1)} \tag{2.24}$$

2.2.2 Seismic attenuation measurements

The methods used in this thesis are based on the constant Q theory of Kjartansson (1979). As mentioned previously, this theory predicts that the wavelet decays in time and frequency. Also, there is an associated phase rotation. According to this, the amplitude spectrum of the wavelet after a traveltime, t, will be determined by the following equation:

$$A(f,t) = |A_0(f)|e^{-\dfrac{\pi f t}{Q}} \tag{2.25}$$

where $|A_0(f)|$ is the initial amplitude spectrum. Then, the phase spectrum $\Phi(w)$ is given by the Hilbert transform:

$$\Phi(w) = H(ln(|A(f,t)|)) \tag{2.26}$$

Spectral-ratio method

The classic spectral-ratio method proposed by Spencer et al. (1982) is used to estimate Q from VSP data. First, we consider two wavelets at times t_1 and t_2 ($t_1 < t_2$) where their amplitude spectra are:

$$|A(t_1, f)| = |A(f)|e^{\dfrac{-\pi f t_1}{Q}} \tag{2.27}$$

$$|A(t_2, f)| = |A(f)|e^{\dfrac{-\pi f t_2}{Q}} \tag{2.28}$$

Then, we estimate the ratio of the amplitude spectra (Equations 2.27 and 2.28) and calculate its natural logarithm to obtain the log spectral-ratio lsr,

$$lsr(Q, \Delta t, f) = ln\frac{|w(t_2, f)|}{|w(t_1, f)|} = -\frac{\pi f \Delta t}{Q} \tag{2.29}$$

where, $\Delta t = t_2 - t_1$.

Equation 2.29 shows that lsr has a linear relationship with frequency. The value of Q between t_1 and t_2 can be computed by a least squares fit of a first order polynomial. Note, however that noise and/or notches can be a problem for the spectral division.

Figure 2.13 shows in detail each step to estimate Q using the spectral-ratio method. First, we consider two wavelets at times t_1 and t_2 as mentioned above. For this example, we extracted the wavelet from the downgoing wavefield recorded in a zero-offset VSP, using dynamite as source, for a given time window (Figure 2.13a). Details about the parameters used for Q estimations are shown in Table 4.1. Then, we compute the amplitude spectra for each wavelet and apply transmission loss correction (Figure 2.13b). Finally, we computed a least square of a first order polynomial over the log spectral-ratio to estimate Q which is extracted from the slope (Figure 2.13c).

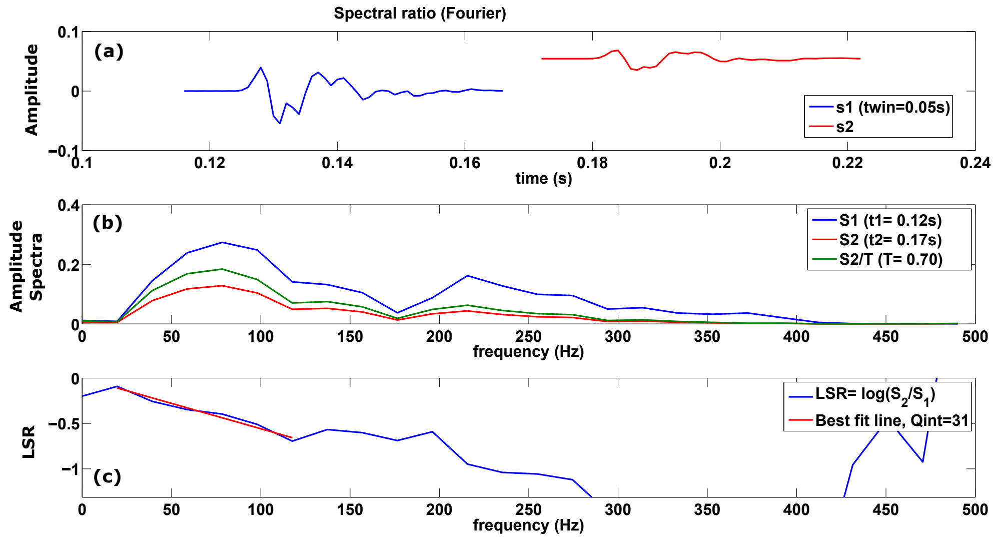

Figure 2.13: Q estimate using spectral-ratio method as detailed in Margrave (2013). (a) Wavelets at given times t_1, and t_2, where the receiver separation distance is 120 m and the time window is 0.05 s. (b) Amplitude spectra of each wavelet; and (c) linear fit over the spectral-ratio.

Spectral Matching method

For this method we compute the amplitude spectrum for a given time window of each wavelet. Then, Q is estimated by minimizing the difference between the amplitude spectra (Equation 2.30). This means that we attenuate the amplitude spectrum of wavelet at t_1 until it is close to the amplitude spectrum at t_2 (Margrave, 2013).

$$Obj = \left\| |\bar{A}(t_2, f)| - |\bar{A}(t_1, f)| e^{\dfrac{-\pi f \Delta t}{Q}} \right\| \tag{2.30}$$

Further details about Q estimations using spectral matching method are shown in Figure 2.14. Similar to the previous method, we consider two wavelets (Figure 2.14a), and compute their amplitude spectra (Figure 2.14b). Then, we match the amplitude spectra of wavelet at times t_1 and t_2 by attenuating the amplitude spectra of the wavelet at time t_1 (Figure 2.14c). Finally, Q is estimated by minimizing the objective function given by Equation (2.30) which value corresponds to the red asterisk for this specific case (Figure 2.14d).

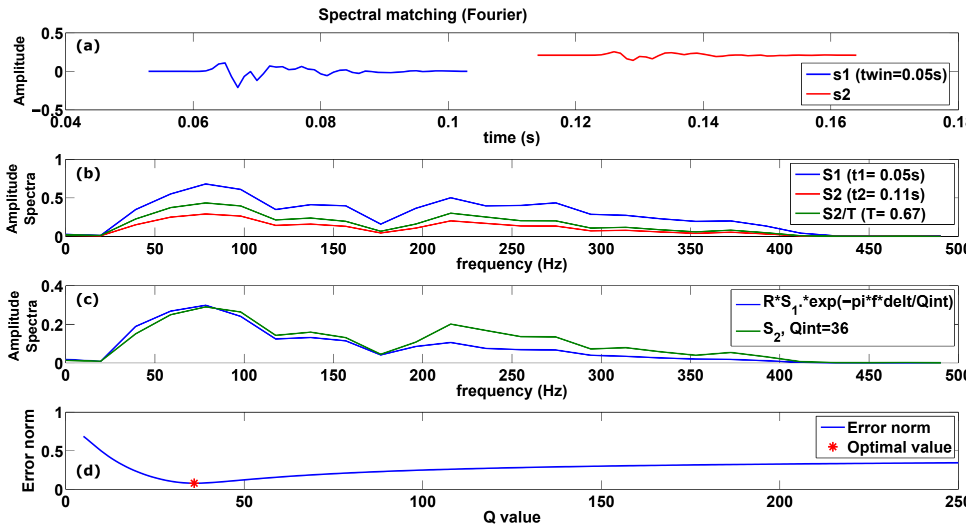

Figure 2.14: Q estimate using spectral matching method as detailed in Margrave (2013). (a) Wavelets at given times t_1, and t_2, where the receiver separation distance is 120 m and the time window is 0.05 s, (b) Amplitude spectra for each wavelet, (c) Amplitude spectra matching, and (d) Minimum of the objective function (Equation (2.30)).

2.2.3 Q versus offset method

The Q versus offset (QVO) method proposed by Dasgupta and Clark (1998) is a technique where Q values are estimated from surface seismic common midpoint (CMP) gathers by using the spectral-ratio method. They noticed that the spectral-ratio slopes change with offset due to different raypath geometries. The key point is how to convey all these values into a single value for a given common midpoint. To answer this question, they assumed that the slope of spectral ratio changes linearly with offset squared because reflection travel time changes are also dependent on offset squared. Therefore, the Q value for the zero-offset condition can be estimated by computing the intercept of a linear fit over the slope versus offset squared.

2.2.4 Seismic attenuation versus velocity

According to Mavko and Nur (1979) and Winkler and Nur (1982), P-wave attenuation in partially saturated rocks is much stronger than shear wave attenuation. However, in fully saturated rocks shear wave attenuation is stronger than P-wave attenuation. Figure 2.15 shows a crossplot of Q_S/Q_P versus V_P/V_S for sandstone from Winkler and Nur (1982). Here, there are three different fields: dry, partially saturated and fully saturated rocks. The authors obtained a more accurate degree of saturation than V_P/V_S (Domenico, 1976), by combining velocity and attenuation data. The value $Q_S/Q_P = 1$ can be used as a reference to separate partial saturation ($Q_S/Q_P > 1$) from total saturation ($Q_S/Q_P < 1$).

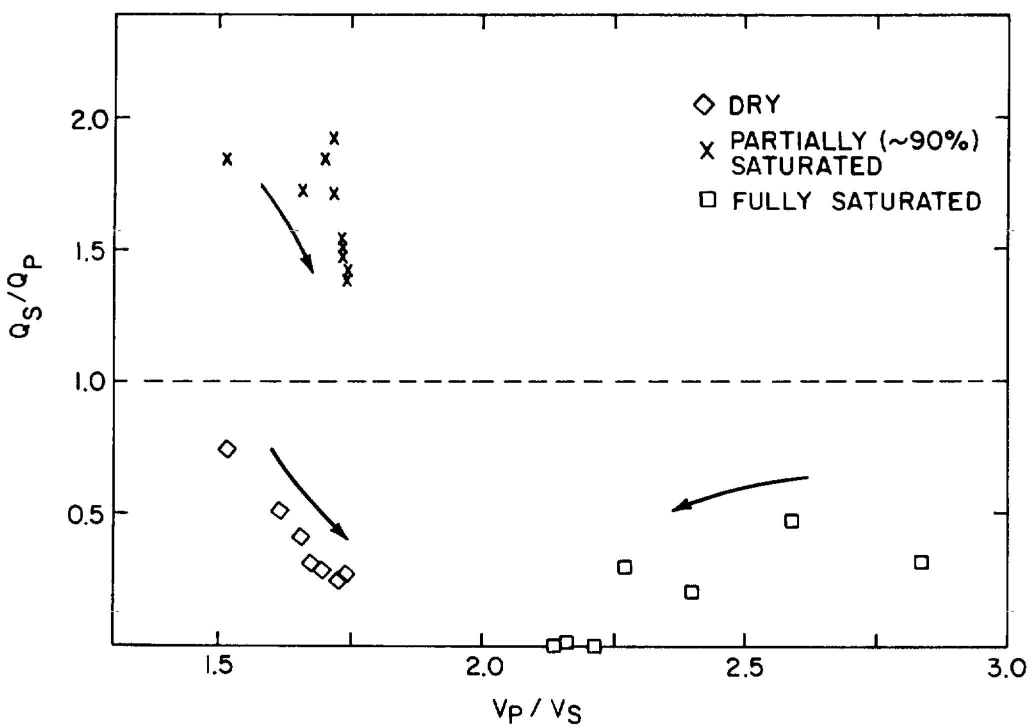

Figure 2.15: Crossplot Q_S/Q_P versus V_P/V_S for Massilon sandstone. From Winkler and Nur (1982).

Chapter 3

SYNTHETIC VSP DATA

3.1 Zero-offset VSP data

Zero-offset VSP data were modelled using blocked well log data (Figure 3.1). The data corresponds to a well located 200 m from the VSP survey in case study 1 (Well A), and includes density and P-wave velocity (Figure 3.1a and 3.1b). The input Q used for this model is shown in Figure 3.1c. These values were obtained by computing a harmonic average between velocity and density logs given by equation 3.1,

$$\frac{1}{Q} = \frac{1}{Q_v} + \frac{1}{Q_\rho} \tag{3.1}$$

where,

$$Q_v(z) = Qmin * \left(\frac{v_P(z) - v_0}{v_1 - v_0}\right) + Qmax * \left(\frac{v_P(z) - v_1}{v_0 - v_1}\right) \tag{3.2}$$

and

$$Q_\rho(z) = Qmin * \left(\frac{\rho(z) - \rho_0}{\rho_1 - \rho_0}\right) + Qmax * \left(\frac{\rho(z) - \rho_1}{\rho_0 - \rho_1}\right) \tag{3.3}$$

$Qmin$ and $Qmax$ are the minimum and maximum values allowed for the computation; v_0 and v_1 are the minimum and maximum velocities; ρ_0 and ρ_1 are the minimum and maximum densities (Margrave, 2013).

For the survey, we placed the source at the surface and receivers were located from 10 to 600 m depth at intervals of 10 m (Figure 3.2). Then, we computed a zero-offset VSP response using a minimum phase wavelet with a dominant frequency of 30 Hz (Figure 3.3). For this modelling, we did not consider internal multiples or noise. The downgoing and upgoing wavefield are computed for each layer using a single step wavefield extrapolation in the frequency domain (Ganley, 1981; Margrave, 2013).

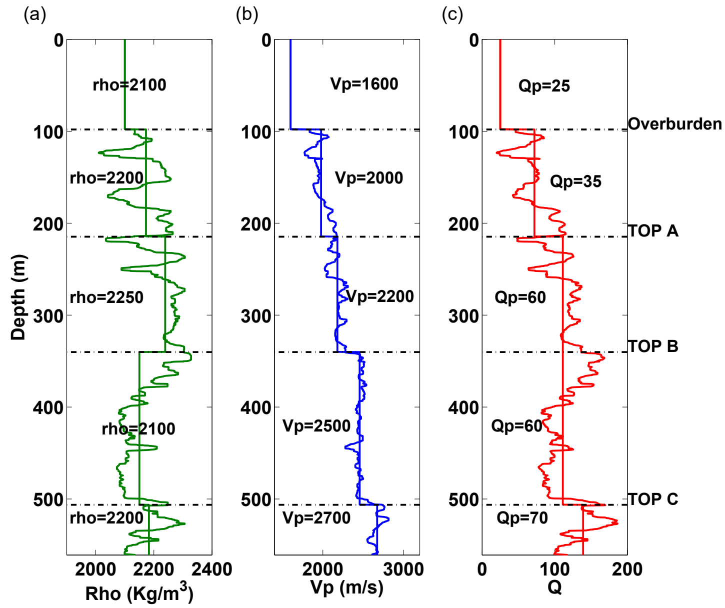

Figure 3.1: Density and P-wave velocity from well A. The Q values input for the forward modelling were computed using a harmonic average between density and velocity logs. Data were blocked into five homogeneous layers based on the formations tops.

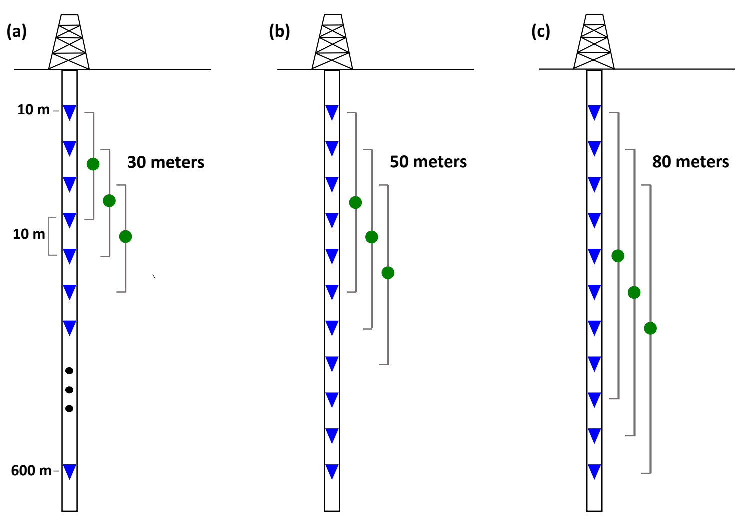

Figure 3.2: Synthetic VSP geometry. Using a separation distance of (a) 30 m for the Q analysis, (b) 50 m and (c) 80 m.

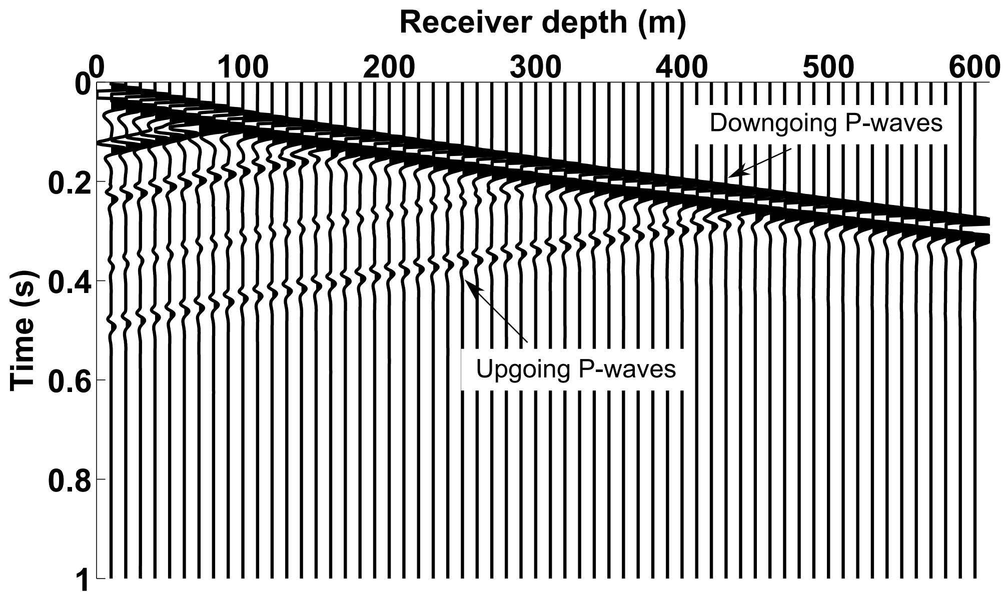

Figure 3.3: Synthetic VSP seismic gather using *vspmodelq* function from the Crewes Matlab toolbox.

3.1.1 Q_P estimation from direct downgoing P-waves

We estimated Q from the direct downgoing P-wave arrivals shown in Figure 3.3, using the spectral matching method. For the Q analysis, we used a separation distance of 30 m. The estimated Q was set midway between the two receivers, as shown in Figure 3.2 a. We repeated this for each trace down to the deepest receiver. Then, we increased the separation to 50 m and 80 m (Figure 3.2 b and c). Also, we used a frequency bandwidth of 10-50 Hz. A time window of 0.15 s around the direct arrivals was defined.

Figure 3.4 shows the results for these three cases. In the first case, we observed a good match between the input Q and the estimated Q (Figure 3.4 a). However, vertical resolution decreased when we increased the separation to 50 m and to 80 m (Figure 3.4 b and c, respectively). For example, in Figure 3.4 c it is hard to differentiate Q between the first two layers. Also, Q within the deepest layer is overestimated in all three cases. Notice that this layer has a high Q value of 70, which means it has relatively low attenuation. We may need to use a larger separation distance in order to determine the attenuation when we analyze real data.

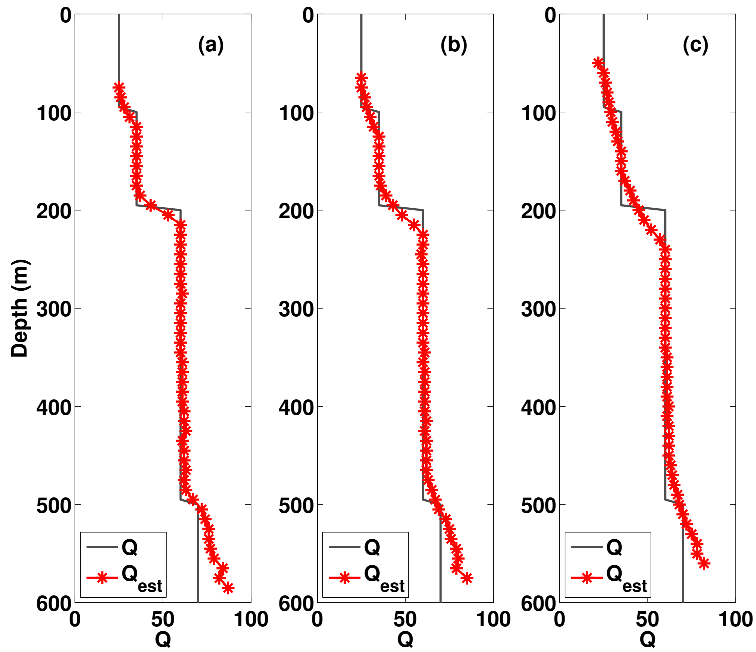

Figure 3.4: Q_P estimates from downgoing P-waves, using separation distances of (a) 30 m, (b) 50 m and (c) 80 m.

3.1.2 Q_P estimation from upgoing P-waves

In this study, we also wanted to determine Q for the near-surface layers. To achieve this, we estimated Q from the upgoing P-waves generated from the deepest reflector indicated in Figure 3.3. We selected this event because it crosses most of the time-depth window. Figure 3.5 shows the results obtained using the same set of separation distances as used for the downgoing Q analysis. Similar comments can be drawn from these results, in which we lose Q resolution when the trace separation is increased. The advantage of this procedure is that more estimates through the near-surface interval were added, particularly for the short separation distance of 30 m. We combined these two estimates in order to have a better understanding of Q variations through the layered sequence.

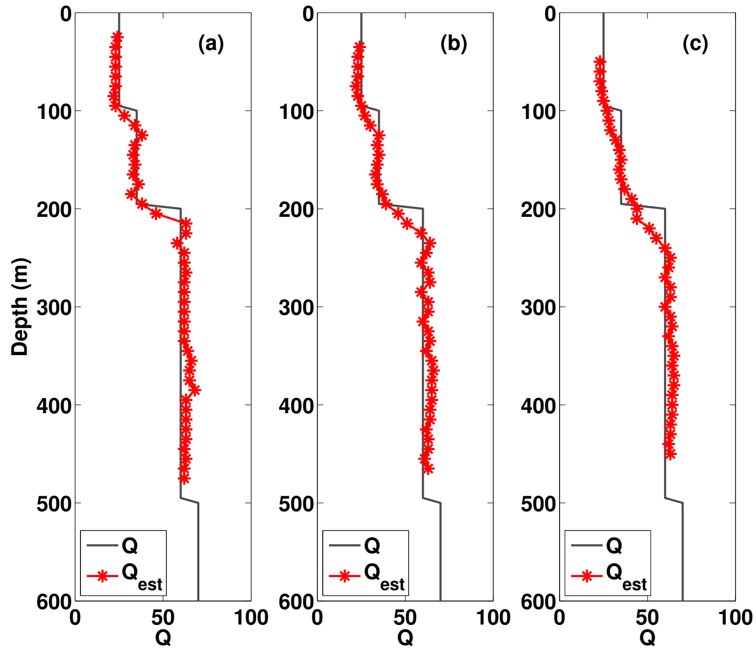

Figure 3.5: Q_P estimates from upgoing P-waves using a separation distance of (a) 30 m, (b) 50 m and (c) 80 m.

3.2 Walkaway VSP data

We computed a forward model in two dimensions using NORSAR2D. This software uses ray-tracing algorithms based on Snell's law. The modelling is divided into two parts, the kinematic ray tracing and dynamic ray tracing. The first calculates the location of the ray paths and the traveltimes. The second one calculates the dynamic properties of the seismic wavefield, such as the geometrical spreading factors, wavefront curvature, and amplitude coefficients.

The geological model used in this case is obtained from well logs that include density, P-wave and S-wave velocities (Figure 3.6). The well log data corresponds to a well located 500 m from the VSP survey in case study 1 (Well B). We made the overburden parameters increase linearly with depth (Figure 3.7 a, b and c). The input Q was the same as used in the previous model (Figure 3.7 d). For the survey, we used the acquisition parameters from the study case 1 (Table 1.1). Fourteen shot points and 222 receiver's from 60 to 500 m depth at intervals of 2 m. The wavelet is minimum phase with a dominant frequency of 40 Hz. For computing this data, we did not consider internal multiples or noise.

In Figure 3.8, we observe the ray-tracing for the mode-converted upgoing S-waves. The seismic wavefield travels downward as P-waves, and convert to S-wave at the Top formation D. We are interested in this event because it shows high amplitudes. We can also observe that the common conversion points (CCP) are very close to the bottom of the well, within a range of 125 m of lateral distance.

Figure 3.9 shows the source gather 1. Here, we observe the direct downgoing P-waves and downgoing S-waves recorded in the vertical and horizontal components. The downgoing P-waves shows more energy in the vertical component because its propagation is longitudinal. In comparison, the downgoing S-wave shows more energy in the horizontal component due to its transverse mode. We also observed some interruptions in the downgoing P-waves and S-waves where there are not signal. This may be due to the ray bedding at the interfaces where the ray does not reach some receivers, especially when changing from low to high velocities. Figure 3.10 and 3.11 shows that the mode-converted upgoing S-waves increase in energy as we increase the source offset. Also, we observed that the mode-converted upgoing S-waves coming from the Top formation D shows a polarity reversal at 300 m depth for the source gather 6 (Figure 3.10 b). This effect might be the results of the AVO response for the converted-wave mode. The seismic gather of the next source point does not show this problem (Figure 3.11 b).

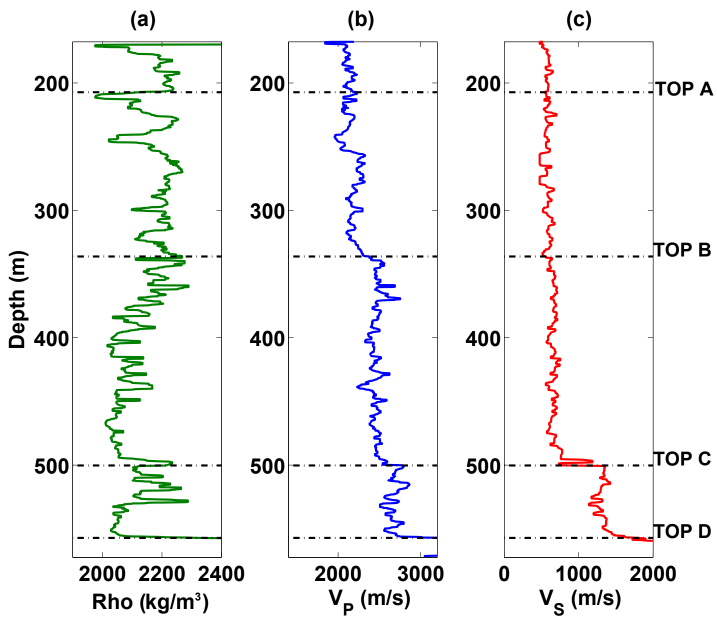

Figure 3.6: Well logs from well B (Case Study 1). (a) Density, (b) P-wave and (c) S-wave velocities.

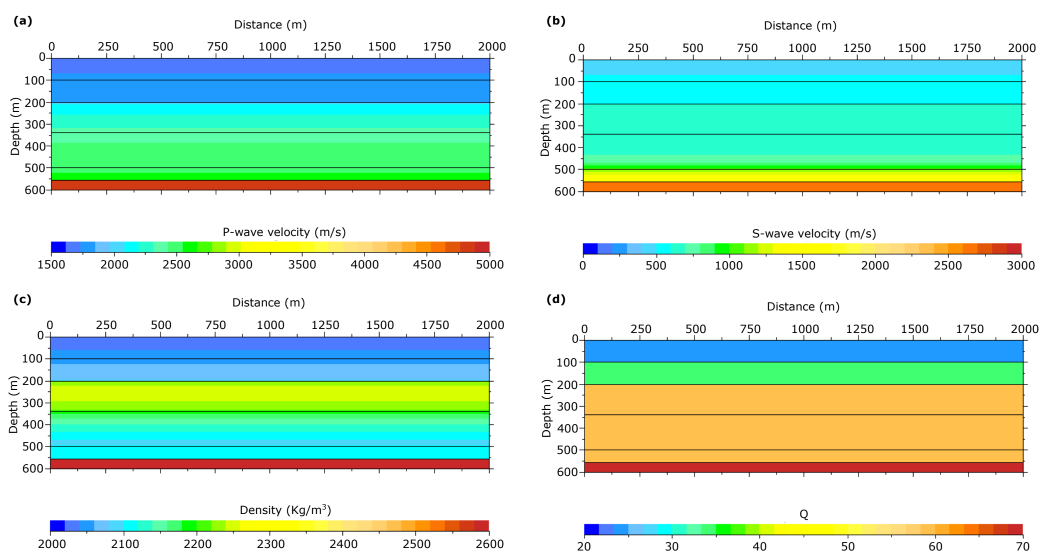

Figure 3.7: Geological model using NORSAR.

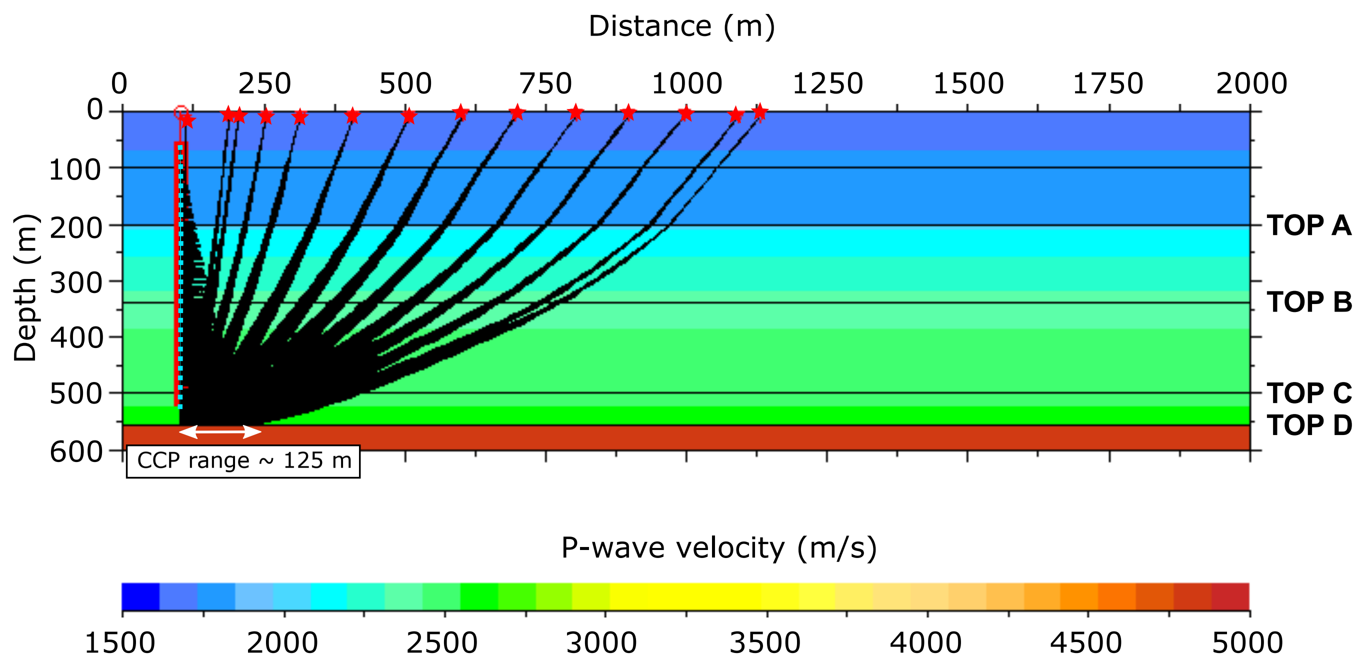

Figure 3.8: Ray-tracing using Norsar2D. Mode-converted upgoing S-waves coming the Top formation D.

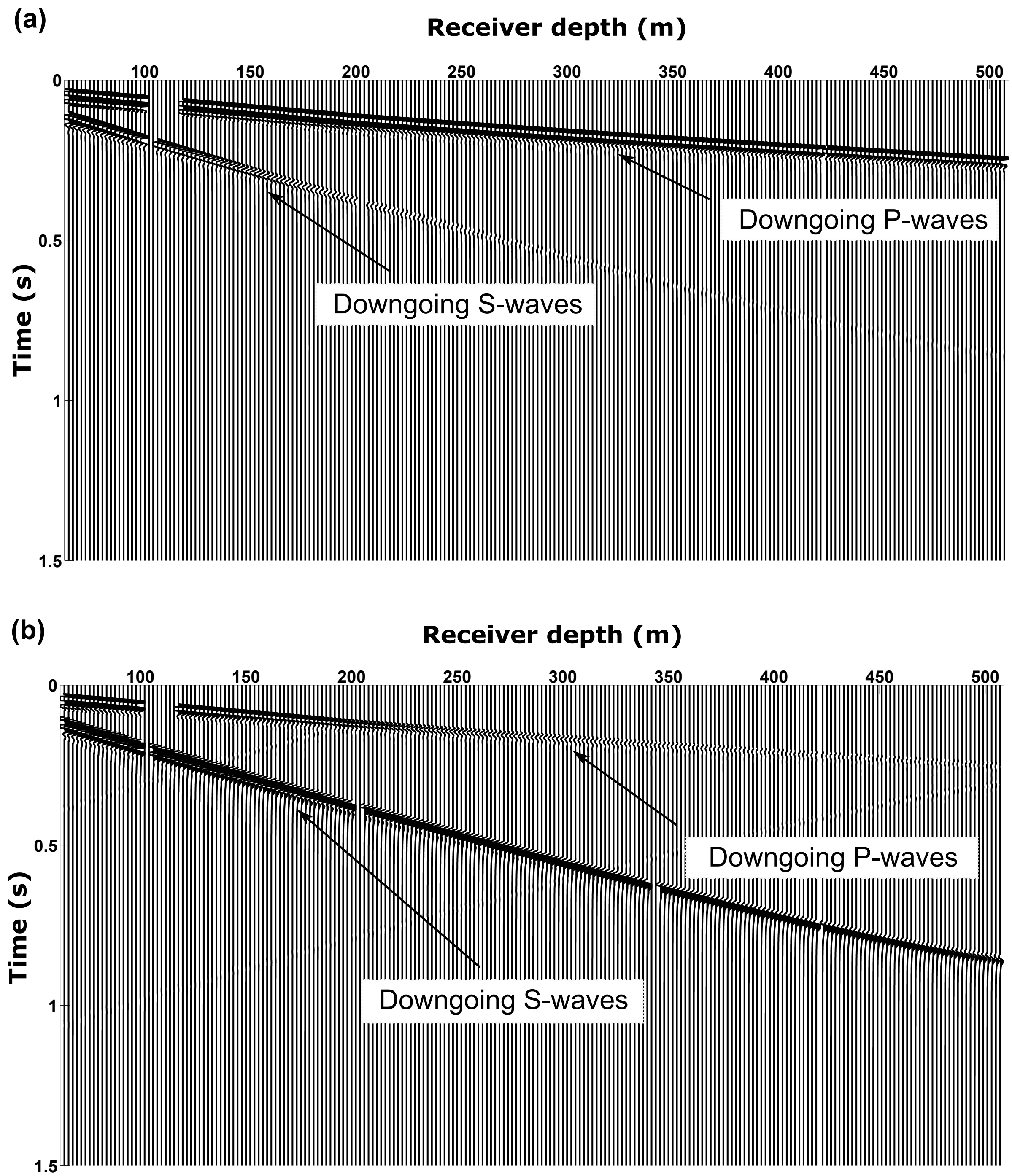

Figure 3.9: Synthetic source gather 1 at 12 m offset from the well using NORSAR2D. (a) Vertical and (b) horizontal components.

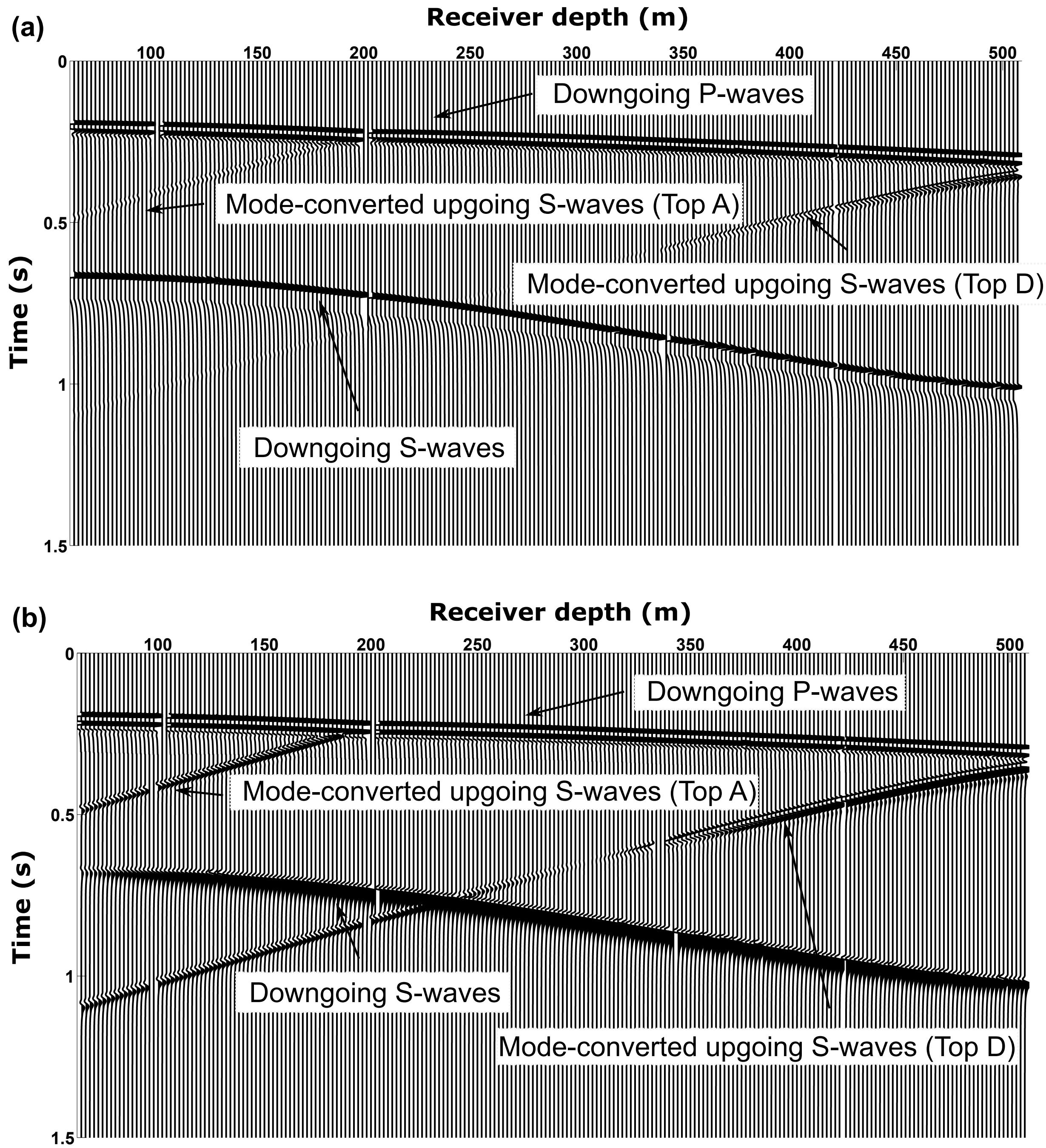

Figure 3.10: Synthetic source gather 6 at 300 m offset from the well using NORSAR2D. (a) Vertical and (b) horizontal components.

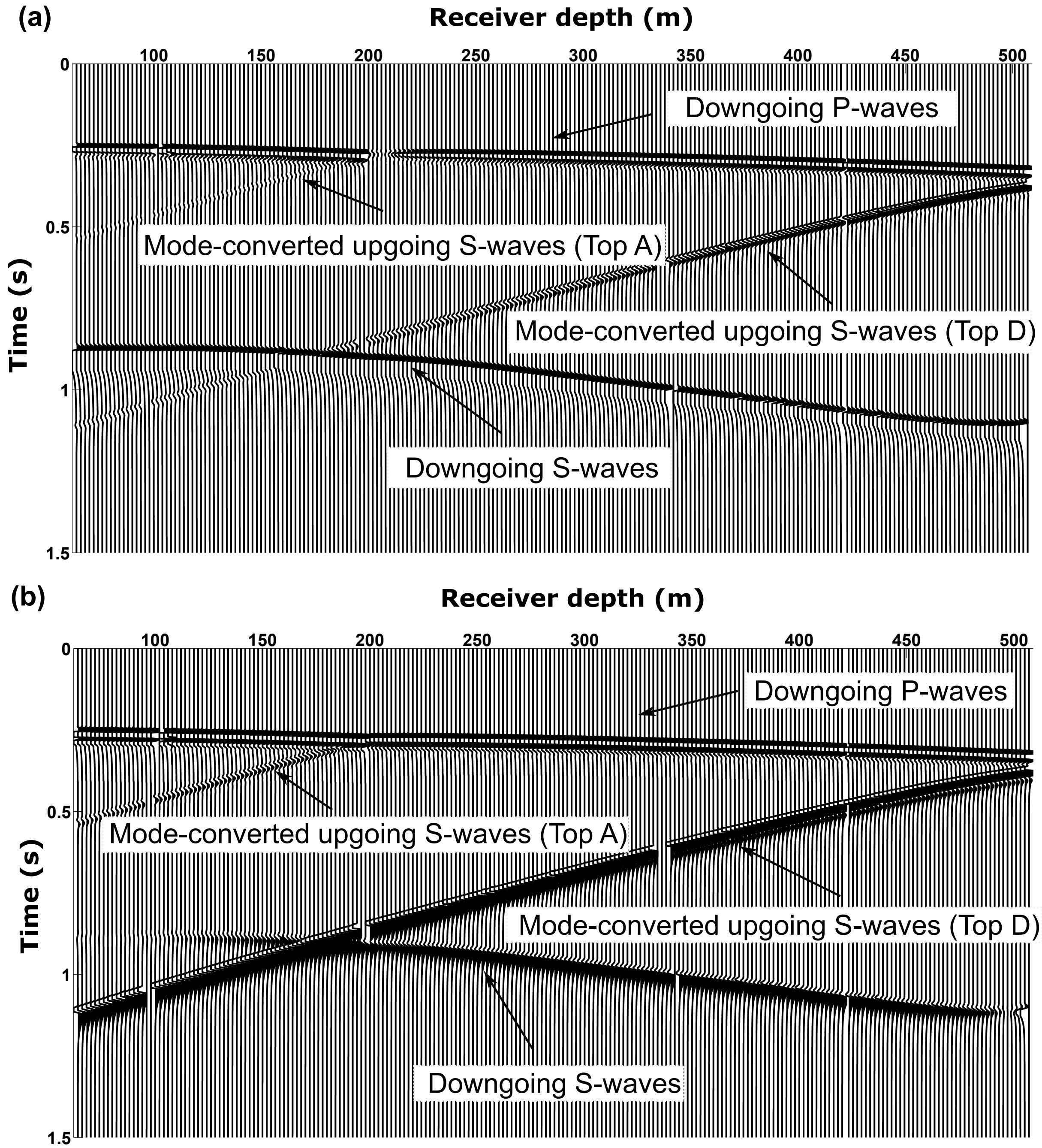

Figure 3.11: Synthetic source gather 7 at 400 m offset from the well using NORSAR2D. (a) Vertical and (b) horizontal components.

3.2.1 Q_S estimates from direct downgoing S-waves

We estimated Q_S using the direct downgoing S-wave shown in source gather 1 (Figure 3.9). For the Q analysis, we used the spectral-matching method with a separation in receiver depths of 40 m: a frequency bandwidth of 8-80 Hz, and a time window of 0.2 s. Results are shown in Figure 3.12. As one can see, there is a good match between the input Q and the estimated Q. This shows that downgoing S-waves, whenever available, might provide the necessary information to compute Q_S values. However, the direct downgoing S-wave is hard to identify in field data.

3.2.2 Q_S estimates from mode-converted upgoing S-waves

We estimated Q_S from the mode-converted upgoing S-waves for source points 1 to 14. For Q analysis, we used the spectral-matching method with the previous parameters. Results are shown in Figure 3.13. In this case, we observe the estimated Q_S values to increase with the source offset probably because the wavefield travels horizontally in the same layer for a longer period of time which causes less attenuation. We also noticed that all estimates share a similar trend except for source point 6 (dark blue line). Results here show very high values from 100 to 300 m depth, and very low values from 300 to 500 m depth. As we mentioned previously, this may be related to PS-AVO effects.

All the estimates were converted to zero-offset conditions using the QVO method. For this case, we used converted-waves from VSP data to estimate Q_S. Since the common conversion points are very close together (Figure 3.8), we assumed that all mode-converted upgoing S-waves recorded at a given receiver depth were generated at a similar conversion point. Then, based on this condition we were able to use the QVO method. Figure 3.14a shows Q_S versus offset squared at 193 m depth. These values show a linear trend except for those from source point 6, where the estimated Q_S is far from the rest. This causes an error in the measured gradient (red line). If we remove this value, we obtain a better linear fit (Figure 3.14b). As we mentioned in chapter 2.2.3, the Q_S at zero-offset corresponds to the intercept of the linear fit (red asterisk) estimated at each depth. Results are shown in Figure 3.15. After removing the source point 6 value, our final estimation matches very closely the Q values of the original model.

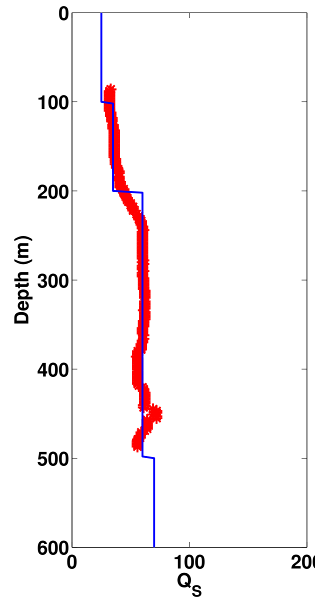

Figure 3.12: Q_S estimates from the direct downgoing S-waves using source point 1.

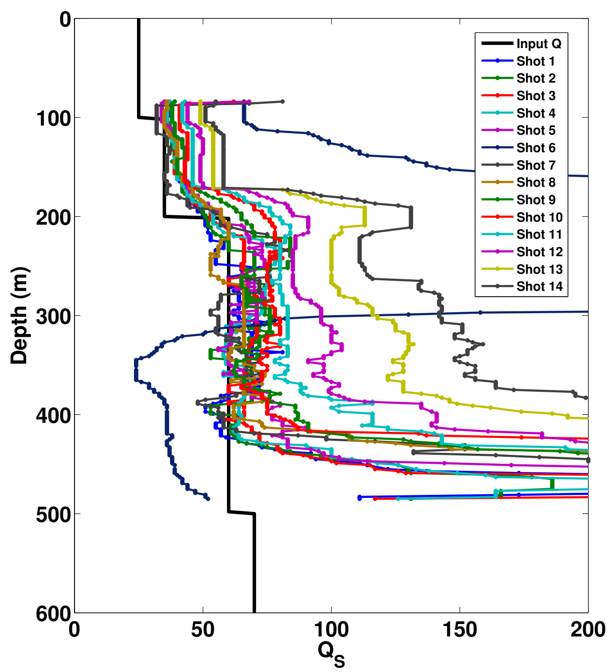

Figure 3.13: Q_S estimates from mode-converted upgoing S-waves using source points 1 to 14.

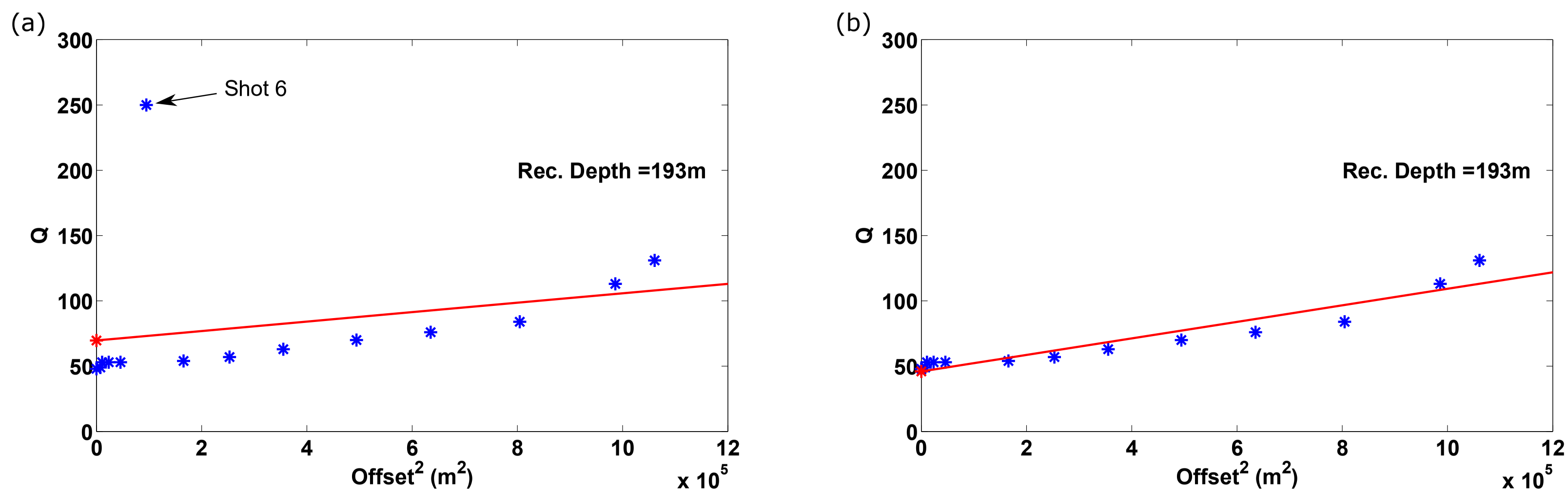

Figure 3.14: Offset square cross-plot for Q at receiver depth = 193 m. (a) Including all shot points 1 to 14, and (b) without source point 6.

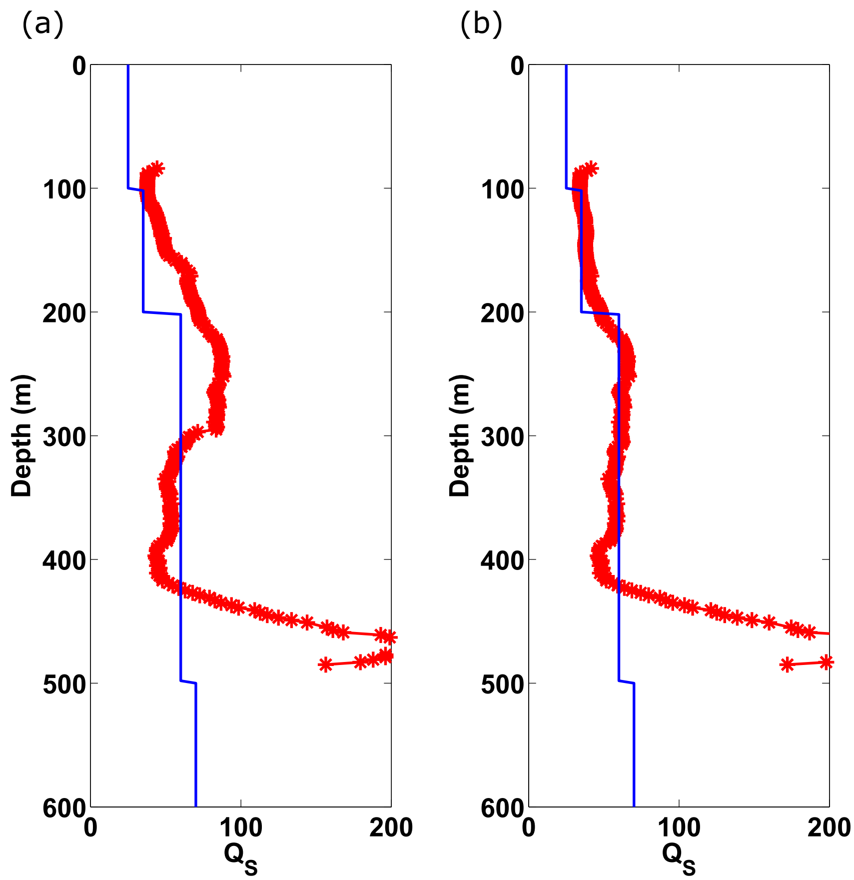

Figure 3.15: Q_S estimates using the QVO method. (a) Including all source points 1 to 14, and (b) without source point 6.

Chapter 4

CASE STUDY 1

4.1 Introduction

A walkaway VSP located in an oil sand field in Western Canada was available for this study. As we mentioned in the chapter 1.3, fourteen source points were acquired; first, using 0.125 kg of dynamite at 9 m depth for the energy source, and then from an EnviroVibe source or vertical vibrator, generating a linear sweep of 10-300 Hz over 20 s (Figure 1.4). Receivers were placed at 2 m spacing from 60 to 500 m depth (Table 1.1).

4.2 Zero-offset VSP data

4.2.1 Data processing and analysis

The processing flow used for estimation of Q from the zero-offset VSP data is shown in Figure 4.1. First, we input the geometry, the first break picks, and the upgoing events. Then, we computed the interval velocity. Next, we rotated the receiver components using hodogram analysis. To this data, two rotations were applied. For the first rotation, the horizontal components H1 and H2 were rotated into the source-receiver plane to obtain Hmax and Hmin. For the second rotation, the horizontal component Hmax, obtained from the first rotation, and the vertical component z, were rotated in the plane defined by the well and the source (Hinds et al., 1996) (See further details in chapter 2.1.2). Later, we separated the wavefields using a median filter. Finally, we estimated Q from the downgoing and upgoing wavefields using the spectral matching method.

Figure 4.2a shows the vertical component of the dynamite VSP data from source point 1, the nearest source, offset 12 m from the well. In this figure, high-amplitude downgoing P-waves are the first arrivals. Also, we observed a high-amplitude upgoing P-wave from a reflector which crosses the complete time-depth plot just below the deepest receiver. We are interested in these two events for measuring P-wave attenuation. Preliminary analysis was done by computing the amplitude spectra of the direct downgoing P-waves, using a cosine-tapered window and the delimited data in the green box of Figure 4.2a. The spectra shown in Figure 4.2b shows that the frequency bandwidth decreases with depth, a clear signature of seismic attenuation. Also, there is a notch at 190 Hz that could be a source ghost. In comparison, Figure 4.3a shows the horizontal component (Hmax) for the 12 m source offset, acquired with a dynamite source. Here, we observed an event assumed to be S-waves that have a narrow frequency bandwidth (Figure 4.3b).

Figure 4.4a shows the vertical component of the Envirovibe VSP data from source point 1 at 12 m from the well. Here, we observed the downgoing and upgoing wavefield. There is noise interfering with the upgoing wavefield that we assumed to be tube wave. The amplitude spectra was computed for the downgoing wavefield using a cosine-tapered window (Figure 4.4b). This figure shows the frequency bandwidth used to acquire the data from 10-300 Hz which is decreasing with depth. In comparison, Figure 4.5a shows the horizontal component (Hmax) for the 12 m source offset, acquired with the EnviroVibe source. In this figure, we observe direct downgoing S-waves. The amplitude spectra of these traces (Figure 4.5b) suggest greater attenuation effects for this wave-mode. This agrees with previous studies (Armstrong et al., 2001; Hardage, 1985) that indicate the S-waves attenuate faster than P-waves. Notice that the S-wave data has a narrow frequency bandwidth compared to the P-wave data (Figure 4.2b), with significant losses in bandwidth even before arriving at the shallowest receiver depth (60 m). Also, the S-wave has lost even more energy and bandwidth below 300 m depth. This makes it difficult to estimate Q_S from the deepest receivers in the well.

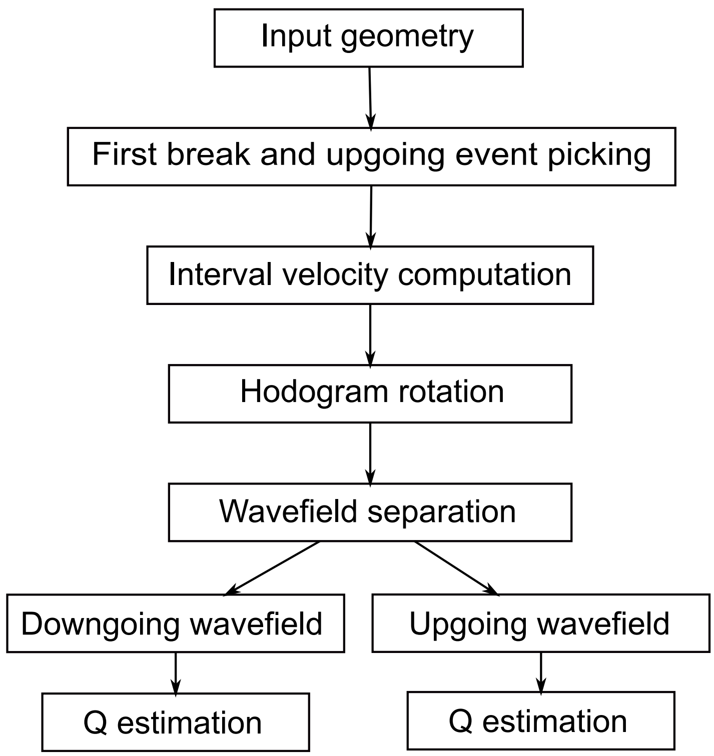

Figure 4.1: Processing flow to estimate Q from a zero-offset VSP.

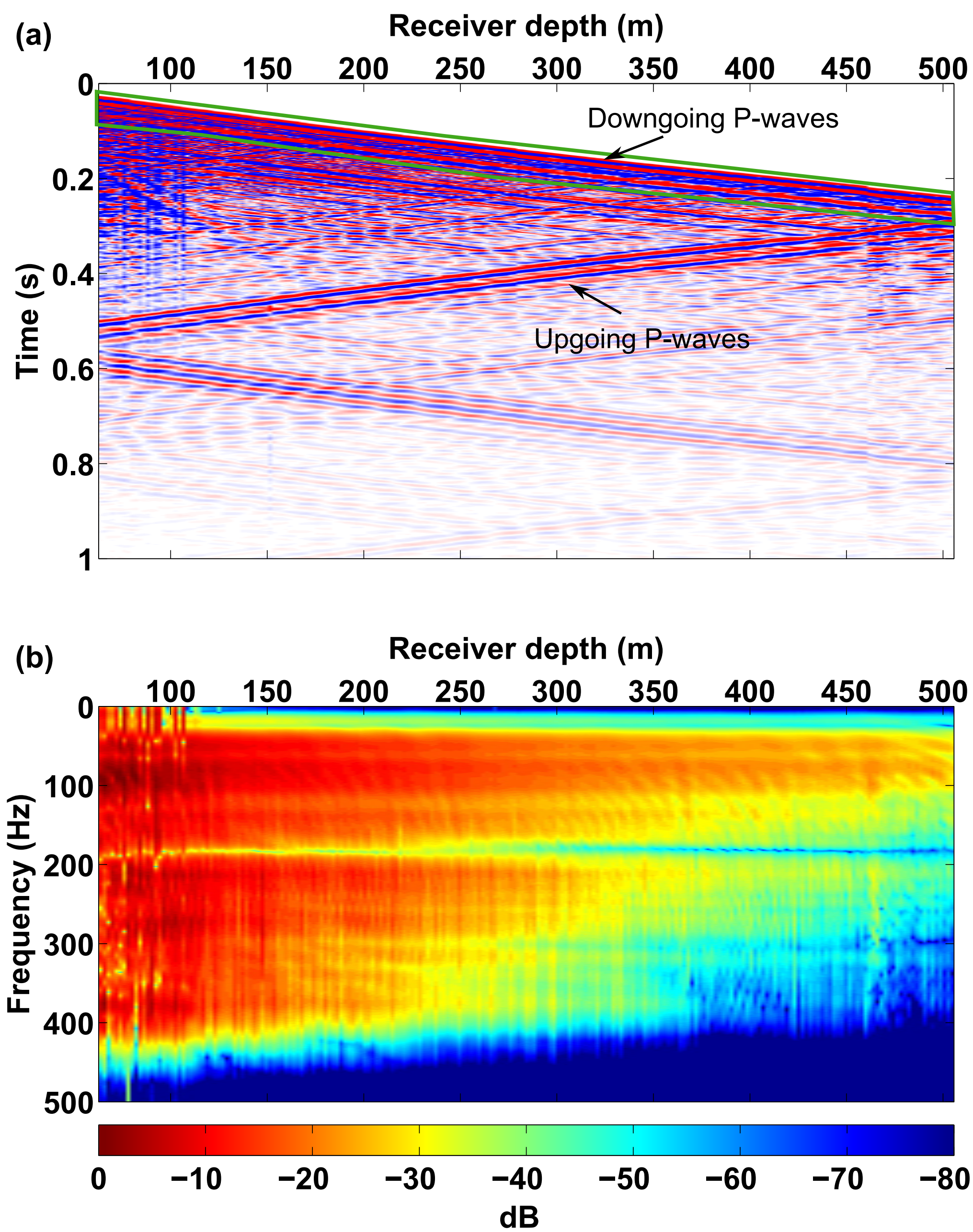

Figure 4.2: (a) Dynamite VSP data from source point 1 at 12 m from the well (vertical component). (b) Amplitude spectra for the downgoing P-wave using a cosine-tapered window and the delimited data in the green box.

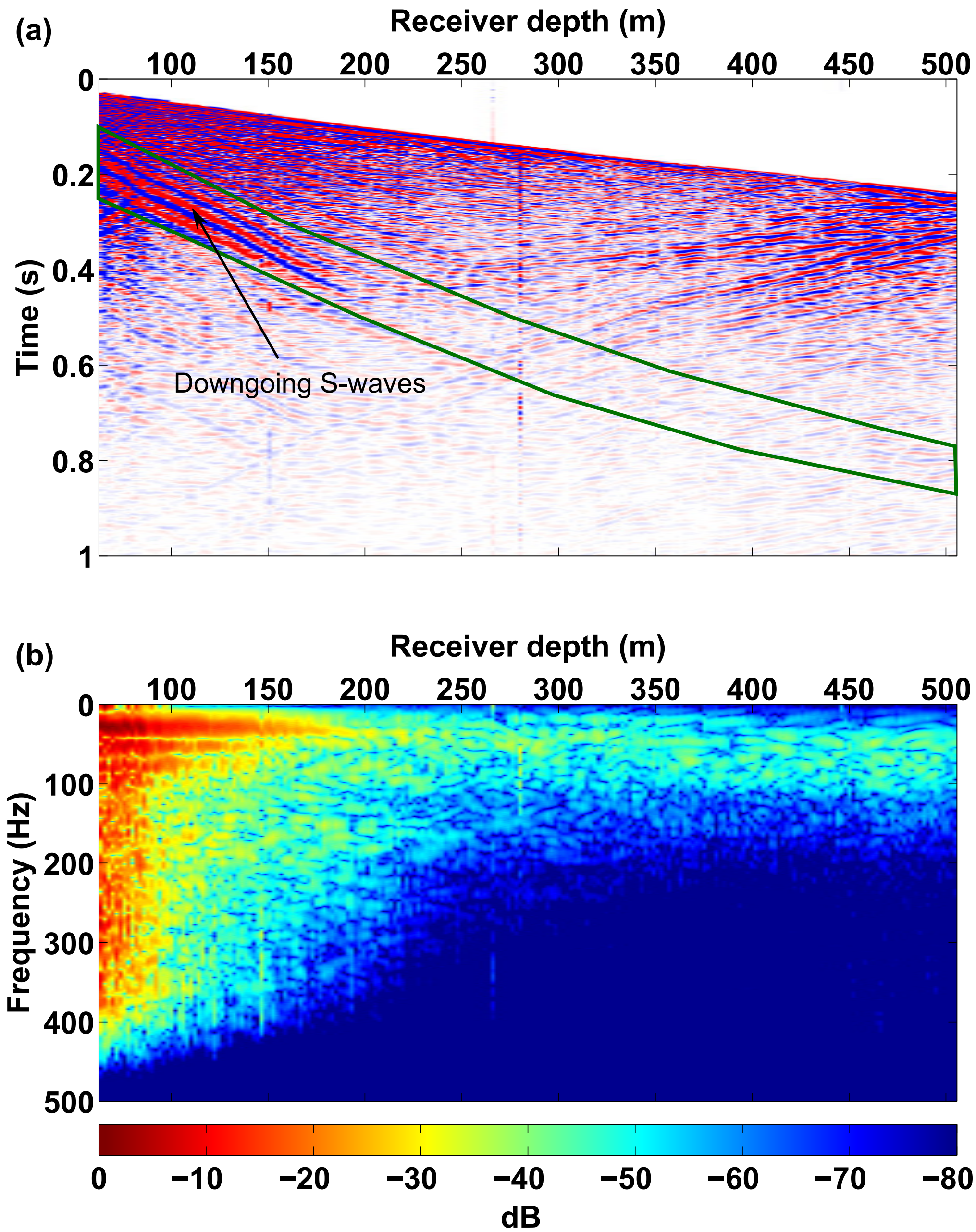

Figure 4.3: (a) Dynamite VSP data from source point 1 at 12 m from the well (horizontal component - Hmax). (b) Amplitude spectra for the downgoing S-wave using a cosine-tapered window and the delimited data in the green box.

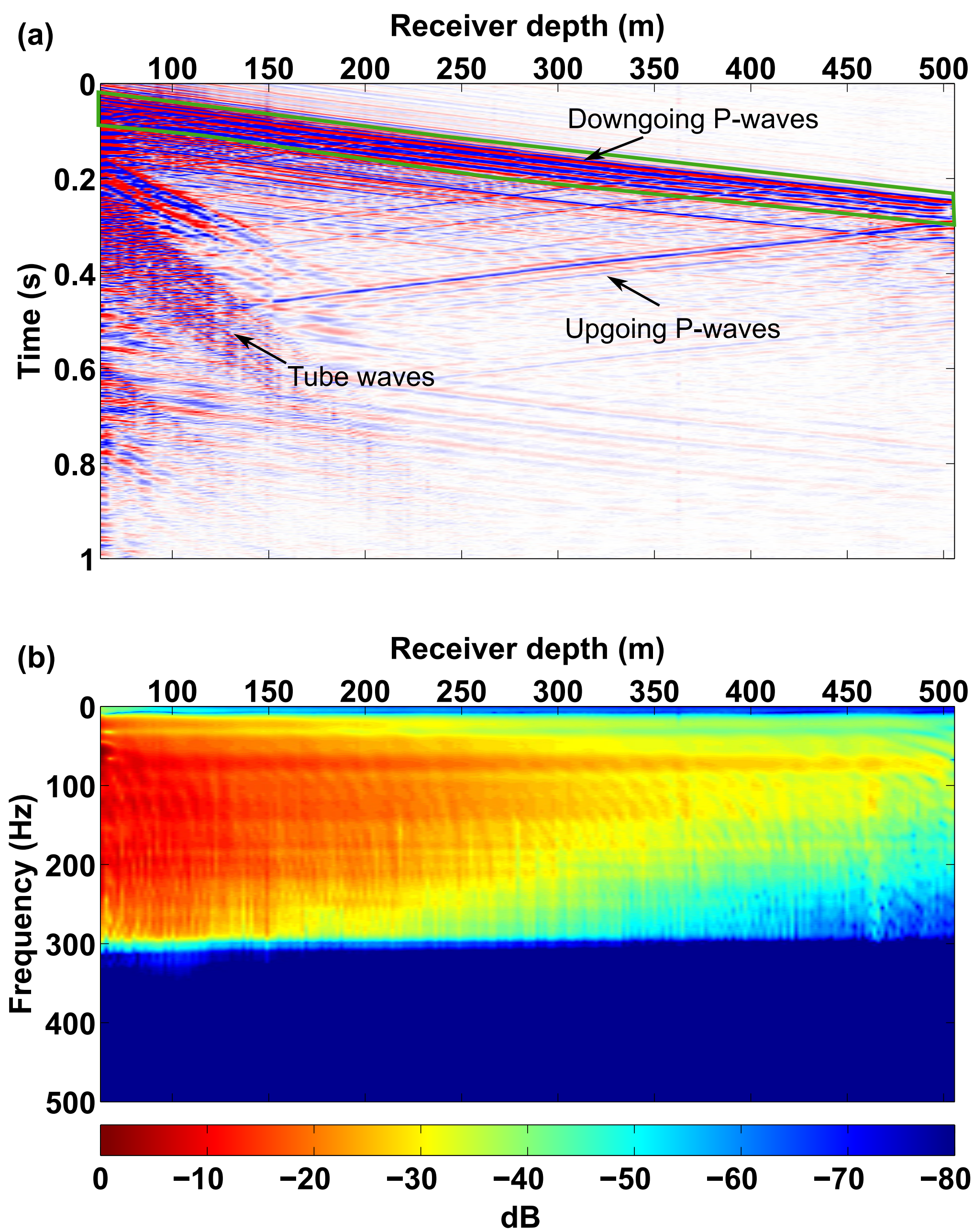

Figure 4.4: (a) Envirovibe VSP data from source point 1 at 12 m from the well (vertical component). (b) Amplitude spectra for the downgoing P-wave using a cosine-tapered window and the delimited data in the green box.

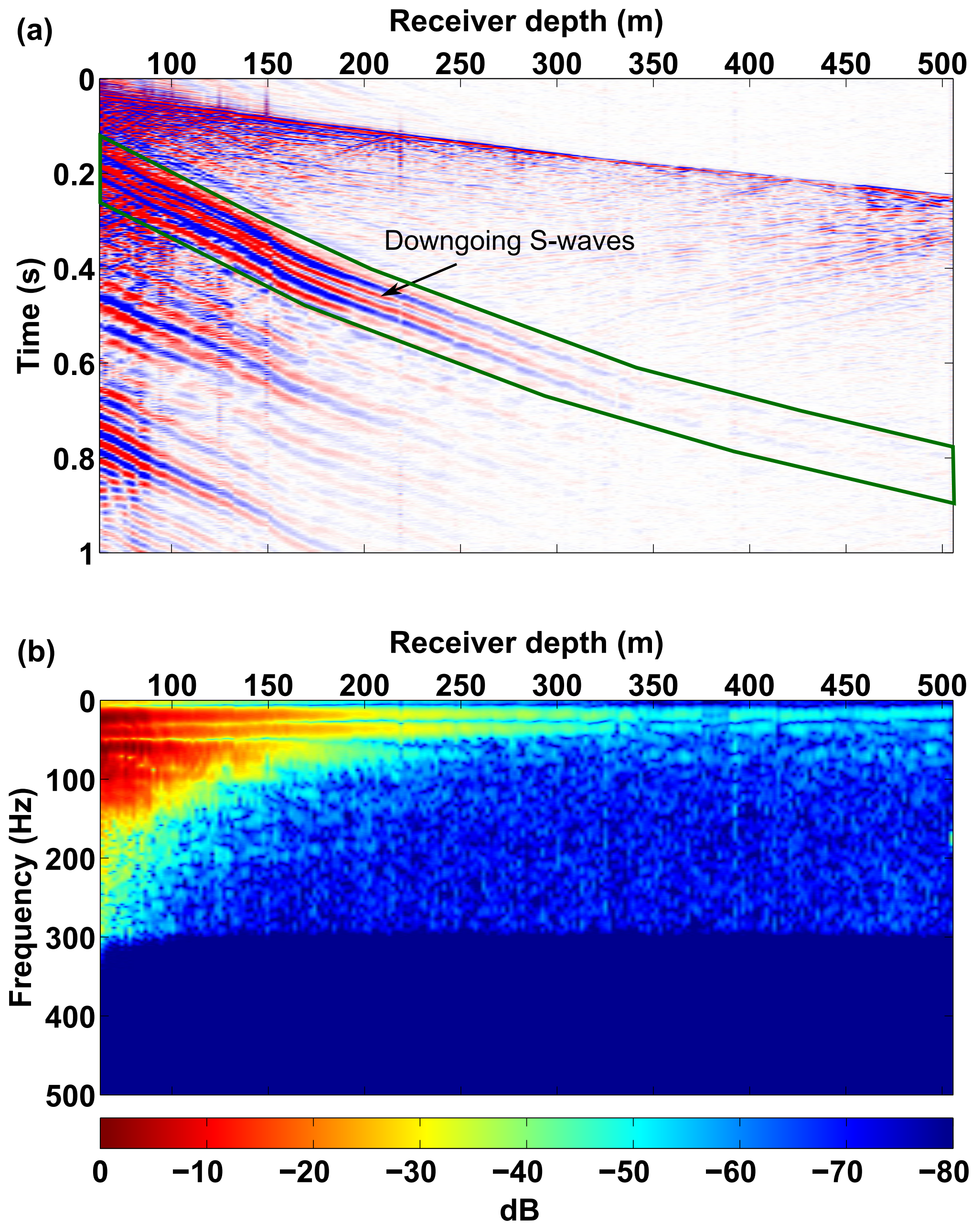

Figure 4.5: (a) Envirovibe VSP data from source point 1 at 12 m from the well (horizontal component - Hmax). (b) Amplitude spectra for the downgoing S-waves using a cosine-tapered window and the delimited data in the green box.

4.2.2 Q analysis and results

Prior to the Q analysis, we estimated the wavelength, λ, given by the equation $\lambda = V/f_{dom}$, where the velocity V is obtained from well logs (Figure 3.6). We used a constant value for the dominant frequency, f_{dom} obtained from the first arrivals recorded in the VSP data. Here, we used a dominant frequency of 75 Hz for P-waves, and 26 Hz for S-waves. Figure 4.6a shows the wavelength estimates for P-waves where the values are nearly constant around 35 m. In comparison, Figure 4.6b shows the estimates for S-waves in which values range from 20 m to 50 m.

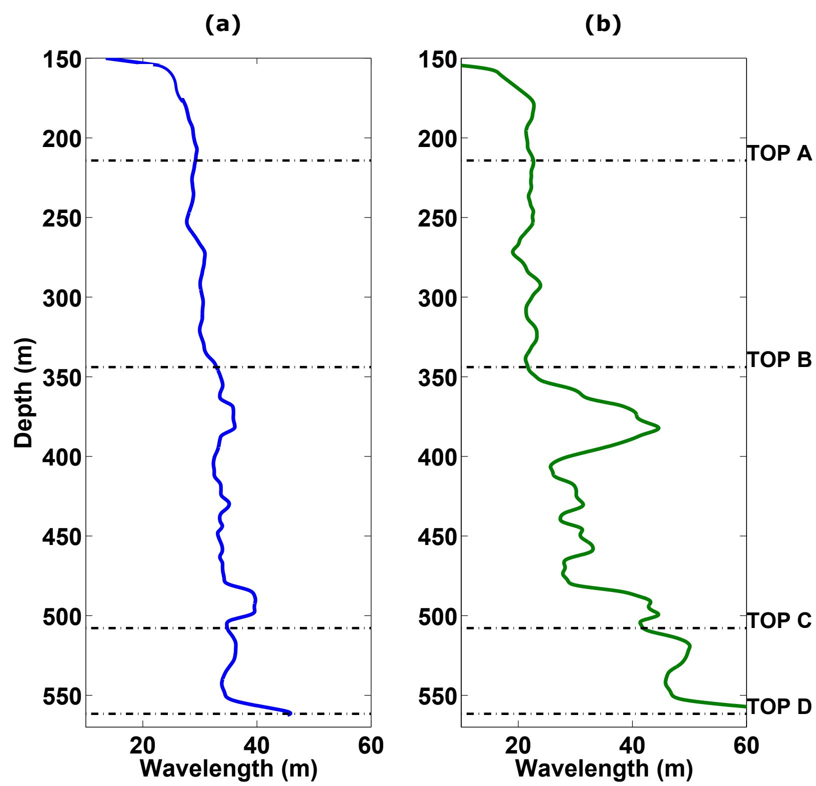

Figure 4.6: Wavelength variation with depth given by the equation $\lambda = V/f_{dom}$. (a) Using P-wave velocity logs and a dominant frequency of 75 Hz. (b) Using S-wave velocity logs and a dominant frequency of 26 Hz. We applied a moving average to the velocity logs to match VSP velocities.

Firstly, we estimated Q_P from the direct downgoing P-wave data acquired from both dynamite and EnviroVibe sources. We used the spectral-matching method for the estimation, with the parameters in Table 4.1. These include receiver distance, which is the vertical separation between receivers, and a frequency bandwidth where we observe the signal. For data recorded with a dynamite source, we used a receiver separation of 120 m and a frequency bandwidth of 22-150 Hz. Note that the receiver separation we used (120 m) is larger than the wavelength (around 35 m) estimated for the P-waves (Figure 4.6a). We selected this value because we needed a large separation distance to estimate Q in order to observe a significant attenuation for the near-surface layers in this shallow borehole. An example of this estimate for two traces is shown in Figure 4.7a. The first step is to compute the amplitude spectrum for each trace (Figure 4.7b). Then we matched the amplitude spectra (Figure 4.7c) in order to calculate Q, resulting in a value of 21 for this specific case (Figure 4.7d) (See description in chapter 2.2.2). Finally, this value is located midway between the two receivers, similar to the Q estimation from synthetic VSP data (Figure 3.2). A similar process was applied to the direct downgoing P-wave data acquired from an EnviroVibe source, as shown in Figure 4.8. Notice that we used a wider frequency bandwidth than in the previous case. These results from use of the broadband sweep, to acquire the data.

Table 4.1: Parameters for the Q_P analysis using the direct downgoing P-wave data acquired with a dynamite and EnviroVibe source.

Source type	Dynamite	EnviroVibe
Receiver separation	120 m	100 m
Frequency bandwidth	22-150 Hz	20-240 Hz

Secondly, we estimated Q_P from the upgoing dynamite P-wave data acquired with the parameters shown in Table 4.2. Figure 4.9 shows an example of the Q estimate for two traces. In this case, the trace 1 is recorded by a receiver deeper than trace 2 because we are using the upgoing wavefield. We did not estimate Q from the data acquired with the EnviroVibe source because significant noise interfered with the upgoing event.

Table 4.2: Parameters for the Q_P analysis using the upgoing P-wave data from a dynamite source.

Source type	Dynamite
Receiver separation	140 m
Frequency bandwidth	8-85 Hz

Finally, we estimate Q_S from the direct downgoing S-wave data acquired from the EnviroVibe source using the parameters of Table 4.3. Here, we used a receiver separation of 100 m and a frequency bandwidth of 9-50 Hz. Note that the receiver separation, of 100 m, is larger than the wavelength estimated for S-waves ranging from 20 m to 50 m (Figure 4.6b). We selected this value because we need the larger separation to observe a significant attenuation for the near-surface layers, as we did previously for P-waves. Figure 4.10 shows the Q_S estimate for two given traces from the direct downgoing S-waves. As one can see, the wavelet varies drastically after travelling a short period of time.

Table 4.3: Parameters for the Q_S analysis using the direct downgoing S-wave data from an EnviroVibe source.

Source type	EnviroVibe
Receiver separation	100 m
Frequency bandwidth	9-50 Hz

Results of the Q estimates for the four cases are shown in Figure 4.11. Error bars were computed from objective function, a direct search in Q values between 5 and 250 is applied here (blue circles in Figure 4.12). As we mentioned previously, Q estimates are obtained by minimizing the objective function (red circle). Then, we added five percentage to this value (green circles) and we find their corresponding Q values. Finally, the error corresponds to the difference between maximum and minimum Q which is 5 for this specific case. In Figure 4.11, as expected, we observe that Q_P estimates from the direct downgoing P-waves vary significantly from 20 to 120 in the near-surface layers (Figure 4.11 a and b). In Figure 4.11b, we observe that Q_P estimates are unstable from 100 to 225 m depth as we observe that the error increased, probably due to noise in the data. In comparison, Q_P estimates from the upgoing P-waves are 50 approximately (Figure 4.11c) and the errors in estimates between 100 and 250 m depths are lower than previous case. Figure 4.11d shows the Q_S estimates from the direct downgoing S-waves. There, we observe a high peak between 400 to 450 m depth that may be related to variations in the lithology. In the next section, we estimate Q_S from the mode-converted upgoing S-wave and compare them with these results.

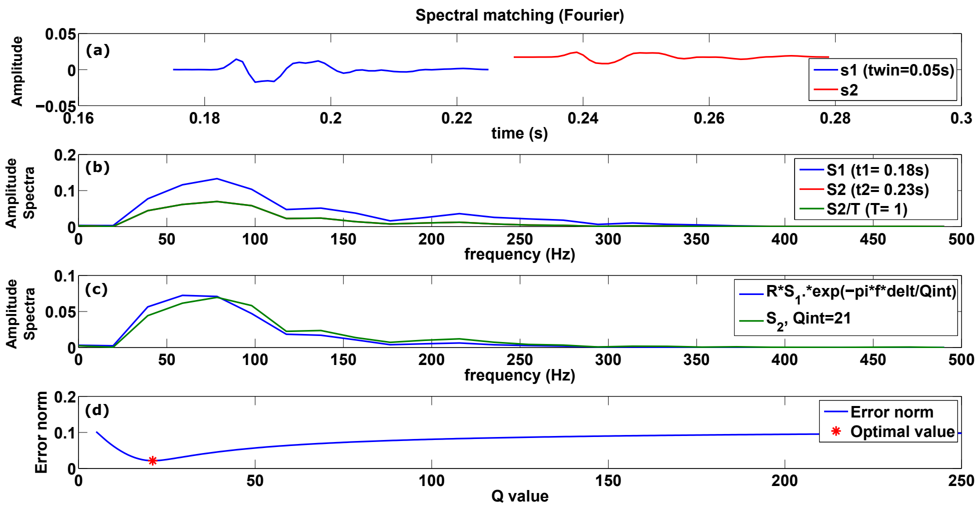

Figure 4.7: Q_P estimation from the direct downgoing P-wave data acquired with dynamite, using spectral matching detailed in Margrave (2013). (a) Wavelets at given times t_1, and t_2, where the receiver separation distance is 120 m and the time window 0.05 s, (b) Amplitude spectra for each wavelet, (c) Amplitude spectra matching, and (d) Minimum of the objective function given by Equation (2.30).

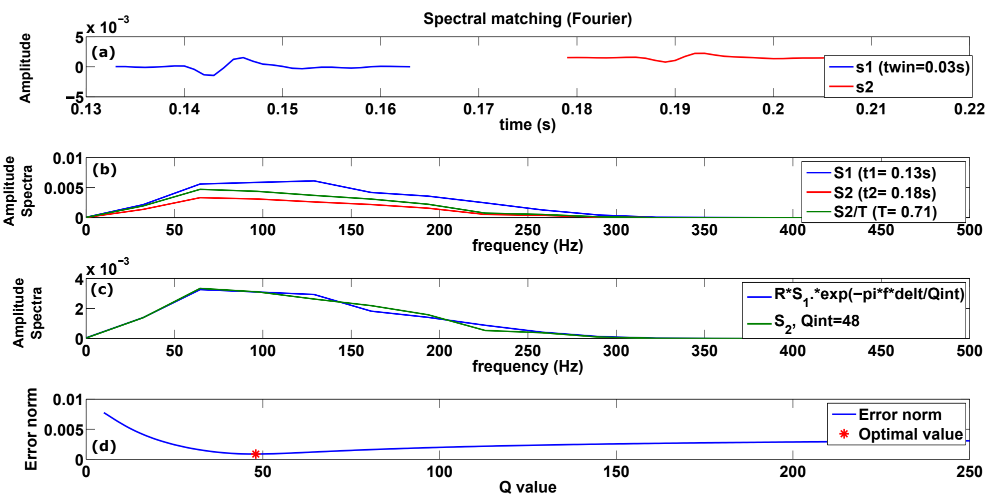

Figure 4.8: Q_P estimation from the direct downgoing P-wave data acquired with EnviroVibe source, using the spectral matching method detailed in Margrave (2013). (a) Wavelets at given times t_1, and t_2, where the receiver separation is 100 m and the time window 0.03 s, (b) Amplitude spectra for each wavelet, (c) Amplitude spectra matching, and (d) Minimum of the objective function given by Equation (2.30).

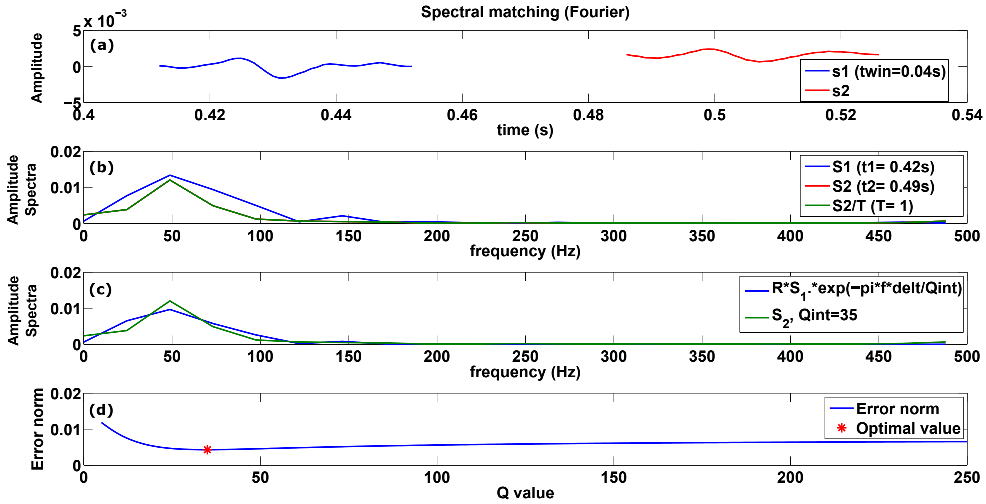

Figure 4.9: Q_P analysis from the direct upgoing P-wave dynamite source data using the spectral matching method detailed in Margrave (2013). (a) Wavelets at given times t_1, and t_2, where the receiver separation is 140 m and the time window 0.04 s, (b) Amplitude spectra for each wavelet, (c) Amplitude spectra matching, and (d) Minimum of the objective function given by Equation (2.30).

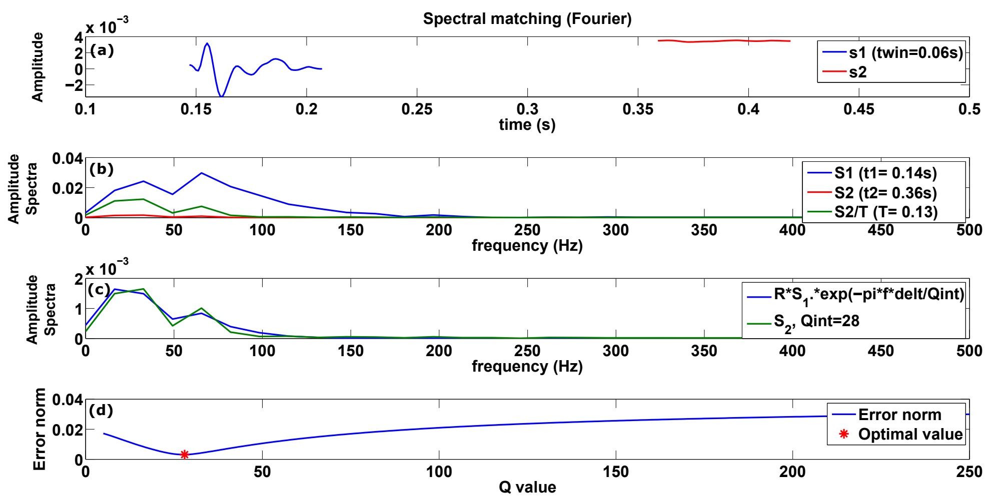

Figure 4.10: Q_S analysis from the direct downgoing S-wave EnviroVibe source data, using the spectral matching method detailed in Margrave (2013). (a) Wavelets at given times t_1, and t_2, where the receiver separation is 100 m and the time window 0.06 s, (b) Amplitude spectra for each wavelet, (c) Amplitude spectra matching, and (d) Minimum of the objective function given by Equation (2.30).

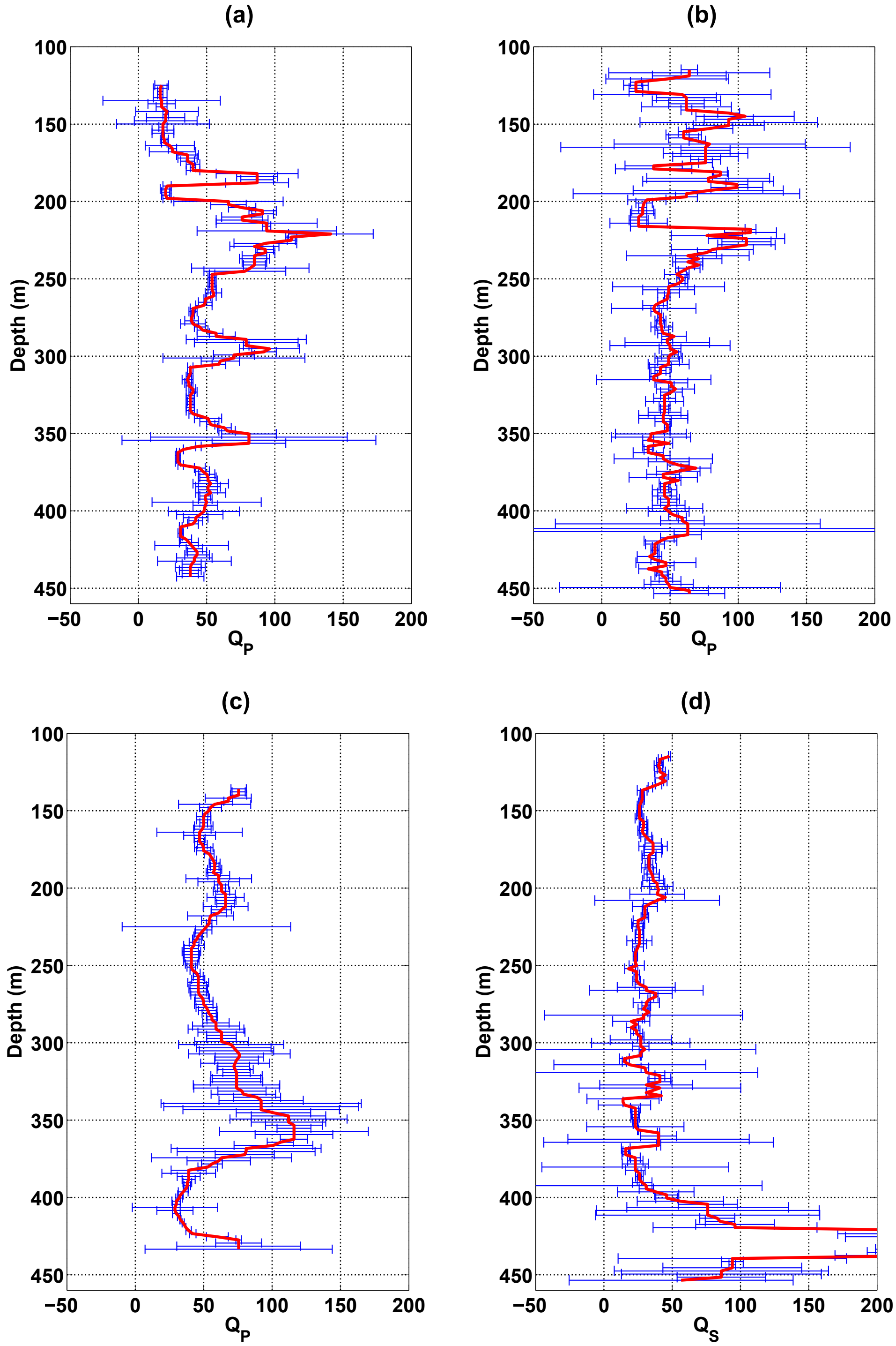

Figure 4.11: (a) Q_P estimations from the direct downgoing P-wave data acquired with dynamite and (b) an EnviroVibe source. (c) Q_P estimations from the upgoing P-wave data acquired with dynamite. (d) Q_S estimations from the direct downgoing S-wave data acquired with an EnviroVibe source.

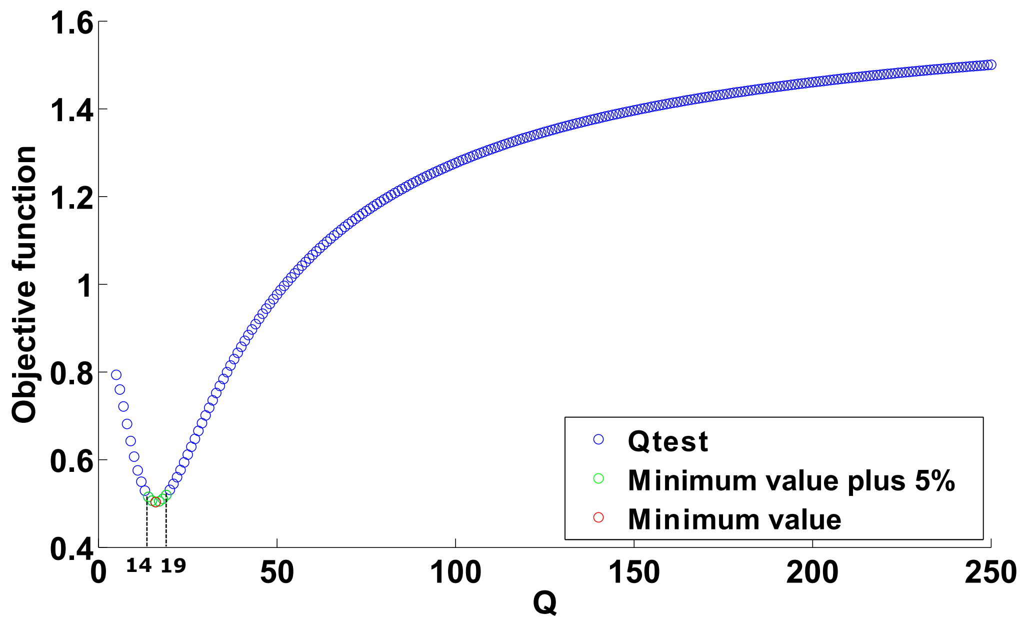

Figure 4.12: Objective function for a given depth. Direct search between Q equals 5 and 250. For this specific case, the error is equal to 5.

4.3 Walkaway VSP data

4.3.1 Data processing and analysis

We processed the walkaway VSP data set to estimate Q_S from the mode-converted upgoing S-waves using the flow shown in Figure 4.13. First, we sorted the data by source point. Then, we selected source points 6 to 9, where the converted wave showed very good energy and less noise. The next steps were very similar to the ones explained previously up to the extraction of the mode-converted upgoing S-waves (see details in chapter 2.1.2). Then, we estimated Q for each source point. Finally, we converted our Q estimates from walkaway VSP to zero-offset conditions by using the Q versus offset method proposed by Dasgupta and Clark (1998). For each depth we computed a linear fit of Q versus offset square values where the intercept corresponds to the Q value at zero-offset.

Figure 4.14a shows gather 9 at a source offset of 600 m. This Figure shows the mode-converted upgoing S-waves returning from the same reflector as the upgoing P-waves identified in Figure 4.2a. Notice that the upgoing S-wave conserves much of its energy and frequency bandwidth over the travel-time distance (Figure 4.14b). This enabled us to obtain reliable Q_S estimates through the strata intersected by the well, using the mode-converted upgoing S-wave data.

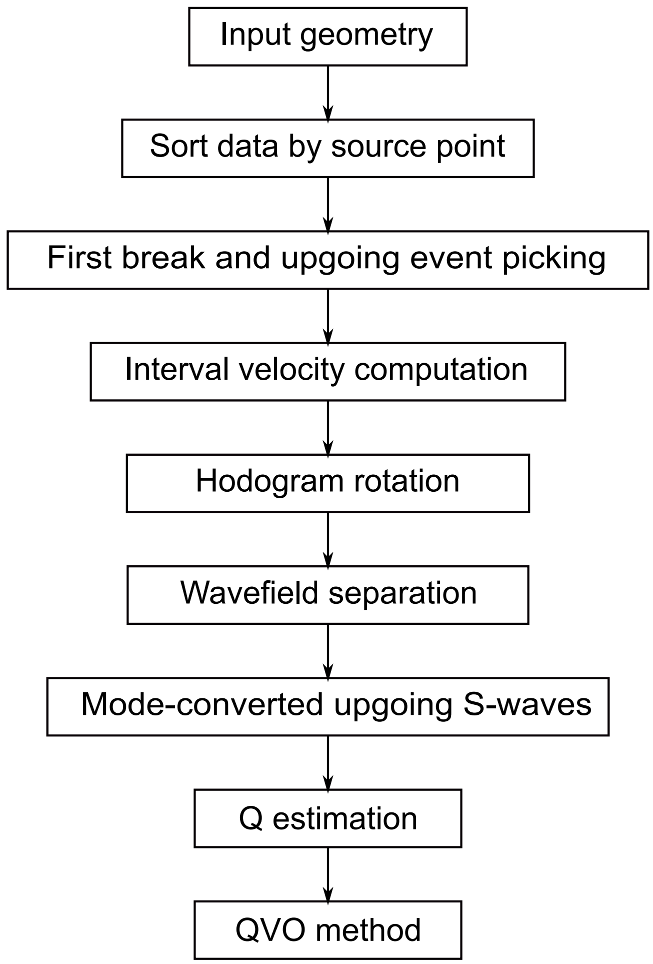

Figure 4.13: Processing flow to estimate Q from a walkaway VSP.

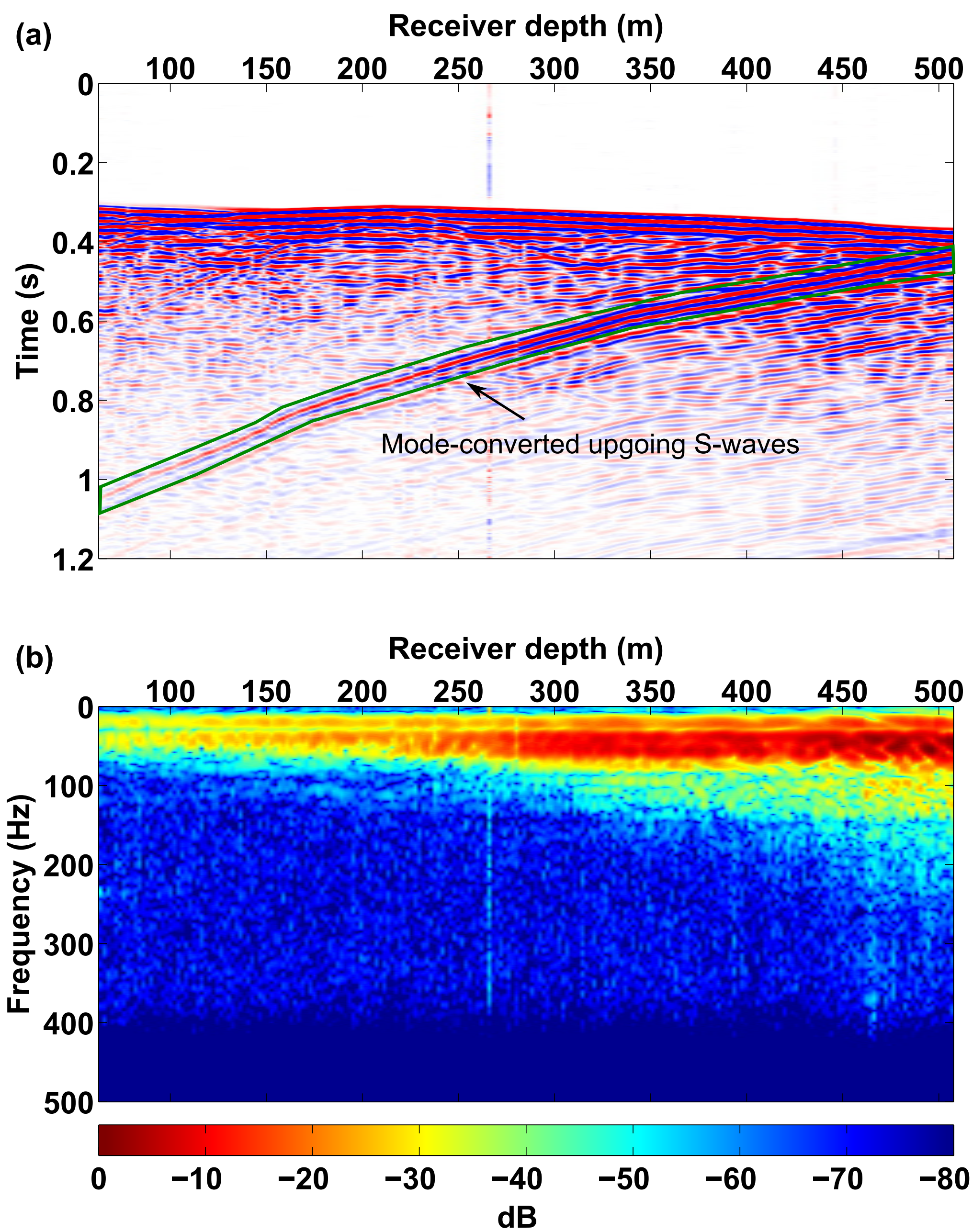

Figure 4.14: (a) Dynamite VSP data from source point 9 at 600 m from the well. (b) Amplitude spectra for the upgoing S-waves using a cosine-tapered window and the delimited data in the green box.

4.3.2 Q analysis and results

We estimated Q_S from the mode converted upgoing S-wave data acquired from dynamite source points 6 to 9. For this estimation, we used the spectral matching method with the parameters shown in Table 4.4. For the four source points, we used a receiver separtion of 100 m. The time window used ranges between 0.1-0.15 s while the frequency bandwidth narrows from 10-70 Hz to 10-40 Hz. Figures 4.15, 4.16, 4.17 and 4.18 show the Q_S estimates for two traces from source points 6 to 9, similar to the Q estimates from the zero-offset VSP data. Results are shown in Figure 4.19. We observed the error is greater for estimates from source point 6 and 9. Figure 4.20 shows these results have a similar trend. Also, there is a peak between 350 to 400 m depth. For the locations where Q_S is higher than 100, we could not estimate Q due to noise in the data, especially for source point 6. After computing Q_S for each source point, we estimated Q_S at zero-offset by using the QVO method shown in Figure 4.21 (see description in chapter 2.2.3). Results are shown in Figure 4.22 where Q_S ranges from 20 to 50.

Table 4.4: Parameters for the Q_S analysis using the mode-converted upgoing S-waves.

Parameters	Shot 6	Shot 7	Shot 8	Shot 9
Offset	300 m	400 m	500 m	600 m
Receiver separation	100 m	100 m	100 m	100 m
Frequency bandwidth	10-70 Hz	10-70 Hz	10-40 Hz	10-40 Hz

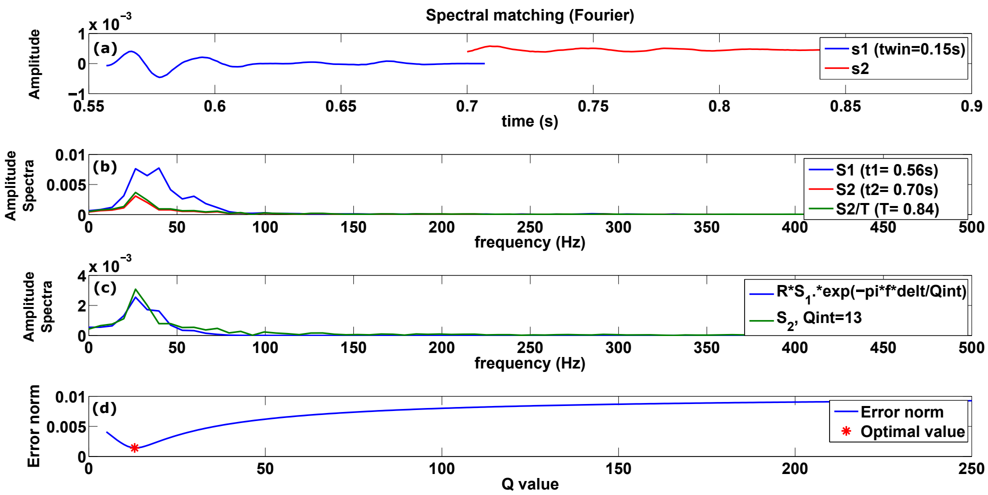

Figure 4.15: Q_S analysis from the mode-converted upgoing S-wave data acquired with dynamite at source point 6, using the spectral matching method detailed in Margrave (2013). (a) Wavelets at given times, t_1 and t_2, where the receiver separation is 100 m and the time window is 0.15 s, (b) Amplitude spectra for each wavelet, (c) Amplitude spectra matching, and (d) Minimum of the objective function given by Equation (2.30).

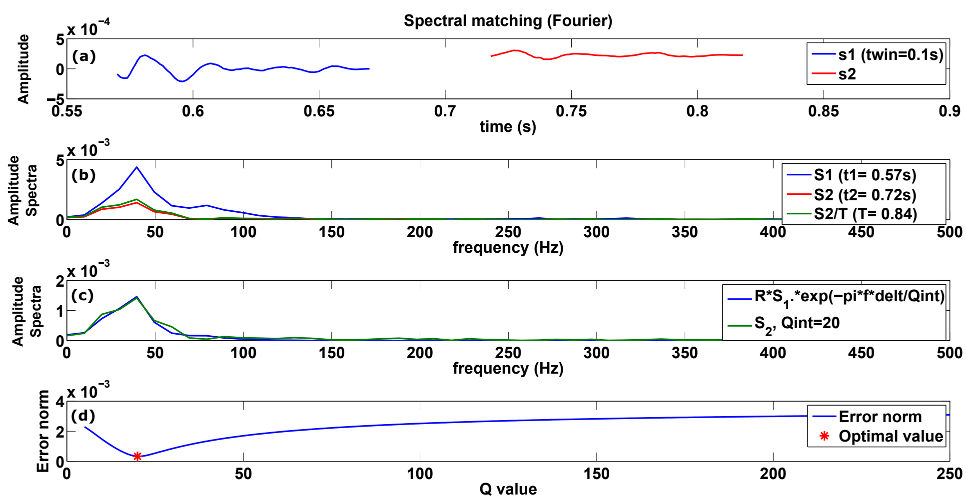

Figure 4.16: Q_S analysis from the mode-converted upgoing S-wave data, acquired with dynamite at source point 7, using the spectral matching method detailed in Margrave (2013). (a) Wavelets at given times t_1, and t_2, where the receiver separation is 100 m and the time window 0.1 s, (b) Amplitude spectra for each wavelet, (c) Amplitude spectra matching, and (d) Minimum of the objective function given by Equation (2.30).

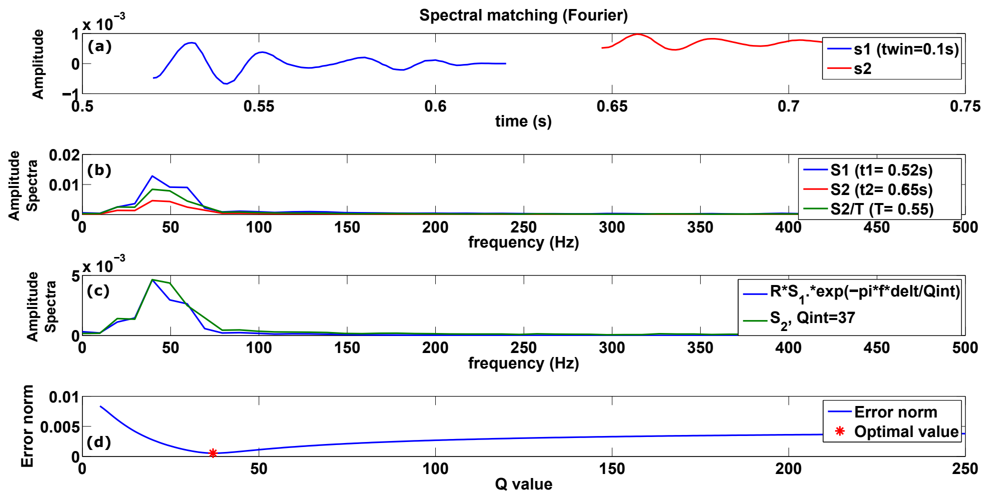

Figure 4.17: Q_S analysis from the mode-converted upgoing S-wave data, acquired with dynamite at source point 8, using the spectral matching method detailed in Margrave (2013). (a) Wavelets at given times t_1, and t_2, where the receiver separation distance is 100 m and the time window is 0.1 s, (b) Amplitude spectra for each wavelet, (c) Amplitude spectra matching, and (d) Minimum of the objective function given by Equation (2.30).

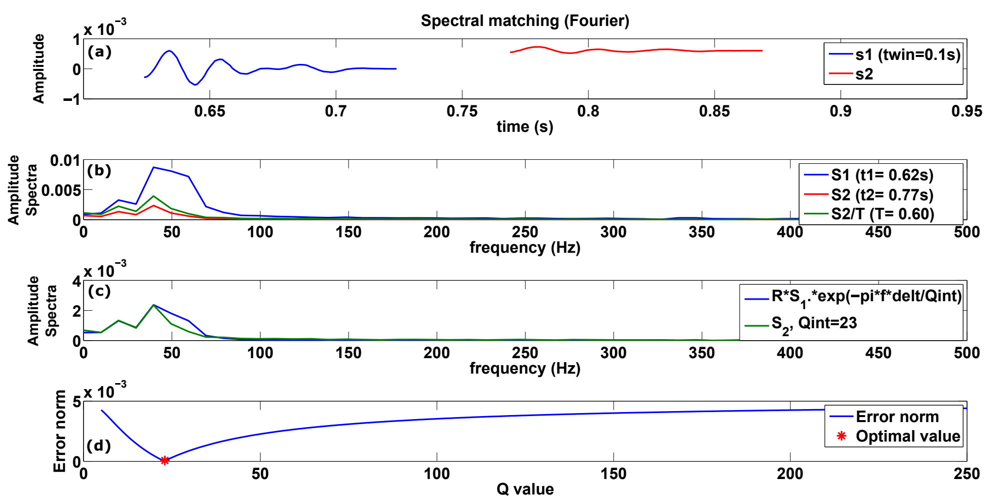

Figure 4.18: Q_S analysis from the mode-converted upgoing S-wave data acquired with dynamite at source point 9, using the spectral matching method detailed in Margrave (2013). (a) Wavelets at given times, t_1 and t_2, where the receiver separation is 100 m and the time window is 0.1 s, (b) Amplitude spectra for each wavelet, (c) Amplitude spectra matching, and (d) Minimum of the objective function given by Equation (2.30).

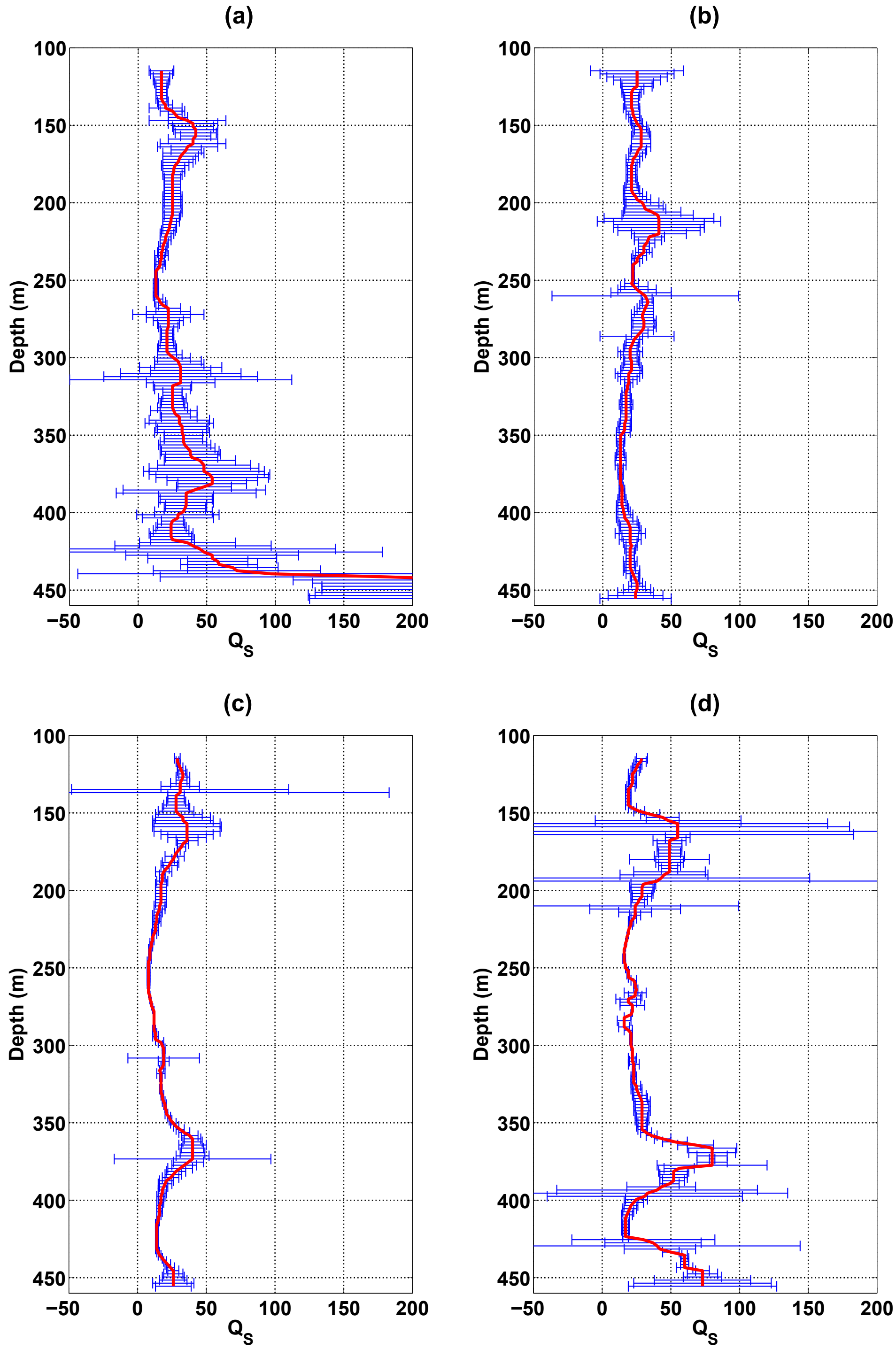

Figure 4.19: Q_S estimates from the mode-converted upgoing S-waves for the source points (a) 6, (b) 7, (c) 8 and (d) 9.

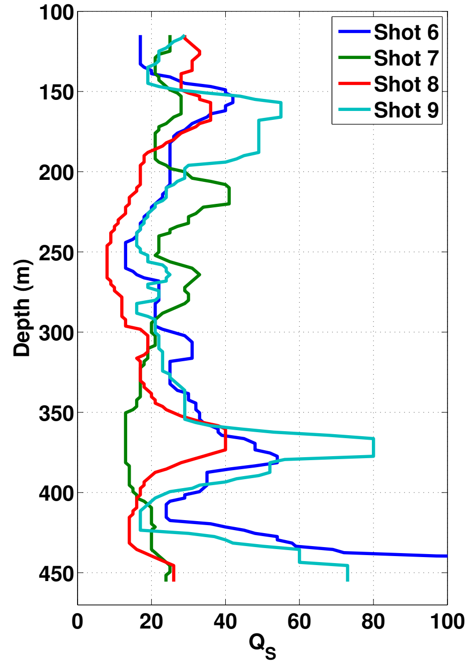

Figure 4.20: Q_S estimates from the mode-converted upgoing S-waves for the source points 6 to 9.

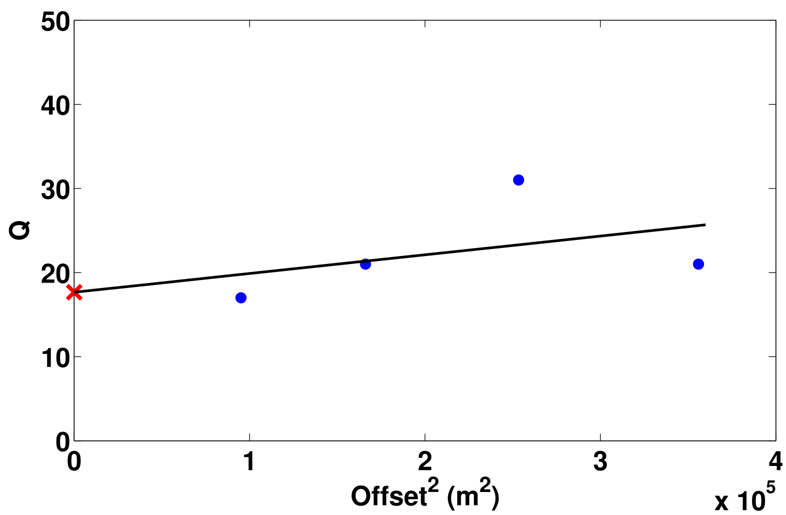

Figure 4.21: Q versus offset squared for a receiver depth = 132 m.

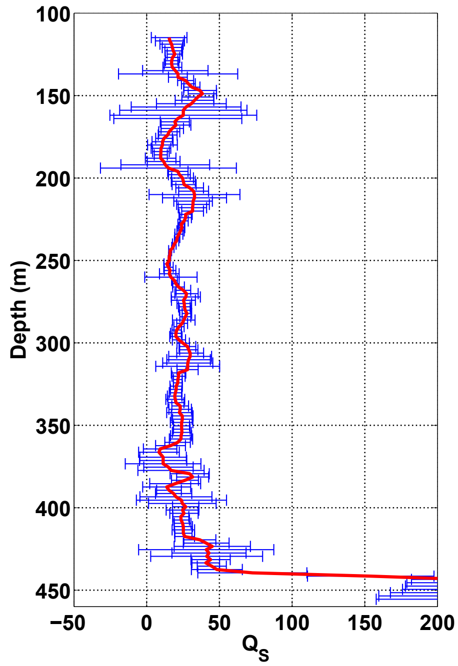

Figure 4.22: Q_S estimates using the QVO method.

4.4 Discussion

Figure 4.23 shows Q estimates from P-wave, S-wave and mode-converted wave analysis. In Figure 4.23a, we observe the Q_P estimates from the zero-offset VSP data. The blue line indicates the Q_P estimates from the downgoing P-wave dynamite source data and red line from an EnviroVibe source. The green line corresponds to the Q_P estimates from the upgoing P-wave dynamite source data. From 100 to 200 m depth, we observe that Q_P estimates from the downgoing P-waves vary significantly from 20 to 100 as predicted (blue and red line). In comparison, Q_P estimates from the upgoing P-waves are approximately 50 (green line). We consider this low Q_P value to be more reliable because poorly consolidated rocks are usually present in the near-surface. For the three cases, we observe a peak around the Top formation A. Also, there is a peak around the Top formation B (blue and green line). This suggests that, in this case, Q_P estimates are related to variations in the lithology. A better understanding of Q_P variations with depth is obtained by combining the three results.

In Figure 4.23b, we observe the Q_S estimates from the zero-offset and walkaway VSP data. The red line indicates the Q_S estimates from the direct downgoing S-wave EnviroVibe source data for the zero-offset VSP. The green line corresponds to the Q_S estimates from the mode-converted upgoing S-wave dynamite source data. As can be seen in Figure 4.23b, the two estimates have a similar trend. Below 400 m the Q_S estimated from the downgoing wavefield (red line) is over 50. This may not be reliable because most of the energy and bandwidth have been lost at these depths. Estimates from the mode-converted upgoing S-wave (green line) are probably more accurate at such depths. We also observe that Q_S is significantly lower than Q_P, as the data show that S-waves attenuate faster than P-waves.

Lastly, we calculated Q_S/Q_P using the data recorded with the same source (Figure 4.23c). First, we computed the ratio using the Q_P estimated from downgoing P-wave dynamite source data (Figure 4.23a, blue line) and the Q_S estimated from the mode-converted upgoing S-wave dynamite source data (Figure 4.23b, green line). This corresponds to the Q_S/Q_P values shown in Figure 4.23c (blue line). Then, we also computed the ratio using the Q_P estimated from downgoing P-wave EnviroVibe source data (Figure 4.23a, red line) and the Q_S estimated from the downgoing S-wave EnviroVibe source data (Figure 4.23b, red line). Results are shown in Figure 4.23c (red line). In this figure, we observe that both estimates share a similar trend when values range from 0 to 7. There is an increase of Q_S/Q_P values around the Top formation A, and between 400 m and 450 m. These changes could be related to variations in lithology or fluid saturation, especially for the deepest anomaly closer to the reservoir formation.

According to Mavko and Nur (1979), and Winkler and Nur (1982), P-wave attenuation in partially saturated rocks is stronger than S-wave attenuation. However, in fully saturated rocks S-wave attenuation is stronger than P-wave attenuation (Figure 2.15). The value Q_S/Q_P equal to 1 can be used as a reference to separate partial saturation ($Q_S/Q_P > 1$) from total saturation ($Q_S/Q_P < 1$). Figure 4.24 shows Q_S/Q_P obtained from dynamite data versus V_P/V_S from well logs. We applied a moving average filter to the velocity logs to match the resolution of the Q estimates. For this study, water saturation logs were not available. For this reason, we coloured the scatterplots by gamma-ray and depth (Figure 4.26). This gave us a general idea of fluid saturation strata intercepted by the borehole. Following the analysis of Mavko and Nur (1979), and Winkler and Nur (1982), we interpret the blue circle in Figure 4.24, to represent partially saturated rocks and the red circle fully saturated rocks. Notice that points enclosed by the red circle show high gamma-ray values. This may indicate shaly sediments, in which high water saturation is usually found. Also, we observe, in the scatter-plot coloured by depth, that the blue box encloses points located over 400 m depth and close to the transition zone. This suggests that partially saturated rocks are present in the area. Similar observations can be drawn from the scatterplots from the EnviroVibe source data (Figure 4.25). There, we observe a clear separation between partially and fully saturated rocks.

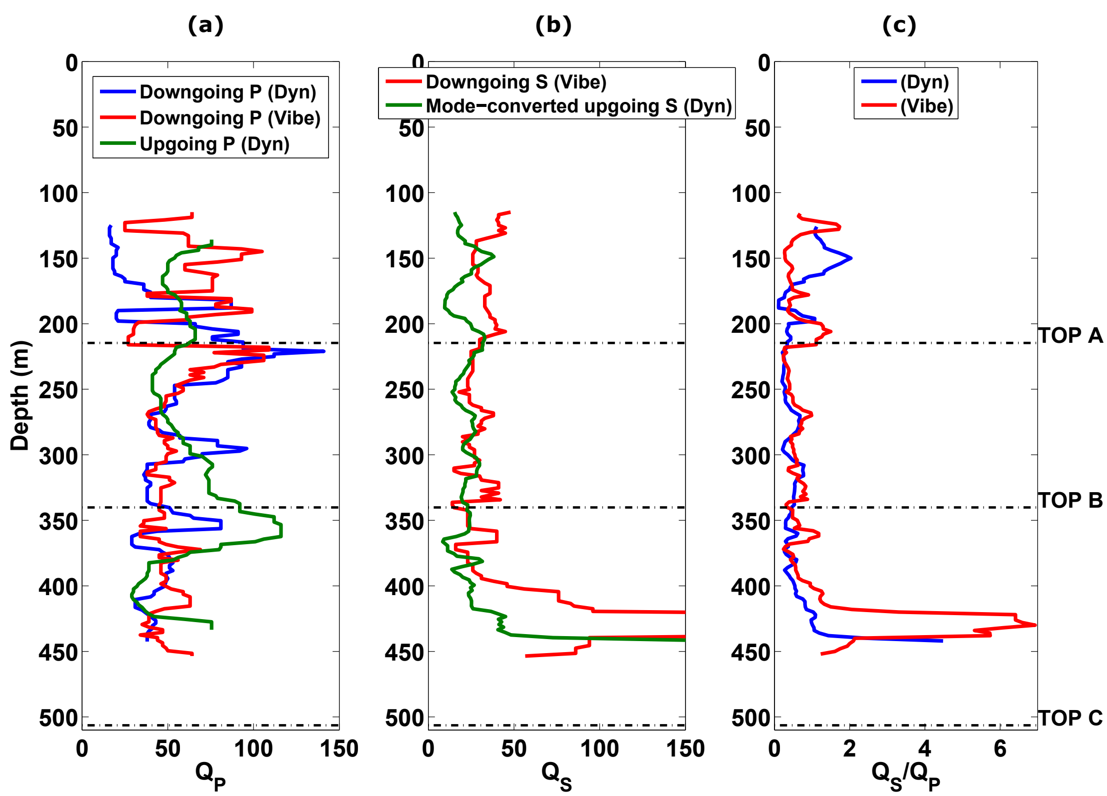

Figure 4.23: Q estimates using spectral matching method (Case study 1).

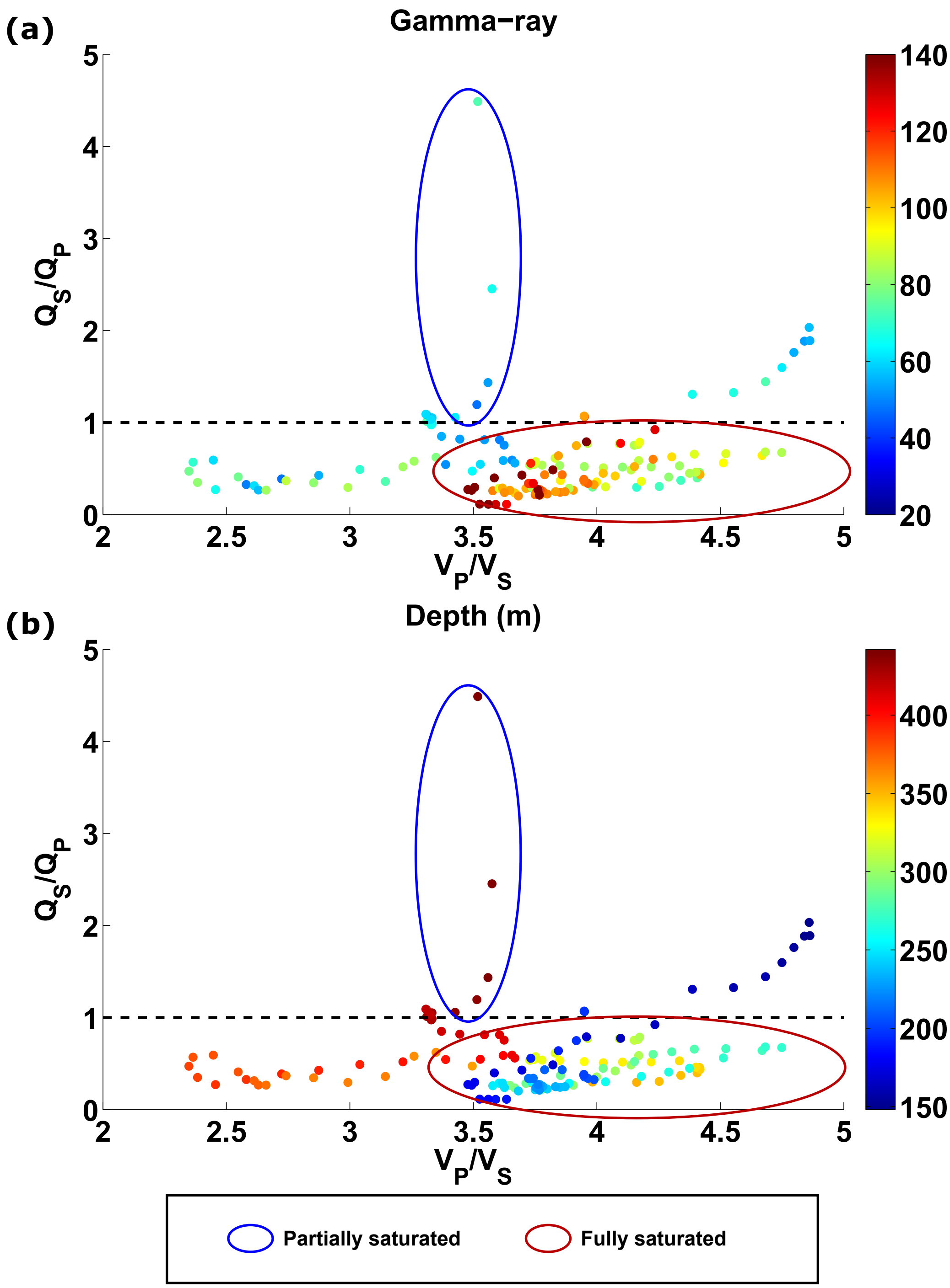

Figure 4.24: Seismic attenuation versus velocity ratio. Q_S/Q_P obtained from the dynamite source data(blue line, Figure 4.18c). Scatterplot coloured (a) by gamma-ray and (b) by receiver depth.

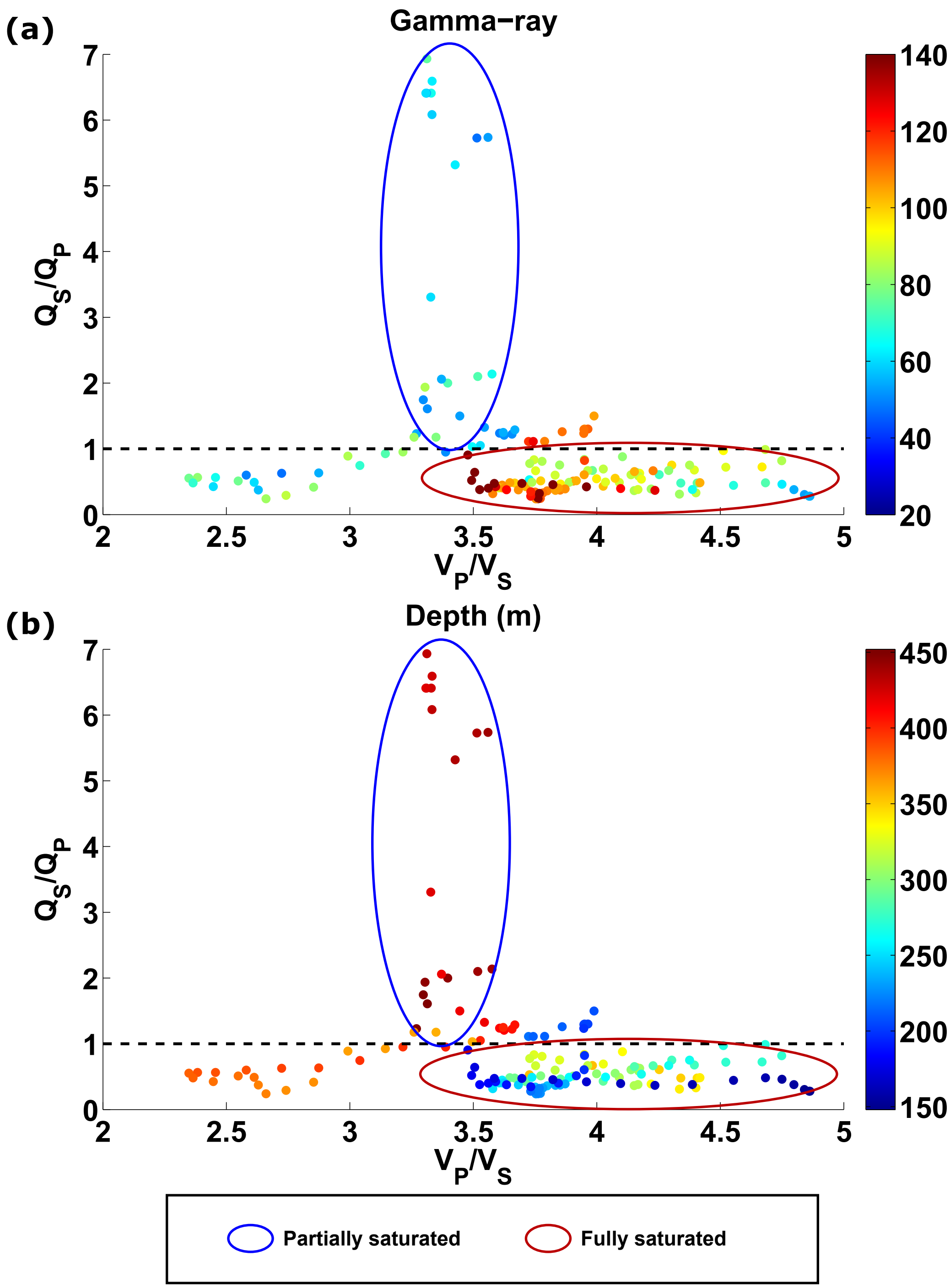

Figure 4.25: Seismic attenuation versus velocity ratio. Q_S/Q_P obtained from the EnviroVibe source data (blue line, Figure 4.18c). Scatterplot coloured (a) by gamma-ray and (b) by receiver depth.

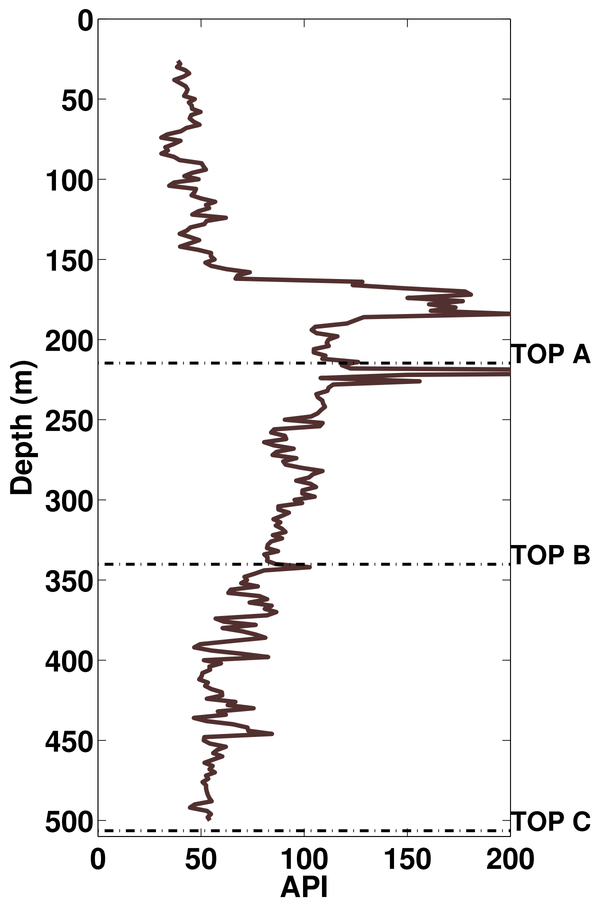

Figure 4.26: Gamma-ray for case study 1.

Chapter 5

CASE STUDY 2

5.1 Introduction

For this part of the thesis we studied a 3D VSP recorded in a field in Western Canada. As we mentioned in Chapter 1.3, 1047 source points were acquired using a Mertz 18 vibrator source producing a linear sweep of 6-120 Hz over 12 s (Figure 1.5). The acquisition parameters for this study are shown in Table 1.2. Q_P and Q_S were estimated from the source gather 1; offset 72 m from the borehole. For additional work we analyzed some gathers offset 300 m from the borehole.

5.2 Zero-offset VSP

5.2.1 Data processing and analysis

We continue to use the same processing flow as in Chapter 4.2.1 (Figure 4.1) to estimate Q from the zero-offset VSP data. The processing flow included: input geometry, first break picking, interval velocity computation, hodogram rotation, wavefield separation and Q estimation. Further details of the processing are shown in Chapter 4.2.1.

Figure 5.1a shows the vertical component of the VSP vibrator data for source point 1. This is the nearest source point, offset 72 m from the well. We identified high-amplitude downgoing P-waves as first arrivals. We are interested in this event for measuring P-wave attenuation. We also observe three upgoing P-waves, the indicated by the blue arrow is from a high-amplitude reflector near 750 m depth (Figure 5.1a). The upgoing P-wave events may be used to estimate Q_P in the near-surface and to corroborate our estimates for the previous case. Preliminary analysis was done by computing amplitude spectra of the direct downgoing P-waves, using the delimited data in the green box in Figure 5.1a. The spectra of Figure 5.1b, show the frequency bandwidth to decrease with depth, a clear signature of seismic attenuation.

In comparison, Figure 5.2a shows the horizontal component (Hmax) for the 72 m offset vibrator source. Here, we observe direct downgoing S-waves. The amplitude spectra of these traces (Figure 5.2b), suggest greater attenuation for this wave-mode than was observed in the previous case study. Notice that the S-wave data has a narrow frequency bandwidth compared to the P-wave data (Figure 5.1b), with significant losses in bandwidth even before arriving at the shallowest receiver depth (10 m).

Also, the S-wave has lost even more energy and bandwidth below 1000 m depth. This makes it difficult to estimate Q_S at the deepest receivers in the well. Below 1500 m, are additional events that we consider to be tube waves. A tube wave propagates along the interface between the fluid in the wellbore and the wall of the wellbore (Schlumberger, 1998). In this case, we observe that the tube wave enclosed in the green box has a different frequency window compared to direct downgoing S-waves. Also, tube wave velocities are similar to water velocity ($\approx 1500 m/s$). We can follow the event back to its point of origin at $\simeq$ 1500 m, to identify the source of the tube wave (Hardage, 1981). There is a variation in borehole diameter at this depth (See Figure B.1 in Appendix B). We know that geophones respond to tube waves in cased, partially cemented wells (Hardage, 1981), suggesting that this well was partially cemented below 1500 m depth.

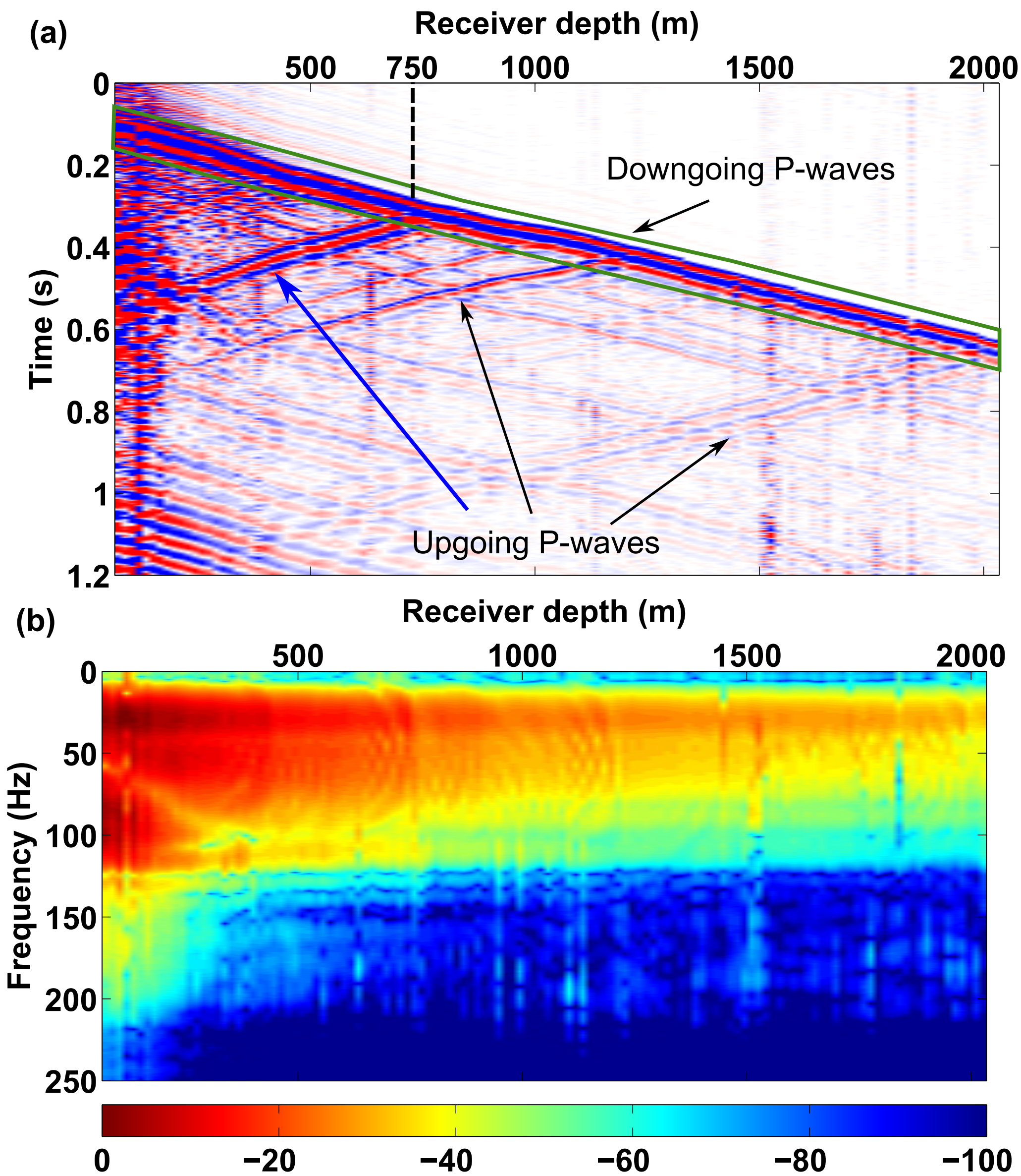

Figure 5.1: (a) Source gather 1 from a Mertz 18 vibrator source (vertical component). (b) Amplitude spectra for the downgoing P-waves enclosed in the green box. Blue arrow indicates the high amplitude upgoing P-waves.

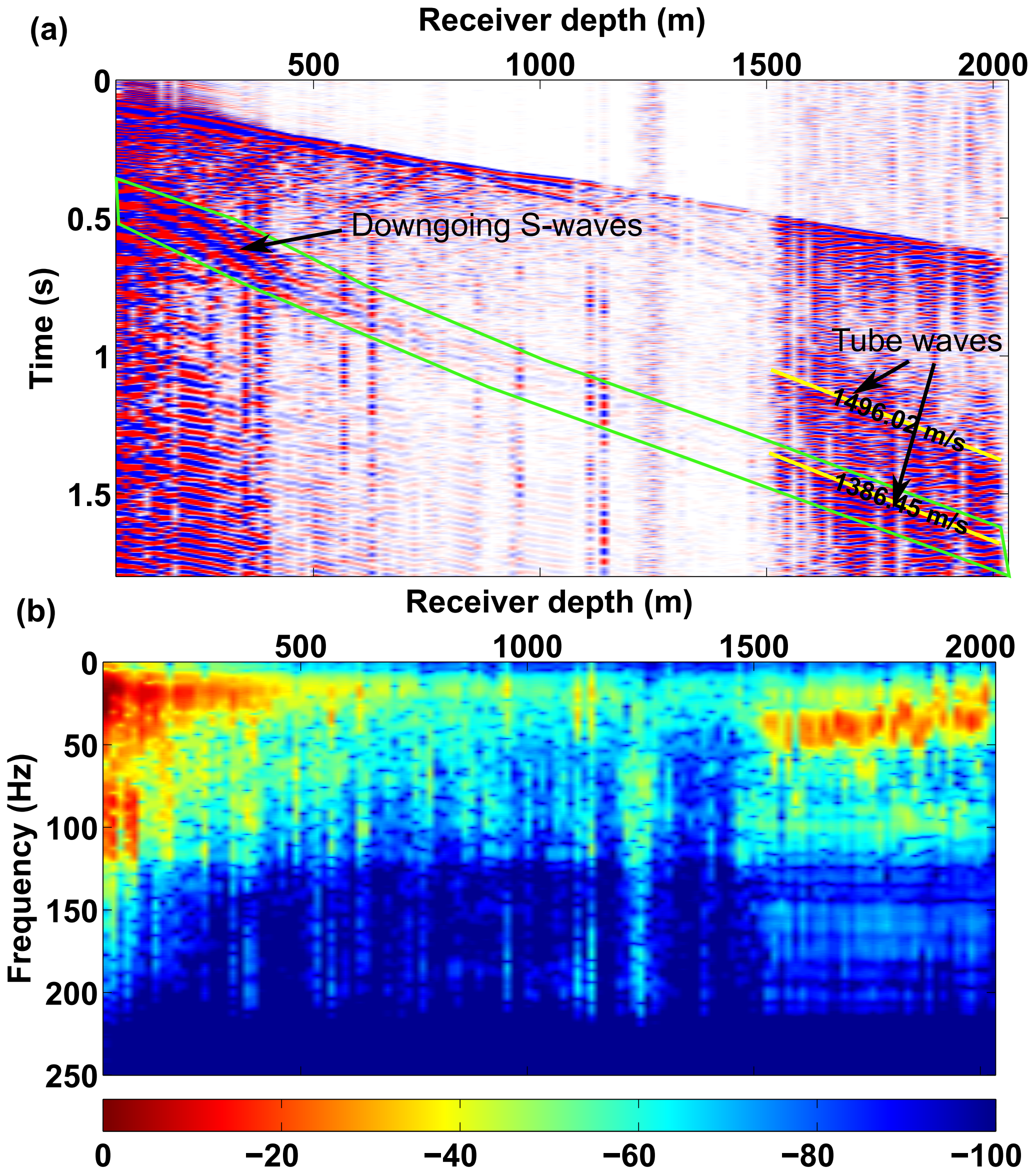

Figure 5.2: (a) Hmax from source gather 1 acquired with a Mertz 18 vibrator source. (b) Amplitude spectra of signals enclosed in the green box.

5.2.2 Q analysis and results

Figure 5.3 shows well log data that, after applying a moving average to match seismic resolution. This has a length of 15.24 m, in which a cosine weight was used to average density, P-wave and S-wave velocities. In this part of the thesis, we used these velocities to compute wavelength, λ (Figure 5.4). This is given by the equation $\lambda = V/f_{dom}$, where the velocity, V, is obtained from well logs. For the dominant frequency, f_{dom}, we used a constant value obtained from the first arrivals recorded by the VSP data. Figure 5.4a shows the wavelength estimates for P-waves ranging from $\simeq$60 m to $\simeq$187.5 m. In comparison, Figure 5.4b shows the wavelength estimates for S-waves where the values range from 30 m to 170 m.

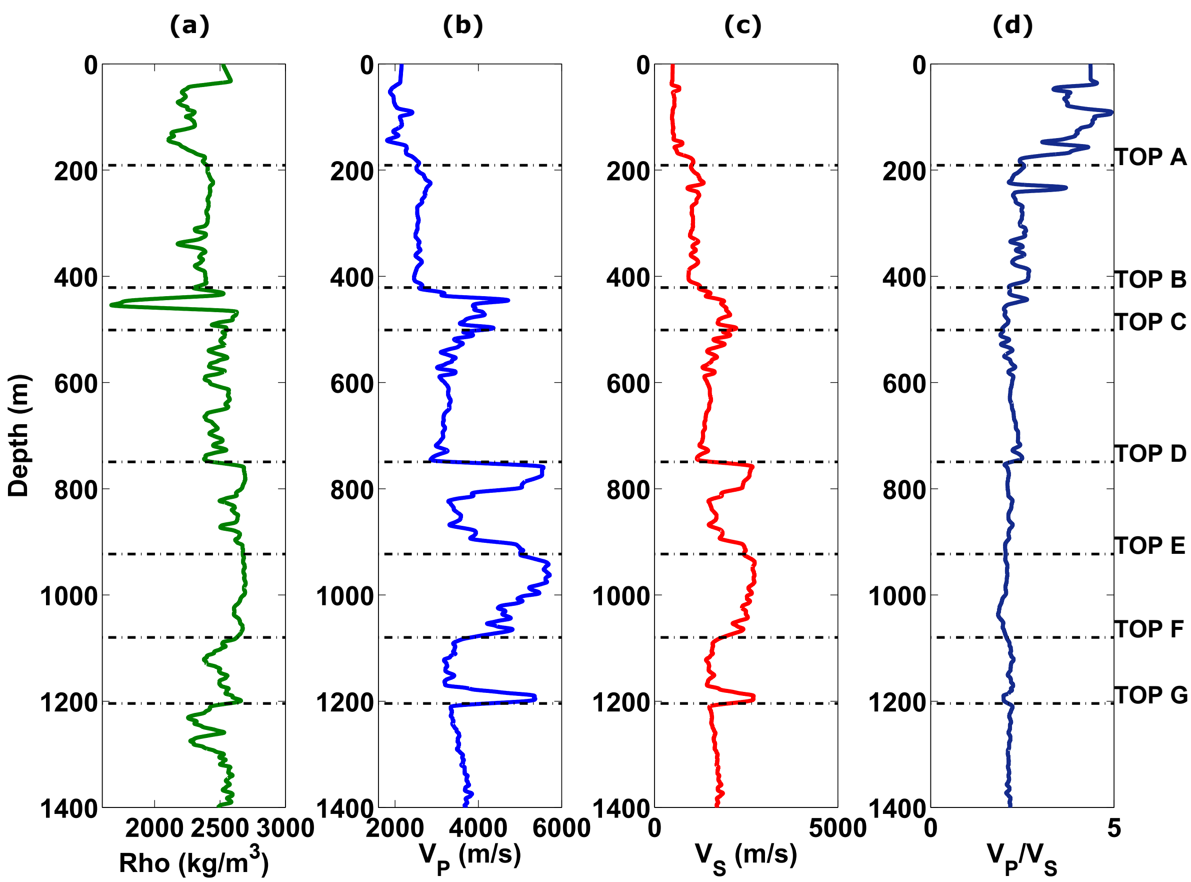

Figure 5.3: Well logs for Case Study 2. (a) Density, (b) P-wave velocity, (c) S-wave velocity, and (d) V_P/V_S.

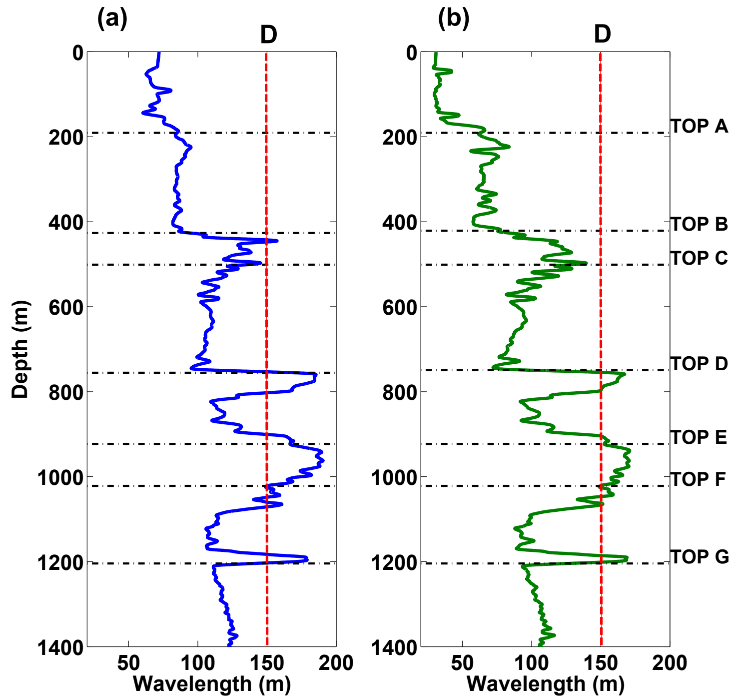

Figure 5.4: Wavelength variation with depth given by the equation $\lambda = V/f_{dom}$. (a) Using P-wave velocity logs and a dominant frequency of 30 Hz. (b) Using S-wave velocity logs and a dominant frequency of 16 Hz. We applied a moving average to the velocity logs to match VSP velocities. D is the receiver separation used for Q estimates.

First, we estimated Q_P from the direct downgoing P-waves. We used the spectral-matching method with the parameters shown in Table 5.1 for the estimate. Note that these are different from the previous case. Here, we used a receiver separation of 150 m, and a bandwidth of 10-120 Hz. We compared D, the receiver separation we chose, to wavelength estimates at different depths (Figure 5.3a). Note that we chose a separation, D, in between the minimum and maximum wavelength since we are using a constant value. Additional work could be done using a receiver separation that varies with depth, especially for deep boreholes as in case study 2. Figure 5.5a shows the Q_P estimate for two traces from the direct downgoing P-waves. As we explained in Chapter 2.2.2, the first step is to compute the amplitude spectrum for each trace (Figure 5.5b). Then we match the amplitude spectra (Figure 5.4c) to calculate Q, which results in a value of 21 for this specific case (Figure 5.5c). Finally, this value is assigned to a location midway between the two receivers, similar to the Q estimate from the synthetic VSP data (Figure 3.2).

Table 5.1: Parameters for the Q_P analysis using the direct downgoing P-waves.

Source type	Mertz 18
Receiver separation	150 m
Frequency bandwidth	10-120 Hz

Finally, we estimated Q_S from the direct downgoing S-wave data using the parameters shown in Table 5.2. Here, we used a receiver separation of 150 m and a frequency bandwidth of 10-50 Hz. We compared the receiver separation, D, with the wavelength variation with depth obtained for S-waves (Figure 5.4b). We used the same separation distance as we did for the P-waves in order to compute consistent Q_S/Q_P values. Figure 5.6 shows the Q analysis for two wavelets from the direct downgoing S-waves. We observed that the wavelet shape varies drastically after travelling a short period of time.

Table 5.2: Parameters for the Q_S analysis using the direct downgoing S-waves.

Source type	Mertz 18
Receiver separation	150 m
Frequency bandwidth	10-50 Hz

Results of the Q estimates for the two cases are shown in Figure 5.7. Note that Q_P estimates from the direct downgoing P-waves vary significantly from 20 to 100 in the near-surface layers as expected (Figure 5.7a). Also, we observed a peak at $\sim$500 m. Then, between 800 and 1800 m, Q_P estimates gradually increase from 20 to 100 m. On the other hand, Figure 5.7b shows the Q_S estimates from the direct downgoing S-waves shows a large peak at $\simeq$600 m depth that may be related to uncertainties in the estimates. At 1300 m depth, large values occur that may not be reliable due to noise in the data. We did not estimate Q_S bellow 1400 m, due to the poor S/N ratio in the data.

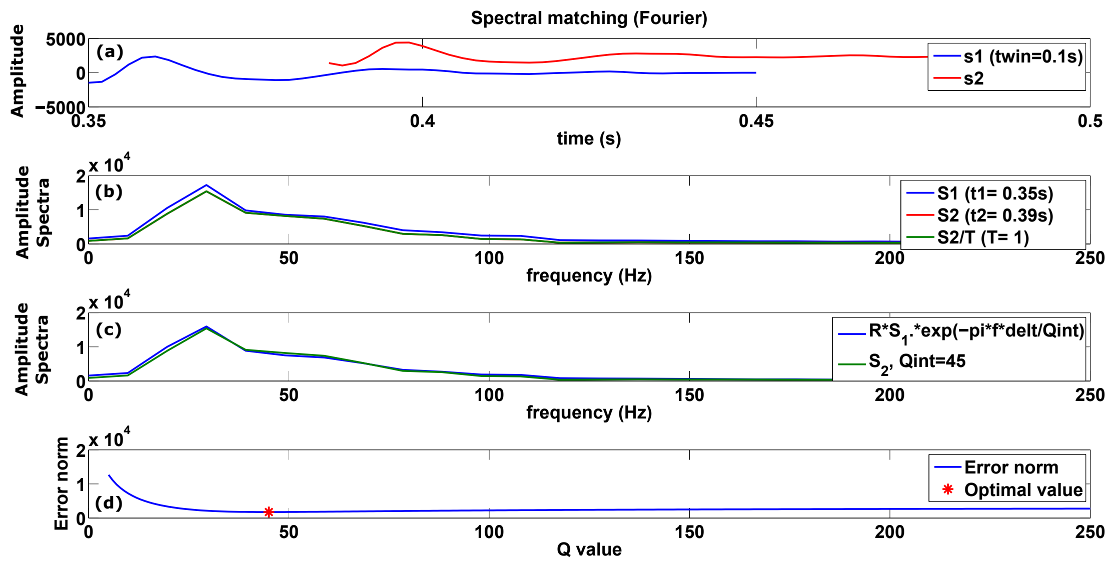

Figure 5.5: Q_P analysis of the direct downgoing P-wave data acquired with the Mertz 18 vibrator, using the spectral matching method adapted from Margrave (2013). (a) Wavelet at times t_1 and t_2, where the receiver separation distance is 150 m, and the time window 0.1 s, (b) Amplitude spectrum for each wavelet, (c) Amplitude spectra matching, and (d) Minimum of the objective function (Equation (2.30)).

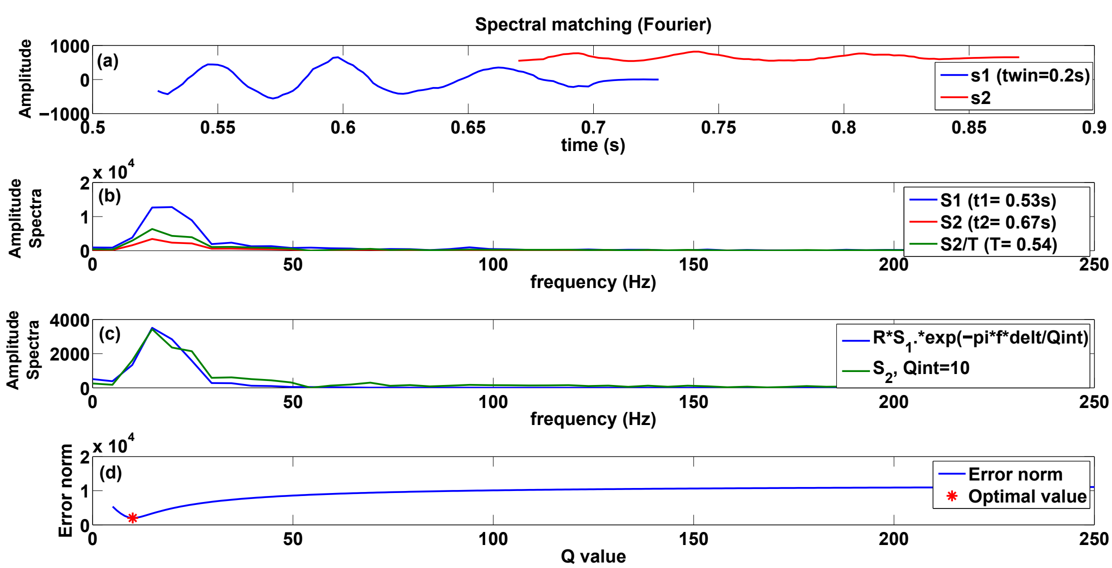

Figure 5.6: Q_S analysis of the direct downgoing S-wave data acquired with the Mertz 18 vibrator, using the spectral matching method adapted from Margrave (2013). (a) Wavelets at times t_1 and t_2 where the receiver separation is 150 m, and the time window of 0.2 s, (b) Amplitude spectrum for each wavelet, (c) Amplitude spectra matching, and, (d) Minimum of the objective function (Equation (2.30)).

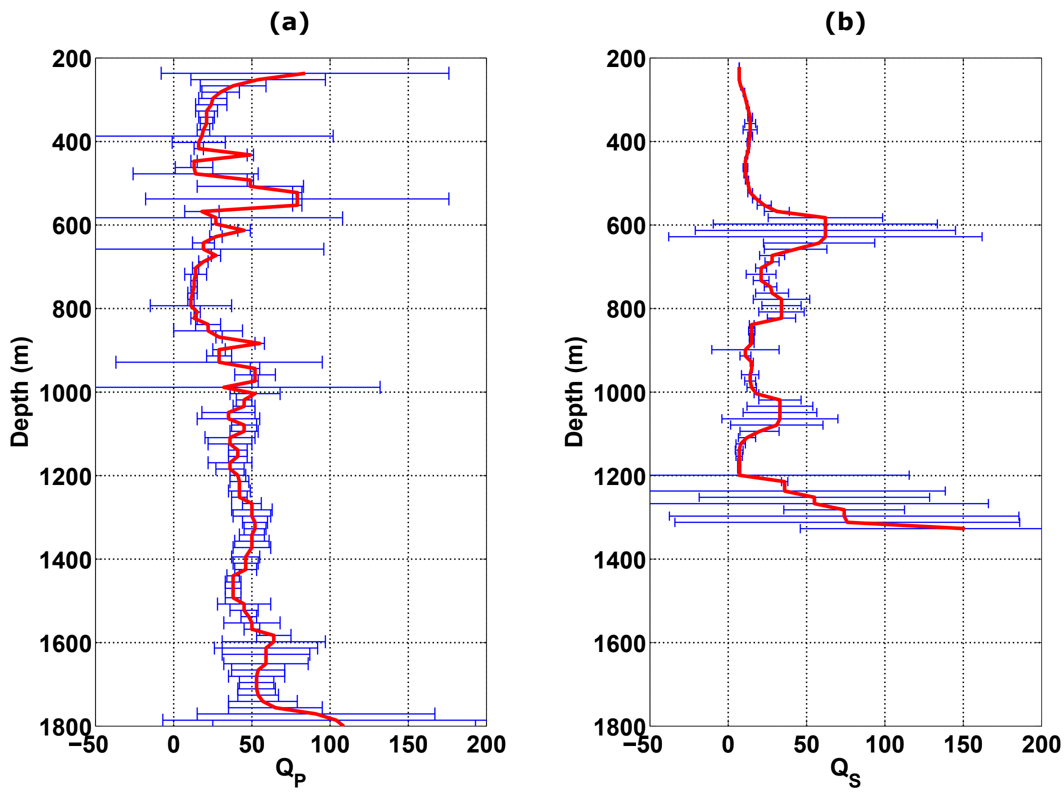

Figure 5.7: (a) Q_P estimates from the direct downgoing P-waves. (b) Q_S estimates from the direct downgoing S-waves. The data was acquired with a Mertz 18 vibrator source.

5.3 Discussion

Figure 5.8 shows an overview of the Q estimates including Top Formations. We plotted all depth values only to 1400 m, because we were not able to estimate Q_S below this level due to noise in the data (tube waves). Figure 5.7a, shows Q_P estimates from the direct downgoing P-waves. In this plot, we observed two peaks, close to Top Formations B and C that may be related to variations in lithology. Then, between 580 m and 750 m the estimates decrease from 40 to 20. Below 750 m depth (Top Formation D), Q_P estimates gradually increase from 20 to 50.

In comparison, Figure 5.8b shows Q_S estimates from the direct downgoing S-waves. Overall, we observed that the values are lower than Q_P estimates but with some exceptions. At $\simeq$600 m, we observed a peak that may not be related to variation in lithology. Between

750 m depth (Top Formation D) and 1200 m (Top Formation G), Q_S estimates decrease from 40 to 10. At the bottom, between 1200 m and 1400 m, we observed a drastic increase in the Q_S estimate, from 10 to 75. Lastly, we calculated Q_S/Q_P values using previous estimates (Figure 5.8c). In this figure, we observed a high Q_S/Q_P ratio between 500 m (Top Formation C), and 920 m (Top Formation E), because Q_S is greater than Q_P at these depths. This may be related to variations in fluid saturation.

Using the velocities from well logs and previous Q estimates, we computed a crossplot, Q_S/Q_P versus V_P/V_S (Figure 5.9). As in Case Study 1, we coloured the scatterplots by gamma-ray and depth (Figure 5.10). This helped attain a general idea of fluid saturation in the strata intercepted by the borehole. Following the analysis of Mavko and Nur (1979), and Winkler and Nur (1982), in Figure 5.9 we interpreted the blue circle as partially saturated rocks, and the red circle as fully saturated rocks. Notice that points enclosed by the red circle show high gamma-ray values. This may indicate shaly sediments, in which high water saturation is usually found. Also, we could observe in the scatter-plot coloured by depth that the blue box encloses depths between 400 and 800 m.

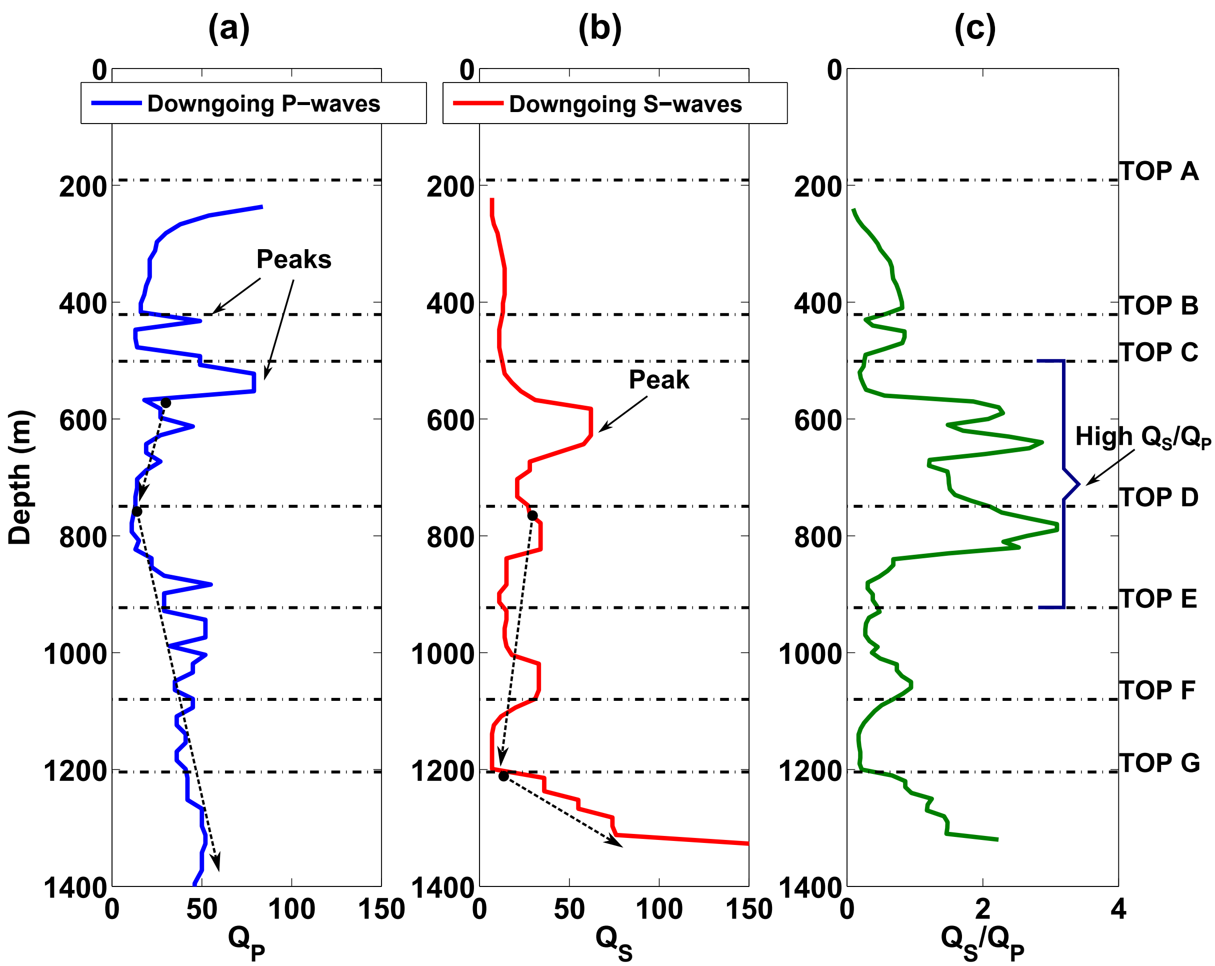

Figure 5.8: Q estimates using the spectral matching method (Case study 2). (a) Q_P estimates from the direct downgoing P-waves. (b) Q_S estimates from the direct downgoing S-waves. (c) Q_S/Q_P values.

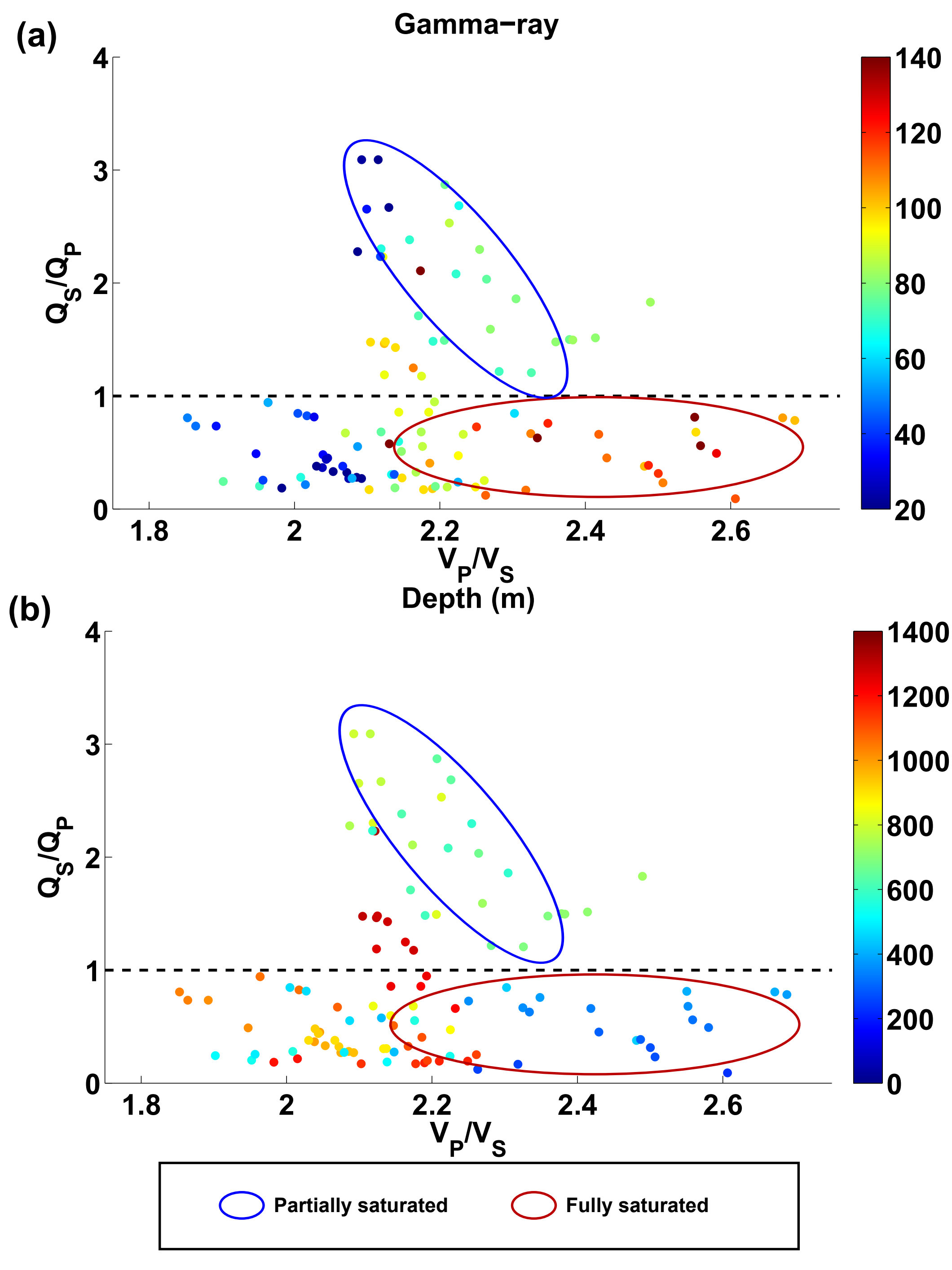

Figure 5.9: Seismic attenuation versus velocity ratio. (a) Scatter-plot coloured by gamma-ray, and (b) by receiver depth.

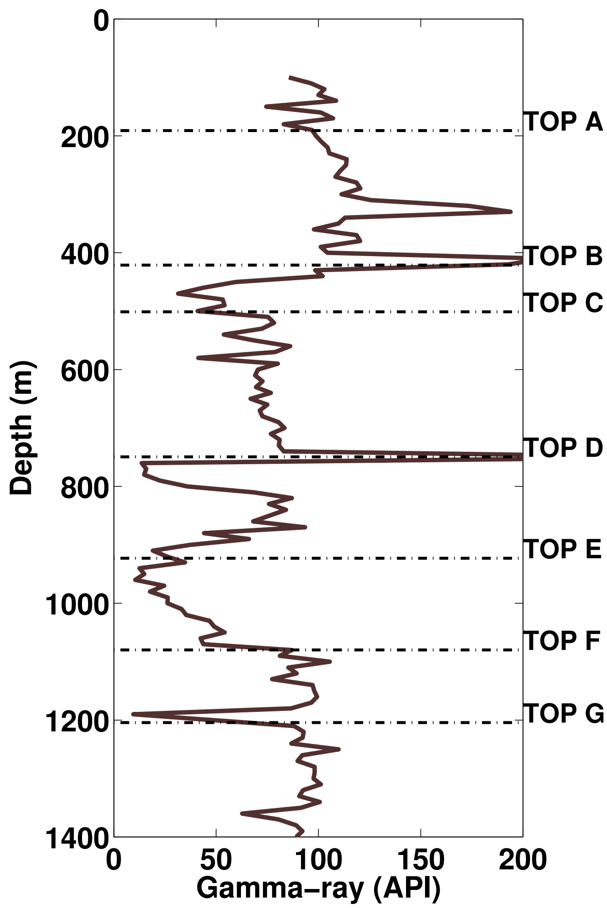

Figure 5.10: Gamma-ray for case study 2.

5.4 Future work

As mentioned in the Q analysis, we could use a receiver separation variable with depth, since the wavelength also changes with depth. We note this variation because this borehole is deeper than the previous one, and velocity varies more significantly with depth.

It would be interesting for this case, as we did for Case Study 1, to estimate Q_S from mode-converted upgoing S-waves in order to corroborate the previous Q_S estimates. Figure 5.11 shows a seismic gather of three mode-converted waves recorded with the source point offset 300 m from the borehole.

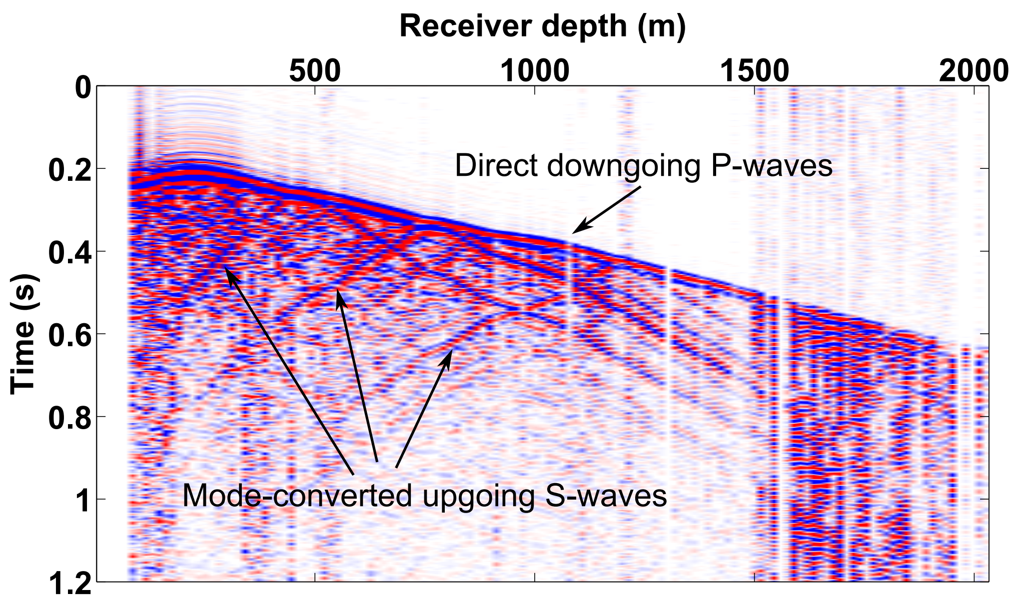

Figure 5.11: Source gather acquired with a Mertz 18 vibrator at 300 m offset from the borehole (Hmax).

Chapter 6

CONCLUSIONS

6.1 Conclusions

From the analysis of synthetics we conclude that analysis of the upgoing wavefield provides a good method to estimate near-surface Q. This should encourage more shallow receivers in VSP surveys. When we increased separation distance to estimate Q from downgoing or upgoing wavefields, we lost resolution and Q estimates became smoother. A layer with high Q is overestimated, meaning that we have to increase the separation distance to obtain a more accurate measure of attenuation in this layer.

Using hodogram rotation for converted-wave VSP data is a good alternative, particularly when an accurate velocity model that includes the overburden to compute the ray-tracing. Our results show that this method can be also used to focus the energy of the converted waves.

For case study 1, using the spectral matching method, we obtained values of $Q_P \simeq 50$ through the rock column, with a peak of 100 close to Formation Top A. In comparison, Q_S is $\simeq 20$ through the rock column and Q_S/Q_P ranges from 0 to 7. We concluded that variations in Q are related to changes in lithology. Converted-wave data may help to obtain more reliable Q_S estimates. These waves are more complex but we can use their unique characteristics to estimate Q. The QVO method which is usually used for surface seismic data, helped us to convey our Q_S estimations from VSP converted-wave data. These values range from $\simeq 10$ to $\simeq 33$. In order to do a comprehensive reservoir characterization, it is necessary to first understand the rock properties of the area. Seismic attenuation may help to move one step closer to this goal. Results show that we can compare seismic attenuation versus velocities to identify fluid saturation changes in rocks.

For case study 2, using the spectral matching method, we obtained values of $Q_P \simeq 50$ through the rock column, with two peaks close to the Formation Tops B and C. In comparison, Q_S is about 30 through the rock column. At $\simeq 600$ m, we observed a peak that may not be related to variations in the lithology. Q_S/Q_P ranges from 0 to 4 where high values are between 500 m and 920 m.

6.2 Recommendations

Add noise to the synthetic VSP to study how it affects our Q estimates. Also, compute synthetic VSPs based on more complex models, such as Marmousi that includes structures and thin layers.

Further study of the relationship between seismic attenuation and rock properties is needed. These values can be used to estimate gas saturation and lithology discrimination, among other properties.

For Q estimations from shallow VSP surveys, such as case study 1, a constant receiver separation can be used. Whereas, for Q estimations from deep VSP surveys, such as case study 2, it will be necessary to vary the receiver separation with depth in order to obtain more accurate results. The reason for this is that wavelength varies with depth.

Appendix A

Horizontal rotation

In the first rotation, x is rotated to the horizontal x' in the direction of direct arrivals and y to the horizontal y',

$$x' = x\cos\theta + y\sin\theta \tag{A.1}$$

$$y' = -x\sin\theta + y\cos\theta \tag{A.2}$$

where θ is the angle between x and the direct arrivals particle velocity (Figure 2.8).

$$Energy(\theta) = \sum_{t_0}^{t_1}(x(t)\cos\theta + y(t)\sin\theta)^2 = |X\cos\theta + Y\sin\theta|^2 \tag{A.3}$$

where t_0 and t_1 is the initial and final time for a given time window. Then, we calculate the maximum energy,

$$\tan 2\theta_{max} = \frac{2X \cdot Y}{X \cdot X - Y \cdot Y} \tag{A.4}$$

where θ_{max} is the orientation that maximizes the energy.

For the second rotation, the horizontal component Hmax and the vertical component z are polarized using an angle of rotation α.

Appendix B

Caliper for case study 2

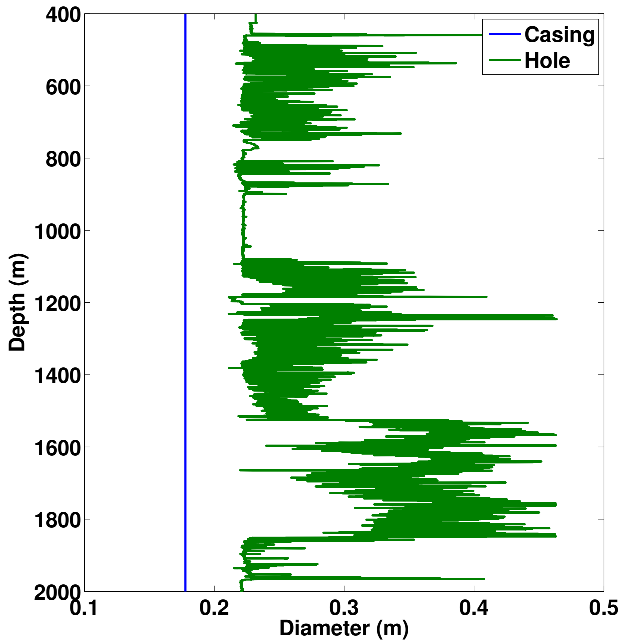

Figure B.1: Casing and hole diameter for case study 2.

References

Aki, K. and Richards, P. (1980). *1980: Quantitative Seismology: Theory and Methods.* Volume I: WH Freeman & Co.

Armstrong, P., Verliac, M., Monroy, N., Ramirez, H. B., and Leite, A. O. (2001). Shear wave applications from zerooffset vsp data. *SEG Technical Program Expanded Abstracts 2001*, pages 448–451.

Dasgupta, R. and Clark, R. A. (1998). Estimation of q from surface seismic reflection data. *GEOPHYSICS*, 63(6):2120–2128.

DiSiena, J. P., Gaiser, J. E., and Corrigan, D. (1984). *Horizontal component and shear wave analysis of three-component VSP data*, volume 14B. Geophysical Press.

Domenico, S. N. (1976). Effect of brinegas mixture on velocity in an unconsolidated sand reservoir. *GEOPHYSICS*, 41(5):882–894.

Ganley, D. C. (1981). A method for calculating synthetic seismograms which include the effects of absorption and dispersion. *GEOPHYSICS*, 46(8):1100–1107.

Hardage, B. A. (1981). An examination of tube wave noise in vertical seismic profiling data. *GEOPHYSICS*, 46(6):892–903.

Hardage, B. A. (1985). *Vertical Seismic Profiling: Principles*, volume 14A. Geophysical Press.

Hinds, R., Anderson, N., and Kuzmiski, R. (1996). *VSP Interpretive Processing.* Society of Exploration Geophysicists.

Kjartansson, E. (1979). Constant q-wave propagation and attenuation. *Journal of Geophysical Research: Solid Earth*, 84(B9):4737–4748.

Liner, C. L. (2012). *Elements of Seismic Dispersion: A Somewhat Practical Guide to Frequency-Dependent Phenomena.* Society of Exploration Geophysicists.

Liu, H.-P., Anderson, D. L., and Kanamori, H. (1976). Velocity dispersion due to anelasticity; implications for seismology and mantle composition. *Geophysical Journal International*, 47(1):41–58.

Margrave, G. (2013). Q tools: Summary of crewes software for q modelling and analysis. *CREWES Research Report*, 25:22.

Martinez, A. and Jones, M. (2010). *Fundamentals of borehole seismic technology*. Schlumberger Oilfield Marketing Communications.

Mavko, G. M. and Nur, A. (1979). Wave attenuation in partially saturated rocks. *GEOPHYSICS*, 44(2):161–178.

Montano, M., Lawton, D., and Margrave, G. (2015). Near-surface q estimation: an approach using the up-going wave-field in vertical seismic profile data. *SEG Technical Program Expanded Abstracts 2015*, pages 5600–5604.

Morse, P. and Feshbach, W. (1953). *Methods of theoretical physics*. McGraw-Hill Book Co.

Richards, P. G. and Menke, W. (1983). The apparent attenuation of a scattering medium. *Bulletin of the Seismological Society of America*, 73(4):1005–1021.

Schlumberger (1998). Oilfield glossary. *Schlumberger*.

Spencer, T. W., Sonnad, J. R., and Butler, T. M. (1982). Seismic qstratigraphy or dissipation. *GEOPHYSICS*, 47(1):16–24.

Winkler, K. W. and Nur, A. (1982). Seismic attenuation: Effects of pore fluids and frictionalsliding. *GEOPHYSICS*, 47(1):1–15.

Wu, B. (2016). *A Multicomponent Walkaway Vertical Seismic Profile Experiment in a Heavy Oil Reservoir*. University of Calgary.